Nonlinear Models and Geometric Structure of Fluid Forcing on Moving Bodies

Gary K. Nave, Jr.

Nonlinear Models and Geometric Structure of Fluid Forcing on Moving Bodies

Gary K. Nave, Jr.

ABSTRACT

This dissertation presents useful nonlinear models for fluid forcing on a moving body in two distinct contexts, and methods for analyzing the geometric structure within those and other mathematical models. This manuscript style dissertation presents three works within the theme of understanding fluid forcing and geometric structure.

When a bluff body is free to move in the presence of an incoming bluff body wake, the average forcing on the body is dependent on its position relative to the upstream bluff body. This position-dependent forcing can be conceptualized as a stiffness, much like a spring. This work presents an updated model for the quasi-steady fluid forcing of a wake and extends the notion of wake stiffness to consider a nonlinear spring. These results are compared with kinematic experimental results to provide an example of the application of this framework.

Fluid force models also play a role in understanding the behavior of passive aerodynamic gliders, such as gliding animals or plant material. The forces a glider experiences depend on the angle that its body makes with respect to its direction of motion. Modeling the glider as capable of pitch control, this work considers a glider with a fixed angle with respect to the ground. Within this model, all trajectories in velocity space collapse to a 1-dimensional invariant manifold known as the terminal velocity manifold. This work presents methods to identify the terminal velocity manifold, investigates its properties, and extends it to a 2-dimensional invariant manifold in a 3-dimensional space.

Finally, in the search for manifolds such as the terminal velocity manifold, this dissertation introduces a new diagnostic for identifying the low dimensional geometric structure of models. The trajectory divergence rate uses instantaneous vector field information to identify regions of large normal stretching and strong normal convergence between nearby invariant manifolds. This work lays out the mathematical basis of the trajectory divergence rate and shows its application to approximate a variety of structures including slow manifolds and Lagrangian coherent structures.

This dissertation applies nonlinear theoretical and numerical techniques to analyze models of fluid forcing and their geometric structure. The tools developed in this dissertation lay the groundwork for future research in the fields of flow-induced vibration, plant and animal biomechanics, and dynamical systems.

Nonlinear Models and Geometric Structure of Fluid Forcing on Moving Bodies

Gary K. Nave, Jr.

GENERAL AUDIENCE ABSTRACT

When an object moves through a fluid such as air or water, the motion of the surrounding fluid generates forces on the moving object, affecting its motion. The moving object, in turn, affects the motion of the surrounding fluid. This interaction is complicated, nonlinear, and hard to even simulate numerically. This dissertation aims to analyze simplified models for these interactions in a way that gives a deeper understanding of the physics of the interaction between an object and a surrounding fluid. In order to understand these interactions, this dissertation looks at the geometric structure of the models. Very often, there are low-dimensional points, curves, or surfaces which have a very strong effect on the behavior of the system. The search for these geometric structures is another key theme of this dissertation. This dissertation presents three independent studies, with an introduction and conclusion to discuss the overall themes.

The first work focuses on the forces acting on a cylinder in the wake of another cylinder. These forces are important to understand, because the vibrations that arise from wake forcing are important to consider when designing bridges, power cables, or pipes to carry oil from the ocean floor to offshore oil platforms. Previous studies have shown that the wake of a circular cylinder acts like a spring, pulling harder on the downstream cylinder the more it is moved from the center of the wake. In this work, I extend this idea of the wake as a spring to consider a nonlinear spring, which keeps the same idea, but provides a more accurate representation of the forces involved.

The second work considers a simple model of gliding flight, relevant to understanding the behavior of gliding animals, falling leaves, or passive engineered gliders. Within this model, a key geometric feature exists on which the majority of the motion of the glider occurs, representing a 2-dimensional analogy to terminal velocity. In this work, I study the properties of this influential curve, show several ways to identify it, and extend the idea to a surface in a 3-dimensional model.

The third study of this dissertation introduces a new mathematical quantity for studying models of systems, for fluid-body interaction problems, ocean flows, chemical reactions, or any other system that can be modeled as a vector field. This quantity, the trajectory divergence rate, provides an easily computed measurement of highly attracting or repelling regions of the states of a model, which can be used to identify influential geometric structures. This work introduces the quantity, discusses its properties, and shows its application to a variety of systems.

Acknowledgments

The work of this dissertation could not have happened without the support of all of the incredible people in my life. It has been a long and challenging road to finish this work, but the wonderful people along the way have made the hard work a joy.

To my family, thank you for supporting and encouraging me toward this goal my entire life. You have loved me unconditionally, encouraged me relentlessly, and stood by me through everything. Thank you.

To my friends, thank you for keeping me sane through all of this, whether you realized it or not. You have helped me see the world beyond graduate school, and I have needed the reminder that the world is bigger than all of this more times than I can count.

To the Engineering Mechanics program at Virginia Tech, thank you so much for being my family on campus. I have gained so much through my relationships with all of the faculty, staff, and students of this program. Thank you for providing a home for me at Virginia Tech for 10 years, between my B.S. and Ph.D.

To the community of Fieldstone United Methodist Church, thank you for providing a place to serve Christ in the New River Valley along with you for the past 10 years. Your heart for serving the world is something I'll never forget.

To Dean DePauw and the Virginia Tech Graduate School, thank you for providing refreshing perspectives on higher education. The Preparing the Future Professoriate curriculum, the Global Perspectives Program, and the Graduate Student Assembly have broadened my understanding of graduate school and higher education in ways I never imagined.

To my labmates and coworkers in the Stremler Lab, the Ross Dynamics Lab, and the Bio-Trans program, the many hours of conversations that we've had together about science and life have been a source of incredible learning for me. I will always cherish your friendship.

To my committee and especially my advisors, thank you for not only being the kind of professors that I want to be, but the kind of people that I want to be. Your support as academic and personal mentors has meant so much to me. I have been incredibly lucky to have freedom to pursue a wide variety of research directions, and I have felt completely supported the entire time.

Finally, thank you to my incredible and lovely wife, Amy. Meeting you was the most important thing that happened to me in all of graduate school. I couldn't imagine that I would have finished this thing if we hadn't been working on our PhDs together. Thank you for standing by my side through this whole process, for giving me pep talks when I doubted myself, and for inspiring me by being excellent in your own work. I love you!

Contents

List of Figures

Chapter 1

Introduction

1.1 Low-dimensional and simplified models in mechanics

Mathematical models of complex phenomena provide frameworks to compare systems across different parameters. With modern flow visualization and computational techniques, we can know high resolution 3D information about fluid flows with more detail than ever before. However, understanding the implications of the detailed flow information is a challenge of its own. Simplified models, on the other hand, allow us to deeply understand the primary components of the physics of the system. Low-dimensional models can be visualized and understood in ways that high-dimensional models cannot. In the words of the statistician George Box [1],

> The most that can be expected from any model is that it can supply a useful approximation to reality: All models are wrong; some models are useful.

There are many examples where simplified models play a unifying role in studying a complex phenomenon. When a moving body interacts with an incoming vortex wake, for example, the fluid forces it encounters may cause large oscillations. The parameter space for such a system is very large: streamwise and transverse body spacing, mass, damping, constraints of motion, and body shape. All of these factors make it very challenging to compare the variety of experimental and numerical investigations in the literature [2]. Comparing experimental

1

and computational results with predictions from a model can supplement the comparison of raw experimental results and provide a more general understanding of the phenomena associated with flow-induced vibration.

As another example, animals which exhibit gliding behavior range from gliding ants to flying squirrels and flying snakes, each displaying a different body morphology, behavior during flight, and aerodynamic capabilities [3]. There are currently a few parameters which can be used to compare these models, such as wing loading, equilibrium glide angle and lift-to-drag ratio, but to compare their non-equilibrium glide behaviors, a new framework is necessary [4]. With modern computational and experimental techniques, it is possible to visualize and simulate the fluid flows that move around these bodies [5, 6], but interpreting the implications of differences in these results is challenging, particularly in relation to making predictions of future behavior. A simplified model which accounts for non-equilibrium trajectories would provide a useful framework to understand the differences in aerodynamic behavior across a variety of passively falling bodies.

Such simplified models can be better understood through tools which identify key features in their structure. Within the model of a system, there may be lower-dimensional geometric features which dominate the system's dynamics. For instance, in the model of gliding flight presented in Chapter 3, there is a single 1-dimensional curve which attracts all possible trajectories of gliding bodies [4, 7]. By detecting and analyzing this attracting structure, we can more easily visualize the global dynamics of the model for comparison across multiple gliders. With these lower-dimensional features in flows, it is possible to gain a global understanding the key features in a flow, as they indicate the most influential regions of the flow.

In this dissertation, I present three works in manuscript format, each as a standalone work that has either been recently submitted or will be soon submitted to a journal for publication. The focus of this dissertation is to develop frameworks and tools which increase our understanding of systems by providing common points of comparison or useful visualizations. All three works fall within the realm of low dimensional models or tools, with a focus on forces resulting from fluid motion or the geometry of flows.

1.2 The challenge of understanding fluid forces

The problem of predicting the motion of flowing air or water, and therefore the resulting forces on a body within the flowing fluid, remains the focus of a broad array of research. Fluid motion is governed by the Navier-Stokes equations, for which even the existence and smoothness of solutions remains an open question. Only under specific assumptions do the Navier-Stokes equations allow for exact solutions. High-dimensional computational methods to simulate fluid motion through discrete approximations of the governing equations have led to many excellent results and improved our understanding of flows, but require significant computational resources and remain limited in application at present. Adding the coupling of body motion to the complexity of the problem, computational methods for fluid-structure interaction are only possible for a very narrow range of problems relative to the space of relevant problems [8]. Just as scientific pursuits continue in such high dimensional spaces, it is important to refine low-dimensional models of fluid motion and forcing.

In the face of the complexity of fluid forces on moving bodies, it is useful to consider more simplified models which give the dominant behavior. As the simplest example, the drag force on a fixed bluff body may be found to be, through the application of Bernoulli's equation or dimensional analysis,

$$F_D = C_D \frac{1}{2} \rho U_0^2 A, \tag{1.1}$$

where A is the cross-sectional area of the body, U_0 is the free stream velocity of the fluid, ρ is the fluid density, and the drag coefficient C_D is a function of Reynolds number only [9]. In the incompressible, inviscid limit, potential flow models have proven useful at predicting the dynamics resulting from flows, often using the Kirchhoff equations [10, 11, 12, 13, 14]. In aerodynamics, methods such as the blade element theory, vortex panel methods, and lifting line theory all serve to provide an effective approximation for the fluid forces experienced during flight, although the practical forces experienced by an airplane may vary.

In this dissertation, I make use of the quasi-steady approach to modeling fluid forces, in which time dependent fluid forces are averaged to find the mean resultant fluid force at each static configuration. These forces, then, become dependent on a body's position, orientation, or configuration within a system. The dynamics are then allowed to evolve with the modeled fluid forces as functional inputs. Using the quasi-steady model for fluid forces allows us to investigate the dominant effect of fluid forces on the body without considering in detail the fluid dynamics. If we consider such models while acknowledging their shortcomings, they

allow us to gain a deeper understanding of the dominant physics with the understanding that other components of the physics may dominate in other circumstances. Chapters 2 and 3 of this dissertation both focus on fluid force modeling, applying existing quasi-steady experimental results in two different contexts.

1.3   The geometric structure of flows

When investigating the behavior of a mathematical model or fluid simulation or experiment, it is useful to look beyond the results of a single simulation or trajectory. While a trajectory gives the time-parametrized solution of a system of equations for a single initial condition $\mathbf{x}_0$,

$$\mathbf{F}_{\mathbf{x}_0} : t \mapsto \mathbf{x}, \tag{1.2}$$

the solution may be expressed in terms of the one-parameter, or time-t, flow map, which defines a mapping that takes any initial condition $\mathbf{x}_0$ to its position $\mathbf{x}$ at a fixed time t,

$$\mathbf{F}_t : \mathbf{x}_0 \mapsto \mathbf{x}. \tag{1.3}$$

The space of vectors based at the initial points $\mathbf{v}_0(\mathbf{x}_0)$ is mapped forward along with the flow by the gradient of the time-t flowmap,

$$\nabla \mathbf{F}_t : \mathbf{v}_0(\mathbf{x}_0) \mapsto \mathbf{v}(\mathbf{x}). \tag{1.4}$$

From the flow map, its gradient, and the vector field itself, it is possible to look at structures which significantly influence the global behavior of the system. Points for which $F_t(\mathbf{x}_0) = \mathbf{x}_0$ for all time t, are *equilibrium points*, which give the points at which the vector field goes to zero. These are the most basic geometric structures in a flow. The flow around an equilibrium point is organized by the *stable, unstable, and center manifolds* of the equilibrium. For a saddle equilibrium point, which is associated with both stable and unstable manifolds, nearby trajectories are repelled from the stable manifold and attracted to the unstable manifold in forward time.

Invariant manifolds have the property that any trajectory on the manifold must remain on the manifold for all time,

$$\Gamma = \{\mathbf{x}_0 : \mathbf{F}_t(\mathbf{x}_0) \in \Gamma \ \forall t\}. \tag{1.5}$$

In an autonomous system, every trajectory is itself an invariant manifold. Equilibrium points are 0-dimensional invariant manifolds, as the point trivially maps to itself. Other examples of invariant manifolds in flows include limit cycles, KAM tori [15], transition tubes [16, 17], and normally hyperbolic invariant manifolds [18].

Coherent structures are defined as material curves which act as barriers to transport in a flow. Within a fluid context, these are identified as Lagrangian if they are calculated from the trajectory advection (i.e., the time-t flowmap) or Eulerian if they are calculated from the vector field itself. The regions of fluid separated by coherent structures are *coherent sets*. In Chapters 3 and 4, I apply and develop methods to identify geometric structures such as the ones discussed here. Chapter 3 analyzes the geometric properties of a single mathematical model, focused on finding an attracting submanifold in phase space. Chapter 4 introduces a diagnostic which can be used to approximate normally hyperbolic invariant manifolds and coherent structures or give local stability information of invariant manifolds.

1.4 Research Overview

This dissertation comprises three projects, all of which related to the ideas of fluid forces on bodies and the geometric structure of flows.

In Chapter 2, I consider a model for the forces that an incoming bluff body wake enacts on a moving body. The idea of linear wake stiffness is combined with an updated nonlinear model for quasi-steady fluid forces to develop the framework of nonlinear wake stiffness. This model is then applied in comparison with kinematic experiments on a new configuration of cylinders. This framework can be used to compare disparate experiments and simulate complex fluid-structure interactions across regimes of fluid forcing. We extend existing models in the literature to develop a framework for comparing different systems and experimentally analyze one such system using the new framework.

In Chapter 3, I use a two degree-of-freedom model to understand the aerodynamic descent of gliding animals and fluttering seeds. Within the phase space of this 2-dimensional model, a 1-dimensional attracting manifold emerges. This attracting manifold serves as a higher-dimensional analog of terminal velocity — the terminal velocity manifold. I show that nearly all of the dynamics of gliding flight and fluttering descent happen along this terminal velocity manifold within the 2-dimensional model and calculate the terminal velocity manifold in the

3-dimensional extended phase space.

In Chapter 4, I introduce a new method for detecting attracting or repelling structures in a flow, the trajectory divergence rate. This diagnostic may be used to rapidly approximate coherent structures in fluid flows or the flows of differential equations. I show applications of this method to find slow manifolds in slow-fast systems and how it compares to known methods in atmospheric fluid flows.

1.5 Research topics not covered in this dissertation

Because of the interdisciplinary nature of this research, and the opportunities that I have had to work with various faculty at Virginia Tech, my research interests vary wildly. There are several projects to which I have contributed which are beyond the scope of the present dissertation. Some of these projects represent extensions of the work presented in this thesis, but are beyond the primary scope of the work. A brief summary of some further work of my dissertation is presented here.

1.5.1 Samara-inspired design of dispersed sensors through additive manufacturing

As a part of an interdisciplinary team of biologists and engineers, I was involved in a project which took inspiration from autorotating plant seeds known as samaras or "helicopter seeds." The shape of samaras allows them to spin rapidly as they fall from their parent tree, generating lift and slowing their descent. Therefore, they are more easily carried by the wind, which increases the area over which seeds may land and germinate and prevents the seedlings from having to grow in direct competition to the fully grown parent tree. From this natural inspiration, our team sought to develop engineered devices to mimic this behavior and carry loads such as sensors over a large area safely to the ground. As a part of this project, a team led by undergraduate students and mentored and assisted by graduate students and faculty was able to apply 3D printing techniques to recreate both silver maple seeds and Norway maple seeds which performed similarly to natural seeds. These natural and 3D printed seeds were compared by drop tests indoor, still-air conditions with high speed photography and in outdoor, windy conditions. Through another part of this project, a scaled up samara
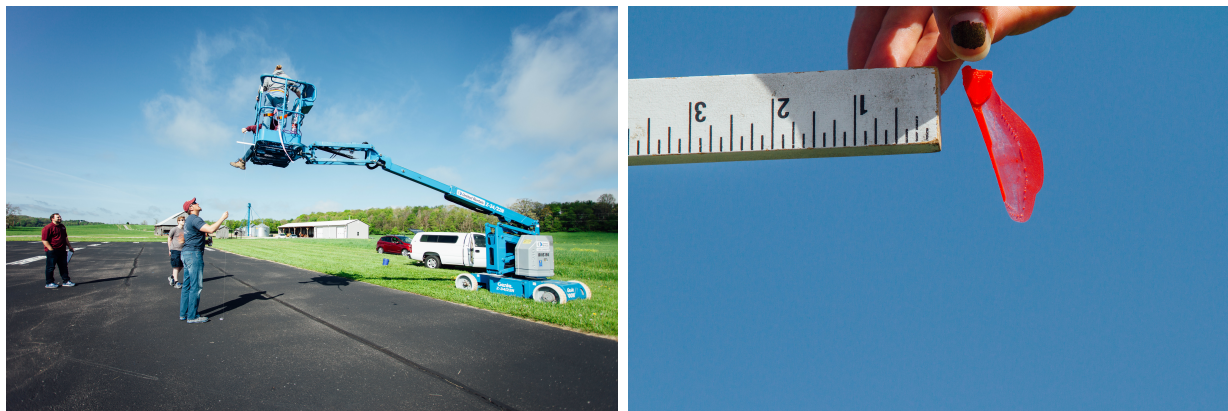
Figure 1.1: Photos of experimental setup for real wind condition drops of 3D printed Norway maple seeds. (left) Seeds were dropped from a cherry picker at a 10ft height from the ground. (right) Close-up of 3D printed samara.

was developed which housed a pressure sensor that recorded data to an SD card throughout its descent. This device was tested from the Virginia Tech Smart Road bridge, successfully collectively data while surviving a descent of 175 feet without the assistance of a parachute.

1.5.2 Wake effects on tandem airfoil gliders

For the 2016 International Congress of Theoretical and Applied Mechanics, I presented a talk which combined the ideas of nonlinear wake stiffness with the study of animal gliders [19]. Because the cross-sectional body shape of *Chrysopelea paradisi* has been shown to be a bluff body at every angle of attack [6], I hypothesized that the vortex wake shed by the upstream part of the body may enhance the lift forces experienced by the trailing bluff body. To give an approximation of the effects of this lift enhancement, I extended the tandem glider model of Jafari et al. [20] to incorporate wake effects using the model of Blevins [21] and simulated a collection of trajectories from various initial glide conditions. The extended abstract from this presentation is presented in Appendix A.

Through this work, I was able to show that a lift enhancement that follows the form of the quasi-steady wake of circular cylinders enhances the stability of a tandem wing glider, given an offset wake centerline due to lift. Figure 1.2 shows this stability enhancement by showing the initial conditions for which a glide is successful. Successful glides are those for which the glider travels more than 10m forward over a 10m vertical descent. The modeled wake effects of this project increase the range of initial conditions that allow for successful glides.
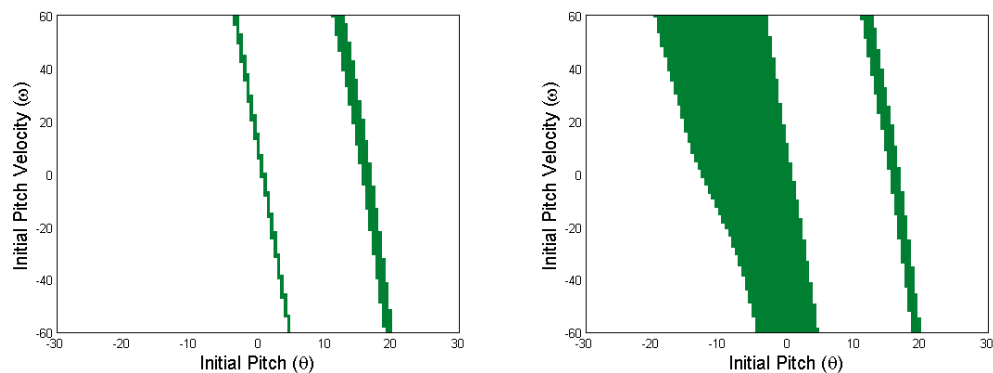
Figure 1.2: Comparison of the results of simulated glides without(left) and with(right) a lift enhancement model based on wake stiffness. Green regions are considered "stable" glides based on whether the glider traveled at an angle shallower than 45°.

1.5.3   Energy harvesting with flow-induced vibration

The tethered cylinder arrangement considered in Chapter 2 was originally developed as a energy harvesting device. In the device, the trailing cylinder is rigidly attached to a vertical shaft allowed to rotate in the center of the upstream cylinder. The oscillating rotation of this shaft is then rectified to a single direction of rotation through the drivetrain pictured in Figure 1.3. This method for energy harvesting shows significant promise for energy harvesting at lower flow speeds where traditional hydrodynamic turbines fail.
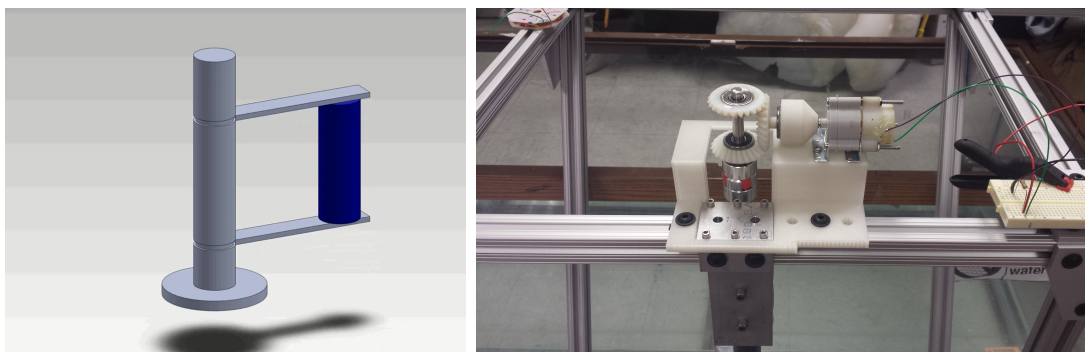
Figure 1.3: (left) Schematic of the vortex-induced vibration energy harvesting system, courtesy of Saikat Basu. (right) Photograph of custom gear assembly designed to rectify cylinder oscillations to single direction of rotation.

Bibliography

[1] George EP Box, J Stuart Hunter, and William Gordon Hunter. *Statistics for experimenters: design, innovation, and discovery*, volume 2. Wiley-Interscience New York, 2005.

[2] Turgut Sarpkaya. A critical review of the intrinsic nature of vortex-induced vibrations. *Journal of Fluids and Structures*, 19(4):389–447, 2004.

[3] Farid Socha, John J.and Jafari, Yonatan Munk, and Greg Byrnes. How animals glide: from trajectory to morphology. *Canadian Journal of Zoology*, 93(12):901–924, 2015.

[4] Isaac J. Yeaton, John J. Socha, and Shane D. Ross. Global dynamics of non-equilibrium gliding in animals. *Bioinspiration & Biomimetics*, 12(2):026013, 2017.

[5] Hui Wan, Haibo Dong, and Kuo Gai. Computational investigation of cicada aerodynamics in forward flight. *Journal of The Royal Society Interface*, 12(102):20141116, 2015.

[6] Anush Krishnan, John J. Socha, Pavlos P. Vlachos, and L.A. Barba. Lift and wakes of flying snakes. *Physics of Fluids*, 26(3):031901, 2014.

[7] Gary K Nave Jr and Shane D Ross. Global phase space structures in a model of passive descent. *Under review, arXiv Preprint arXiv:1804.05099*, 2018.

[8] Earl H Dowell and Kenneth C Hall. Modeling of fluid-structure interaction. *Annual Review of Fluid Mechanics*, 33(1):445–490, 2001.

[9] George Keith Batchelor. *An introduction to fluid dynamics*. Cambridge University Press, 2000.

[10] Horace Lamb. *Hydrodynamics*. Cambridge University Press, 1932.

[11] Naomi Ehrich Leonard. Stability of a bottom-heavy underwater vehicle. *Automatica*, 33(3):331–346, 1997.

[12] Banavara N Shashikanth, Jerrold E Marsden, Joel W Burdick, and Scott D Kelly. The hamiltonian structure of a two-dimensional rigid circular cylinder interacting dynamically with n point vortices. *Physics of Fluids*, 14(3):1214–1227, 2002.

[13] Alexey V. Borisov and Ivan S. Mamaev. On the motion of a heavy rigid body in an ideal fluid with circulation. *Chaos: An Interdisciplinary Journal of Nonlinear Science*, 16(1):013118, 2006.

[14] Scott David Kelly and Hailong Xiong. Self-propulsion of a free hydrofoil with localized discrete vortex shedding: analytical modeling and simulation. *Theoretical and Computational Fluid Dynamics*, 24(1-4):45–50, 2010.

[15] Stephen Wiggins. *Introduction to applied nonlinear dynamical systems and chaos*, volume 2. Springer Science & Business Media, 2003.

[16] Wang Sang Koon, Martin W Lo, Jerrold E Marsden, and Shane D. Ross. *Dynamical systems, the three-body problem and space mission design*. Citeseer, 2008.

[17] Jun Zhong, Lawrence N Virgin, and Shane D Ross. A tube dynamics perspective governing stability transitions: An example based on snap-through buckling. *International Journal of Mechanical Sciences*, 2017.

[18] Stephen Wiggins. *Normally hyperbolic invariant manifolds in dynamical systems*, volume 105. Springer Science & Business Media, 2013.

[19] Gary K. Nave Jr., Mark Stremler, and Shane D. Ross. Wake stiffness and its application: oscillating cylinders and flying snakes. In *Proceedings of the 24th International Congress on Theoretical and Applied Mechanics (ICTAM)*, 2016.

[20] Farid Jafari, Shane D. Ross, Pavlos P. Vlachos, and John J. Socha. A theoretical analysis of pitch stability during gliding in flying snakes. *Bioinspiration & Biomimetics*, 9(2): 025014, 2014.

[21] Robert D. Blevins. Forces on and Stability of a Cylinder in a Wake. *Journal of Offshore Mechanics and Arctic Engineering*, 127(1):39–45, March 2005. ISSN 0892-7219. doi: 10.1115/1.1854697.

Chapter 2

Wake stiffness as a nonlinear spring

Abstract

Previous attempts to describe the quasi-steady variation of fluid forces on a body in the wake of a fixed bluff body have conceptualized the changing lift force as a stiffness. The lift coefficient varies linearly with transverse position within a neighborhood of the wake centerline, pushing the body back toward the centerline of the wake as a restoring force. In this work, we extend the concept of wake stiffness to a nonlinear framework, dependent on a nonlinear model for fluid force coefficients, which allows for system configurations beyond a transversely oscillating tandem cylinder. To improve the accuracy of this framework, we update existing nonlinear fluid force models, taking into account the critical spacing in the gap between bluff bodies and incorporating data from several experimental sources. We show the application of this framework with the updated model to a novel cylinder configuration of a pair of circular cylinders in which the distance between the two is fixed. This work provides a launching point to compare disparate fluid-structure interaction experiments, and improves the capabilities of fluid force modeling in engineering application.

Attribution

This research was conducted in collaboration with Mark Stremler, who contributed to the work through idea development, editing, and support. The idea for the tethered cylinder

arrangement was originally conceived by Dr. Stremler and Dr. Pavlos Vlachos.

2.1   Introduction

Flow-induced vibration (FIV) refers to any of several phenomena in which the motion of air or water past or through a body causes persistent oscillations. These oscillations could be driven by shape asymmetries, vortex shedding, or a non-uniform incoming flow, but all present complex problems as the motion of the body and motion of the surrounding fluid cannot easily be decoupled. The study of the physical phenomena which lead to FIV is essential. In different contexts, flow-induced vibration can present a challenge or a benefit. It has the ability to generate power and disperse plant seeds as well as the capacity to destroy bridges and destabilize underwater structures.

The way in which a body's interaction with surrounding fluid leads to flow-induced vibration varies significantly depending on the configuration of the system [1, 2, 3, 4]. The most well-studied example, vortex-induced vibration, occurs for a single elastically-mounted cylinder in a uniform incoming flow [5, 6, 7]. In vortex-induced vibration, the elasticity of the system is excited by the oscillating pressure of the wake behind the body over a narrow range of velocities, known as the lock-in region. For velocities above or below the lock-in region, oscillations remain small. However, when that same elastically mounted cylinder is placed in the wake of a fixed upstream cylinder, the oscillations continue to grow toward an asymptotic limit as flow velocity increases beyond the lock-in region [2, 3, 8, 9, 10, 11, 12]. These observed oscillations in the wake occur at a lower frequency than the vortex formation and are therefore due to some mechanism other than resonance with the wake. In fact, these oscillations persist even if there is no structural stiffness present [13].

When the moving body is sufficiently far downstream of the upstream body, the wake formation of the upstream body is independent of the downstream body [2, 3, 4]. The body's interaction with the incoming vortex wake causes persistent oscillations of the body through a phenomenon known as wake-induced vibration (WIV) [8]. The combined effect of the incoming vortex wake and the shed vortices from the second body drive the body's oscillations, even though the vortex shedding occurs above the resonant frequency. In the context of this phenomenon, Assi et al. [13] develop the notion of *wake stiffness*. Within approximately 1 diameter of transverse displacement from the wake centerline, the coefficient of lift varies

linearly to drive the body back toward the wake centerline, as shown below in Fig. 2.2. We offer a discussion of this model and others below in Section 2.2.

On the other hand, when a body is placed in the near wake of a fixed bluff body, there is not enough space for vortex formation in the gap between the bodies [2, 3, 4]. When the cylinders are directly in tandem, the flow moves around both cylinders and the shear layer "reattaches" to the downstream cylinder [4], but when the trailing cylinder is displaced from the centerline, the fluid flow redirects to move through the gap between the two cylinders [14]. Therefore, the phenomenon which drives oscillations when the cylinders are close is known as gap flow switching (GFS).

Between the gap flow switching and wake-induced vibration regimes, there is a critical streamwise spacing ℓ_c, which is the point at which coherent vortex formation begins to occur in the gap. At the critical spacing, the drag coefficient at the wake centerline, Strouhal frequency of the wake, and qualitative behavior of the flow all rapidly change. However, there is a wide variety in the reported location of this critical spacing, as shown in Fig. 2.1. It has been shown that there is bistability between the two regimes of fluid phenomena [3, 15, 16], and that there is, in fact, hysteresis in the location of the critical spacing, leading to a different behavior between when the spacing is being increased or being decreased. For further discussion on the hysteresis and location of maximum and minimum critical spacings, see [17].

In a complex problem such as the motion of a cylinder in an incoming wake, simplified models provide a pivotal role alongside highly resolved computational and experimental studies. These simplified models provide the capacity for comparison across systems. By comparing experiments with different configurations with a common model under different parameters, we can develop more general insights about the differences between systems and make inferences and predictions about new configurations. Therefore, in the present work, we seek to extend the concept of wake stiffness to be more widely applicable by considering nonlinear components of the variation of quasi-steady fluid force coefficients in Sec. 2.3. We present the full, two-dimensional wake stiffness model, with forces acting in both the streamwise and transverse directions, in Sec. 2.5. To inform the nonlinear wake stiffness framework, we expand existing nonlinear models for the quasi-steady fluid forces to incorporate the critical spacing of the wake and fluid forces in the GFS regime in Sec. 2.4. In Sec. 2.6, we apply the general framework to an example problem, in which the total distance between the two cylinders, rather than streamwise distance, is kept constant, and
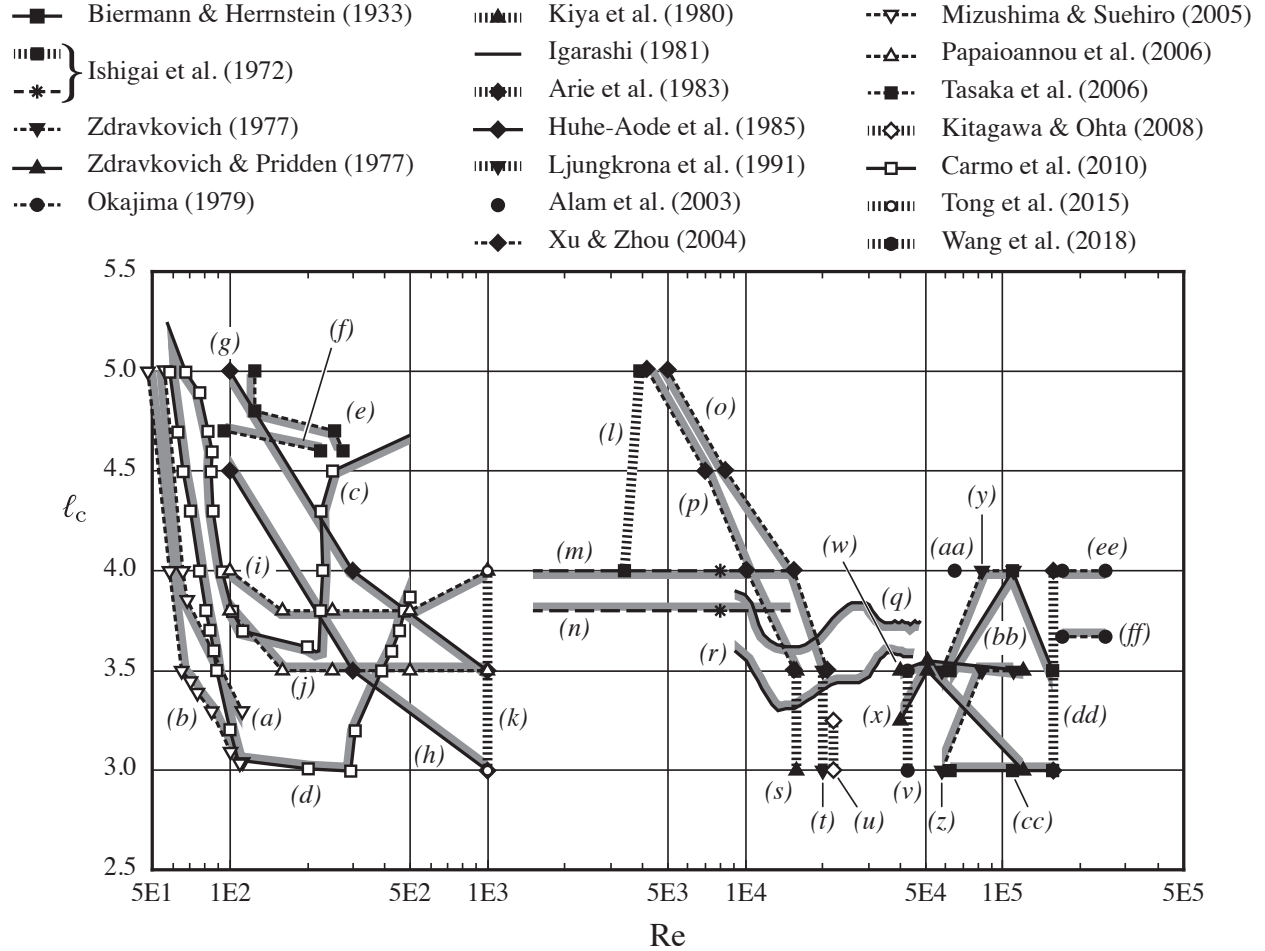
Figure 2.1: The critical spacing in the wake of a cylinder $\ell_c = x_c/D$, reported from various sources over a range of Reynolds numbers, reproduced with permission from preprint of [17]. Open symbols represent computational results, while closed symbols show experimental results. Upper (shading below) and lower (shading above) bounds indicate the possible range for $\ell_{c,min} \leq \ell_c \leq \ell_{c,max}$. Shown in the figure are (a,b) from [16, Fig. 9]; (c,d) from [18, Fig. 6]; (e,f) from [19, Fig. 8]; (g, h) from [20, Fig. 2]; (i,j) from [21, Fig. 8]; (k) from [22]; (l) from [23, Fig. 7]; (m,n) from [23]; (o,p) from [24]; (q,r) from [15, Fig. 16]; (s) from [25]; (t) from [26]; (u) from [27, Fig. 19]; (v) from [28]; (w,x) from [29, Figs. 1,3]; (y,z) from [2]; (aa) from [30]; (bb,cc) from [31, Fig. 8]; (dd) from [32]; (ee,ff) from [33].

the resultant of lift and drag variation is required to predict the effective stiffness of the wake. We compare the predicted behavior of the body with kinematic experimental results over a variety of cylinder separations both above and below the critical spacing.

2.2   Existing force models

Simplified models play an important role in the study of flow-induced vibrations, particularly in multi-body systems. Models have been used effectively in the engineering of offshore oil risers through software packages such as RIFLEX [34] and ORCAFLEX [35]. For engineering application, combined fluid-structure computational models which discretize the highly nonlinear interactions would be preferable, as these models would be better suited to extract all important phenomena in a system. However, although many recent advances have been made, general application of combined flow-induced vibration models remains a future goal for scientists in this field. Additionally, experimental studies alone cannot fully cover the extremely high parameter space in which FIV systems operate. Flow speed, body geometry, system geometry, structural constraints, mechanical stiffness, and mass-damping parameters all provide global bifurcations in FIV phenomena. Sarpkaya [36] discusses this in his critical review paper; a change in selected parameters may lead to a noticeable change in behavior as previously neglected features become dominant features. Therefore, for a new system, mathematical models built on both physical insights and experiments provide the best means for predicting the system's behavior.

As discussed in the introduction, in the present study we are concerned with pairs of circular cylinders as a representative system. A variety of papers dating back at least 50 years have sought to experimentally measure the effects of an upstream cylinder wake on a downstream cylinder. One of the most common techniques is to fix the downstream cylinder at a variety of positions in the wake and measure the average force on this cylinder. From these static cylinder measurements, some researchers have begun to develop quasi-steady force models, assuming that the force on a moving cylinder can be approximated as the mean fluid force on a stationary cylinder. In this section we discuss two of these existing models and provide an updated combined model. The models we will present are the work of [13] and [37]. From this updated model, we show an example application of this model to a novel system: a pair of tandem, tethered cylinders.

2.2.1   Linear Wake Stiffness, Assi et al. [13]

Although they are not the first to observe that the fluid forces on a body are dependent on their location in the wake, Assi et al. [13] conceptualize this observation as "wake stiffness." The idea is a rather elegant one: the fluid forces acting on a body in the wake of another tend to pull the downstream body back to the centerline of the wake. This stiffness manifests itself as a linear change in the lift coefficient, and therefore a linear change in fluid force, as the cylinder is displaced transverse to incoming flow.

They introduce the idea in their 2013 investigation of the oscillations of a freely mounted rigid cylinder in the wake of a fixed upstream cylinder. The cylinder was constrained to move along the transverse direction relative to the flow without any structural elasticity. They found that the cylinder oscillations persisted and amplitude continued to grow, much like the well studied motion of an elastically mounted rigid cylinder in the wake of a fixed upstream cylinder [8, 10, 12].

To determine the linear restoring force that drove these oscillations, they measured the mean and fluctuating fluid force coefficients on the downstream cylinder at an array of positions ranging from 1 to 6 diameters in the streamwise direction and 0 to 3 diameters in the transverse direction with a Reynolds number of $Re = 19,200$. As a specific example, they sample at higher resolution along $x^* = 4$, and repeated the experiment for Reynolds numbers of $Re = \{9600, 14500\}$. From these fluid force coefficients, they found that within 1 diameter of displacement, the lift coefficient increases linearly with displacement from the centerline, as shown in Figure 2.2.

In the transverse direction, the equation of motion is simply given by a forced mass-damper system, Equation (2.1), with m and c representing total mass and damping respectively, $y^* = y/D$ representing the transverse spacing normalized' by cylinder diameter, and ρ, U, and $\bar{C}_L$ representing fluid density, incoming flow velocity and quasi-steady lift force,

$$m\ddot{y}^* + c\dot{y}^* = \frac{1}{2}\rho U^2 D\bar{C}_L(y^*). \tag{2.1}$$

Due to the symmetry of the system, it must be true that $\bar{C}_L(y^*) = -\bar{C}_L(-y^*)$ and, therefore, that $\bar{C}_L(0) = 0$. Applying the linearization $\bar{C}_L = (d\bar{C}_L/dy^*)y^*$, we achieve a simple harmonic oscillator in Equation (2.2),
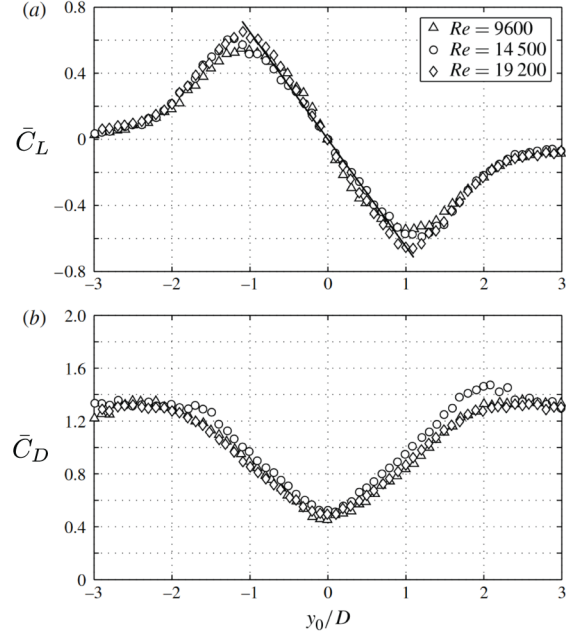
Figure 2.2: The relationship between transverse displacements y_0/D and quasi-steady fluid force coefficients in the transverse ($\bar{C}_L$) and streamwise ($\bar{C}_D$) directions for a fixed cylinder in the wake of another fixed cylinder at a downstream offset of 4 diameters ($x_0/D{=}4$) at various Reynolds numbers (Re). Reproduced from Assi et al. [13].

$$m\ddot{y}^* + c\dot{y}^* + \frac{1}{2}\rho U^2 D y^* \left| \frac{d\bar{C}_L}{dy^*} \right|_{y^*=0} = 0. \tag{2.2}$$

From this simple harmonic oscillator, we can calculate the natural frequency of the wake, f_w, given in dimensionless form by,

$$\frac{f_w D}{U} = \frac{1}{2\pi} \sqrt{\frac{2}{\pi} \frac{|d\bar{C}_L/dy^*|_{y^*=0}}{(m^* + c_a)}}. \tag{2.3}$$

where m^* and c_a are the dimensionless mass $m^* = 4m/\rho\pi D^2 L$ and dimensionless coefficient of added mass.

The idea of modeling an incoming wake as an effective stiffness on a downstream cylinder is compelling. As described in the paper and shown in Figure 2.2, nonlinear effects must be considered for transverse displacements beyond 1 diameter from the wake centerline. In some experimental setups, the downstream cylinder is allowed to oscillate about a point that is offset from the wake centerline, and this nonlinear regime will dominate. Therefore, to

develop a more general framework, as is our goal, we must develop a nonlinear wake stiffness model. To accomplish this goal, we must look toward another model of wake forces.

2.2.2   Quasi-steady coefficients in the wake, Blevins [37]

Work by Blevins seeks to develop a nonlinear model of quasi-steady fluid force coefficients due to position in the wake [37]. He takes experimental data from [38] and [39] on the mean lift and drag coefficients throughout the wake of an upstream cylinder, and fits this data to the coefficients of a theoretical model based on the velocity reduction in the wake. This semi-analytical formulation produces results that closely mimic the experimental lift and drag data presented.

The Blevins model is based on the assumption that the change in drag coefficient is due purely to the decreased mean velocity throughout the wake, following the work of [40]. He therefore begins with the mean velocity in the wake of a cylinder, given by the following equation, with C_{D0} representing the drag coefficient of the upstream cylinder and U_0 representing the free-stream velocity.

$$U(x^*, y^*) = U_0 \left(1 - 1.2 \left(\frac{C_{D0}}{x^*} \right)^{\frac{1}{2}} \exp \left[\frac{-13y^{*2}}{C_{D0}x^*} \right] \right), \tag{2.4}$$

where U_0 represents the free stream velocity, and C_{D0} is the mean drag on a fixed cylinder at the relevant Reynolds number. This expression for velocity is based on asymptotic relationships.

Since $F_D \propto C_D U^2$, he defines a new drag coefficient for the downstream cylinder based on the free stream velocity by scaling the drag coefficient with position rather than the velocity, as shown in Equation (2.5),

$$C_D(x^*, y^*)U_0^2 = C_{D0}U(x^*, y^*)^2. \tag{2.5}$$

His equation for drag coefficient follows from this by substituting equation 2.5 into equation 2.4 and replacing the coefficients of equation 2.4 with general coefficients, A_i, which are

adjusted to match experimental data,

$$C_D(x^*, y^*) = C_{D0} \left(1 - A_1 \left(\frac{C_{D0}}{x^*} \right)^{\frac{1}{2}} \exp\left[-\frac{A_2 y^{*2}}{C_{D0} x^*} \right] \right)^2. \tag{2.6}$$

The most interesting assertion is related to lift. He cites [10], [41] and a discussion by C.B. Rawlins on a conference paper by Simpson and Price [42] in asserting that lift coefficient can be determined by the transverse change in drag coefficient

$$C_L(x^*, y^*) = A_3 \frac{\partial C_D(x^*, y^*)}{\partial y^*}. \tag{2.7}$$

The justification is that the lift is due to the gradient in flow velocities and deflection of the wake. This assumption does seem to give the appropriate shape and warrants further investigation, and we will investigate it in Section 2.4.3. Applying this relation gives the following equation for lift coefficient as a function of position in the wake.

$$C_L(x^*, y^*) = A_3 \frac{y^*}{x^*} \left(\frac{C_{D0}}{x^*} \right)^{1/2} \left(1 - A_1 \left(\frac{C_{D0}}{x^*} \right)^{\frac{1}{2}} \exp\left[-\frac{A_2 y^{*2}}{C_{D0} x^*} \right] \right) \exp\left[-\frac{A_2 y^{*2}}{C_{D0} x^*} \right] \tag{2.8}$$

From his fit to the data from [38] and [39], Blevins finds the following coefficients:

$$
\begin{aligned}
A_1 &= 1, \\
A_2 &= 4.5, \\
A_3 &= -10.6.
\end{aligned}
\tag{2.9}
$$

This nonlinear model for fluid force coefficients provides an effective model, which is used in the next section in combination with the idea of wake stiffness to develop the notion of nonlinear wake stiffness. However, the model does not account for the critical spacing of the wake, and we will update the Blevins model in Section 2.4.

2.3   Wake Stiffness as a Nonlinear Spring

Using the nonlinear model for fluid forces such as the Blevins [37] model and the idea of wake stiffness of [13], we can now consider wake stiffness as a nonlinear spring. We will develop this further as a general 2 degree-of-freedom framework in Section 2.5, but as a first example, we will consider a transversely oscillating cylinder in tandem with a fixed upstream cylinder.

To begin, assume a steady, uniform flow with velocity U_0. This flow passes two cylinders of diameter D and length L, with the upstream cylinder fixed in place and the trailing cylinder free-to-move in the transverse direction in the absence of external forcing. This trailing cylinder has a mass of m, a linear damping coefficient of c, and a linear structural stiffness of k. Any other forcing that the body experiences is provided by the differential pressure on the body from the surrounding fluid. As we have seen in the previous models discussed in Section 2.2, the dominant fluid forces can be modeled as quasi-steady forces which depend solely on position in the wake. For now, we will consider the nonlinear model of Blevins [37], but we will introduce an updated model in Section 2.4. Because of our constraint to the transverse direction, we must only consider the lift force, which we treat the sum of quasi-steady and unsteady components given by,

$$F_L = \frac{1}{2}\left(\bar{C}_L + \hat{C}_L \cos(2\pi f_{St}t)\right)\rho LDU^2, \tag{2.10}$$

where $\bar{C}_L$ is the quasi-steady lift coefficient and $\hat{C}_L$ represents the magnitude of lift variation in time. We will treat the coefficient $\hat{C}_L$ as a constant independent of position and therefore the unsteady forcing as a purely sinusoidal addition, but future studies may consider more complex models for unsteady forcing. As observed by Assi et al. [8], an individual vortex configuration was not repeatable. Therefore, we use this simplified framework in the present work.

The resulting governing equation for the motion of the trailing cylinder is given by the following equation,

$$m\ddot{y} + c\dot{y} + ky - \frac{1}{2}\rho LDU^2\bar{C}_L = \frac{1}{2}\rho LDU^2\hat{C}_L \cos(2\pi f_{St}t). \tag{2.11}$$

If we substitute $m = (m^* + c_A)\rho\pi\frac{1}{4}LD^2$ where c_A is the coefficient of added mass, $y^* = y/D$,

and $t^* = tU/D$, we find the following nondimensionalized equation of motion,

$$\ddot{y}^* + \frac{4c}{(m^* + c_A)\rho\pi LDU}\dot{y}^* + \frac{4k}{(m^* + c_A)\rho\pi LU^2}y^* - \frac{2}{\pi(m^* + c_A)}\bar{C}_L$$
$$= \frac{2}{\pi(m^* + c_A)}\hat{C}_L\cos(2\pi D/Uf_{St}t^*). \tag{2.12}$$

As we are considering a transversely oscillating cylinder in the wake of a fixed upstream cylinder, the trailing cylinder is constrained such that the transverse displacement y is the free variable in the system and the streamwise displacement x^* is a fixed parameter of the experimental apparatus. Therefore, we can use a Taylor approximation for y^* about the wake centerline, treating x^* as a fixed parameter. This gives the relevant nonlinear spring coefficients, which can be used to analyze the system as a forced harmonic oscillator with nonlinear stiffness. Based on the symmetry of the system, the lift coefficient is an odd function about $y^* = 0$. For now, consider this expansion up to fifth order simply as $\bar{C}_L = C_1y^* + C_3y^{*3} + C_5y^{*5} + \mathcal{O}(y^{*7})$.

$$\ddot{y}^* + \frac{4c}{(m^* + c_A)\rho\pi LDU}\dot{y}^* + \frac{4k}{(m^* + c_A)\rho\pi LU^2}y^*$$
$$- \frac{2}{\pi(m^* + c_A)}\left(C_1y^* + C_3y^{*3} + C_5y^{*5}\right) = \frac{2}{\pi(m^* + c_A)}\hat{C}_L\cos(2\pi St t^*). \tag{2.13}$$

From this expansion, we can define an effective stiffness and natural frequency based on the nondimensionalized linear component of wake stiffness and the structural stiffness,

$$k_{\text{eff}} = \frac{2k}{\rho LU^2} - C_1,$$
$$\omega_{\text{eff}} = \sqrt{\frac{2}{\pi(m^* + c_A)}k_{\text{eff}}}. \tag{2.14}$$

With this effective natural frequency, we rescale time by $T = \omega_{\text{eff}}t^*$, and define our damping ratio by

$$\zeta = \frac{4c}{(m^* + c_A)\rho\pi LDU\omega_{\text{eff}}} = \frac{4c}{LDU\sqrt{2\pi(m^* + c_A)k_{eff}}}, \tag{2.15}$$

to give our final rescaled equations of motion

$$\ddot{y}^* + \zeta\dot{y}^* + y^* - \frac{C_3}{k_{\text{eff}}}y^{*3} - \frac{C_5}{k_{\text{eff}}}y^{*5} = \frac{\hat{C}_L}{k_{\text{eff}}}\cos\left(2\pi\text{St}\omega_{\text{eff}}T\right) \tag{2.16}$$

This rescaling allows for several interesting observations. In the absence of wake forcing, the damping ratio is given by $\zeta = c/2\sqrt{k(m + m_A)}$, matching the damping ratio for vortex-induced vibration [43]. In the case of no structural stiffness, the effective stiffness matches the linear wake stiffness of Assi et al. [13]. In this rescaling, both the effective stiffness and damping ratio become velocity dependent. For small velocities, the stiffness is dominated by the structural stiffness, while for large velocities, wake stiffness dominates. This observation compares very well with [8], where the observed frequencies follow two different trends before and after the lock-in region similar to a single cylinder undergoing vortex-induced vibration. Finally, assuming that the "forcing" of individual vortex shedding occurs at the same frequency of a fixed circular cylinder, St ≈ 0.2, the forcing frequency in this rescaled equation is given by $2\pi\text{St}\omega_{\text{eff}} \approx 1.257\omega_{\text{eff}}$.

To generate realistic coefficients for this model, we will use the Blevins model for lift coefficient given by (2.8) in a system with no structural stiffness, $k = 0$. For a transversely oscillating cylinder, x^* is an input parameter determined by the system, and y^* is the independent variable. Taking a Taylor expansion of (2.8) about the wake centerline, we find the nonlinear expansion of the lift coefficient,

$$C_L\left(y^*; x^*\right) = \left(-\frac{A_1 A_3 C_{D0}}{(x^*)^2} + \frac{A_3 C_{D0}^{0.5}}{(x^*)^{1.5}}\right)y^* + \left(\frac{2A_1 A_2 A_3}{(x^*)^3} - \frac{A_2 A_3}{C_{D0}^{0.5}(x^*)^{2.5}}\right)y^{*3}$$
$$+ \left(\frac{-2A_1 A_2^2 A_3}{C_{D0}(x^*)^4} + \frac{A_2^2 A_3}{2C_{D0}^{1.5}(x^*)^{3.5}}\right)y^{*5} + \mathcal{O}(y^{*7}). \tag{2.17}$$

Using the reported coefficients A_i and a free stream drag coefficient of $C_{D0} = 1.3$ from Blevins [37], the functions for this expansion become

$$C_L\left(y^*; x^*\right) = \left(\frac{12.72}{(x^*)^2} - \frac{11.61}{(x^*)^{1.5}}\right)y^* + \left(-\frac{95.4}{(x^*)^3} + \frac{43.54}{(x^*)^{2.5}}\right)y^{*3} + \left(\frac{357.75}{(x^*)^4} - \frac{81.64}{(x^*)^{3.5}}\right)y^{*5} \tag{2.18}$$

For $x^* = 4$, this gives,

$$C_L(y^*) = -0.649y^* - 0.183y^{*3} + 0.724y^{*5}. \tag{2.19}$$

This result compares very favorably with the linear fit in Figure 2.2 of $\partial C_L/\partial y^* = -0.65$ [13]. The development of this framework allows for a more accurate description of the dynamics, and because this expression models fluid forcing, the wake forcing can be added directly with structural stiffness to produce an overall stiffness, k_{eff} as given in (2.14).

2.3.1 Resonance of nonlinear wake stiffness

As the wake of a fixed upstream cylinder presents a nonlinear stiffness on the downstream cylinder, we can analyze the nonlinear resonance of this effective stiffness on the downstream cylinder. Using the nondimensionalized form of the equations of motion given by (2.16) and negligible damping $\zeta = 0$, we can assume a solution of the form

$$y^* = K_1 \cos\left(\omega_F T\right) + K_3 \cos\left(3\omega_F T\right) + K_5 \cos\left(5\omega_F T\right). \tag{2.20}$$

where $\omega_F = 2\pi \text{St} \omega_{eff} \approx 0.1257$ represents the forced frequency.

Substituting the assumed solution of (2.20) into the rescaled equations of (2.16), we find the full expanded solution,

$$
\begin{aligned}
-K_1 \omega_F^2 \cos\left(\omega_F T\right) &- 9 K_3 \omega_F^2 \cos\left(3\omega_F T\right) - 25 K_5 \omega_F^2 \cos\left(5\omega_F T\right) + \\
& K_1 \cos\left(\omega_F T\right) + K_3 \cos\left(3\omega_F T\right) + K_5 \cos\left(5\omega_F T\right) - \\
& \frac{C_3}{k_{\text{eff}}} \left(K_1 \cos\left(\omega_F T\right) + K_3 \cos\left(3\omega_F T\right) + K_5 \cos\left(5\omega_F T\right)\right)^3 - \\
& \frac{C_5}{k_{\text{eff}}} \left(K_1 \cos\left(\omega_F T\right) + K_3 \cos\left(3\omega_F T\right) + K_5 \cos\left(5\omega_F T\right)\right)^5 \\
& \hspace{4cm} = \frac{\hat{C}_L}{k_{\text{eff}}} \cos\left(\omega_F T\right)
\end{aligned} \tag{2.21}
$$

Using the trigonometric identities $\cos^3\left(\omega_F T\right) = \frac{3}{4}\cos\left(\omega_F T\right) + \frac{1}{4}\cos\left(3\omega_F T\right)$ and $\cos^5\left(\omega_F T\right) = \frac{10}{16}\cos\left(\omega_F T\right) + \frac{5}{16}\cos\left(3\omega_F T\right) + \frac{1}{16}\cos\left(5\omega_F T\right)$, and assuming ordered coefficients $K_1 > K_3 > K_5$, we neglect coefficients less than K_1^3 and can replace the nonlinear terms with their

leading order.

$$
\begin{aligned}
-K_1\omega_F^2\cos\left(\omega_F T\right) - 9K_3\omega_F^2\cos\left(3\omega_F T\right) - 25K_5\omega_F^2\cos\left(5\omega_F T\right) + \\
K_1\cos\left(\omega_F T\right) + K_3\cos\left(3\omega_F T\right) + K_5\cos\left(5\omega_F T\right) - \\
\frac{C_3}{k_{\text{eff}}}K_1^3\left(\frac{3}{4}\cos\left(\omega_F T\right) + \frac{1}{4}\cos\left(3\omega_F T\right)\right) - \\
\frac{C_5}{k_{\text{eff}}}K_1^5\left(\frac{10}{16}\cos\left(\omega_F T\right) + \frac{5}{16}\cos\left(3\omega_F T\right) + \frac{1}{16}\cos\left(5\omega_F T\right)\right) \\
= \frac{\hat{C}_L}{k_{\text{eff}}}\cos\left(\omega_F T\right)
\end{aligned}
\tag{2.22}
$$

Gathering coefficients of $\cos(\omega_F T)$, we find that the nonlinear resonance is given by,

$$
\left(1 - \omega_F^2\right)K_1 - \frac{3C_3}{4k_{\text{eff}}}K_1^3 - \frac{10C_5}{16k_{\text{eff}}}K_1^5 = \frac{\hat{C}_L}{k_{\text{eff}}}.
\tag{2.23}
$$

Similarly, for coefficients of $\cos(3\omega_F T)$ and $\cos(5\omega_F T)$, we find an expression for K_3 and K_5,

$$
\begin{aligned}
K_3 &= \frac{1}{1 - 9\omega_F^2}\left(\frac{C_3}{4k_{\text{eff}}}K_1^3 + \frac{5C_5}{16k_{\text{eff}}}K_1^5\right) \\
K_5 &= \frac{1}{1 - 25\omega_F^2}\frac{C_5}{16k_{\text{eff}}}K_1^5
\end{aligned}
\tag{2.24}
$$

Note that these expressions hold only when $1 - 9\omega_F^2 \neq 0$ and $1 - 25\omega_F^2 \neq 0$ respectively. In the case that these expressions approach these singular points, neglected terms must be considered to determine the magnitude of K_3 and K_5.

2.4 Extended Model

With this idea of nonlinear wake stiffness, we turn our attention to the improving the full nonlinear model for quasi-steady fluid forces acting on the downstream body. An effective model for fluid force coefficients is essential to a nonlinear analysis of wake stiffness. As discussed previously, several models of the fluid forcing in a cylinder wake have been developed in the literature, and just as the Blevins [37] model extends the Huse et al. [40] model based on experimental data, we seek to extend the Blevins model here.
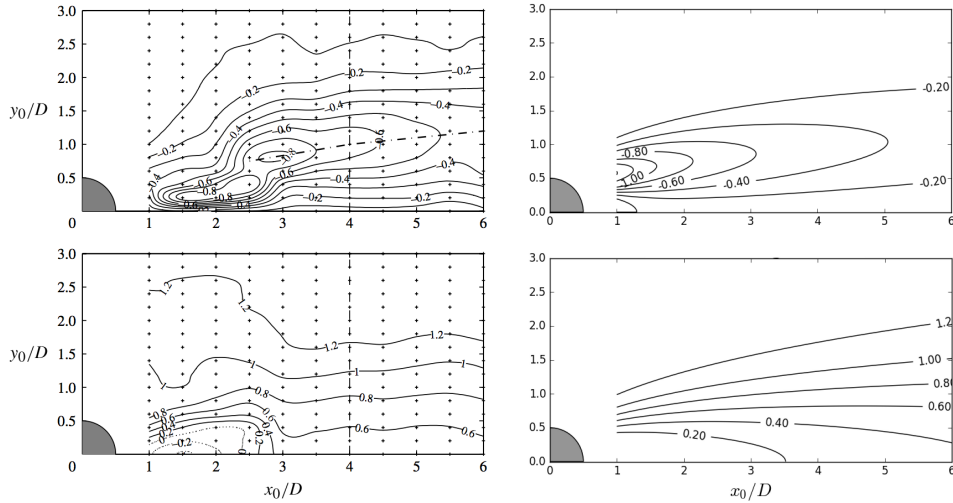
Figure 2.3: The experimental results of Assi et al. [8] (left) compared with the semi-analytical model of Blevins [37] (right) for both quasi-steady lift (top) and quasi-steady drag (bottom). The left column is reproduced from [8], while the right column is a representation of the Blevins model of (2.6) and (2.8) designed for comparison with the left column.

We make several key observations about the physics of fluid forcing in the wake and the resulting mathematical models associated with those physics, and combine these into a cohesive model, which may be applied through polynomial expansions as above in Sec. 2.4 or as fully nonlinear functions to predict flow-induced vibration in the wake of an upstream bluff body. Using the experimental data of [8, 10, 39, 41], we fit the analytical forms of our updated model to experimental data to form this updated semi-analytical model.

2.4.1   Negative drag in the near wake

The Blevins [37] model does an excellent job of capturing the quasi-steady fluid forces throughout the wake of an upstream cylinder for most cylinder spacings, but begins to break down for smaller spacings, such as $x^* = 3$, as can be seen in Figure 2.3, which compares data from [8] and the model of [37]. The figure shows that the Blevins model over-predicts drag coefficient in the near wake. Blevins himself states that his model for velocity deficit "can be expected to be valid when x exceeds a few cylinder diameters" [37]. In the near wake, the drag force actually becomes negative, allowing thrust on the downstream cylinder toward the upstream cylinder [44].

The observation that drag may be negative in the near wake leads to the first key observation in our updated fluid force model. The Blevins model relies on the idea of Eq. (2.5) that drag force is proportional to the square of velocity, $F_x \propto C_D U^2$. However, this definition only admits positive values for drag, even if the direction, and therefore sign, of velocity changes. Because the drag force acts in the same direction as the flow, it is more accurate to consider $F_x \propto C_D U |U|$, which gives us the following expression for an updated drag coefficient based on changes in velocity,

$$C_D\left(x^*, y^*\right) U_0^2 = C_{D0} U\left(x^*, y^*\right) \left|U\left(x^*, y^*\right)\right|. \tag{2.25}$$

This expression for drag allows negative values of drag by including the sign of the velocity U in the expression. As a result of this modification, the lift expression will also need to be modified, because $\frac{d}{dy}\left[u(y)\left|u(y)\right|\right] = \left|u(y)\right| \frac{du}{dy}$. This subtle change in expression for drag, and therefore lift, allows for the possibility of the negative drag in the near wake, and represents our first update to the [37] model.

2.4.2   Critical spacing

The distinction between flow behavior above and below a few diameters of streamwise separation is consistent with the idea of a critical spacing between two observed phenomena of flow around tandem cylinders [3, 4]. Above this critical spacing, the trailing cylinder experiences *wake-induced vibration*, in which the vortex wake from the upstream cylinder drives the vibration of the trailing cylinder [8]. Below the critical spacing, there is not enough space for a vortex wake to form in the gap, and the trailing cylinder undergoes *gap flow switching* (GFS). The flow switches from moving around the two cylinders as an extended body to flowing through the gap between the cylinders. This gap flow drives the oscillations [14]. For fixed cylinders, this lack of vortex shedding leads to a decreased drag in the near wake, causing negative drag for small spacings discussed previously. The location of the critical spacing between the two regimes has been discussed and debated but exists somewhere in the range $3.0 \leq x^* \leq 5$ [3]. Fig. 2.1 above shows many of the reported values.

Because of the change in phenomena at the critical spacing, we propose dividing the model for fluid forcing at the critical spacing and fitting coefficients separately below and above the critical spacing. Previous observations of critical spacing have observed that the transition between fluid force regimes happens very rapidly, and the location of the critical spacing

seems to occur at different places for different experimental setups. Therefore, we consider independent models for fluid forces below the critical spacing and flow above the critical spacing. For convenience, we will refer to these as the gap region, below the critical spacing, and the wake region, beyond the critical spacing, in which a fully developed wake can develop between the cylinders. The gap and wake regions will be denoted by the subscripts g and w respectively. Therefore, the model becomes,

$$
\begin{aligned}
C_D &= \begin{cases} C_{D,g}, & x^* \leq x_c^* \\ C_{D,w}, & x^* > x_c^* \end{cases} \\
C_L &= \begin{cases} C_{L,g}, & x^* \leq x_c^* \\ C_{L,w}, & x^* > x_c^* \end{cases}
\end{aligned}
\tag{2.26}
$$

where x_c^* represents the dimensionless critical spacing.

Because we are considering the region of the wake where the velocity approaches zero, we make one more modification to the drag in the gap region. The solutions for velocity that we are using are based on asymptotic relationships in fully developed flow in the absence of a second cylinder. It is unlikely, then, that the stagnation point of the mean velocity field occurs at the same location as the zero of the drag coefficient function. Therefore, we allow for an additive constant to be added to the drag coefficient expression in the gap region, A_0, g. In order for the drag coefficient to match the free stream drag coefficient $C_D \to C_{D0}$ as $y \to \infty$, the additive coefficient must also be subtracted from C_{D0}, giving the final expression for lift as,

$$
\begin{aligned}
C_D &= \begin{cases} A_{0,g} + (C_{D0} - A_{0,g})u_g\,|u_g|, & x^* \leq x_c^*, \\ C_{D0}u_w\,|u_w|, & x^* > x_c^*, \end{cases} \\
u &= 1 - A_1\sqrt{\frac{C_{D0}}{x^*}}\,\exp\left[\frac{-A_2 y^{*2}}{C_{D0}x^*}\right].
\end{aligned}
\tag{2.27}
$$

2.4.3 Lift dependence on drag

Many papers, including [37], [38], and [45], cite a statement by C.B. Rawlins in the "discussion of [42]" in asserting that the lift coefficient in a wake is proportional to the derivative

of drag coefficient with respect to the dimensionless transverse spacing. That is,

$$C_L(x^*, y^*) \propto \frac{\partial C_D(x^*, y^*)}{\partial y^*} \tag{2.28}$$

With the data that we have assembled from different sources for this study, we can test this assumption against experimental data. To do so, we linearly interpolate the drag coefficient data to the location of measured lift and take a finite difference of the resampled drag coefficients to approximate their derivate. In Figure 2.4, we plot this numerical derivative of the drag coefficients with respect to transverse spacing on the horizontal axis against the corresponding lift coefficient on the vertical axis. The slopes of the various linear regressions are shown in Figure 2.5. If their relationship is linear, then we can confirm the C.B. Rawlins postulate in Eq. (2.28) to be true.

From the results of the linear regression in Figs. 2.4 and 2.5, two observations can be made. The first is that C.B. Rawlins postulate is reasonable for each streamwise spacing x^*. Each figure shows an approximately linear relationship between lift coefficient and the transverse derivative of drag coefficient. The second is that the slope of this linear relationship varies with streamwise spacing, x^*. For a given streamwise position, the lift coefficient varies linearly with the transverse derivative of drag, but streamwise variation of the lift coefficient is also possible. Beyond the critical spacing around $x^* \approx 4.0$, the behavior of the lift coefficient follows less of a clear trend. Therefore, we follow previous work and keep the lift coefficient constant beyond the critical spacing. This change is given by,

$$C_L(x^*, y^*) = \begin{cases} A_{3,g} x^* \frac{\partial C_{D,g}}{\partial y^*}, & x^* \leq x_c^*, \\ A_{3,w} \frac{\partial C_{D,w}}{\partial y^*}, & x^* > x_c^*. \end{cases} \tag{2.29}$$

As a remark, the distinction between the linear change in lift coefficient observed below the critical spacing and other changes in lift coefficient observed above the critical spacing provides a novel metric for finding the critical spacing, adding to metrics such as the Strouhal number, drag coefficient, and observed flow structure. This possible metric and its accuracy in determining the critical spacing in comparison with other methods is worthy of further experimental investigation.
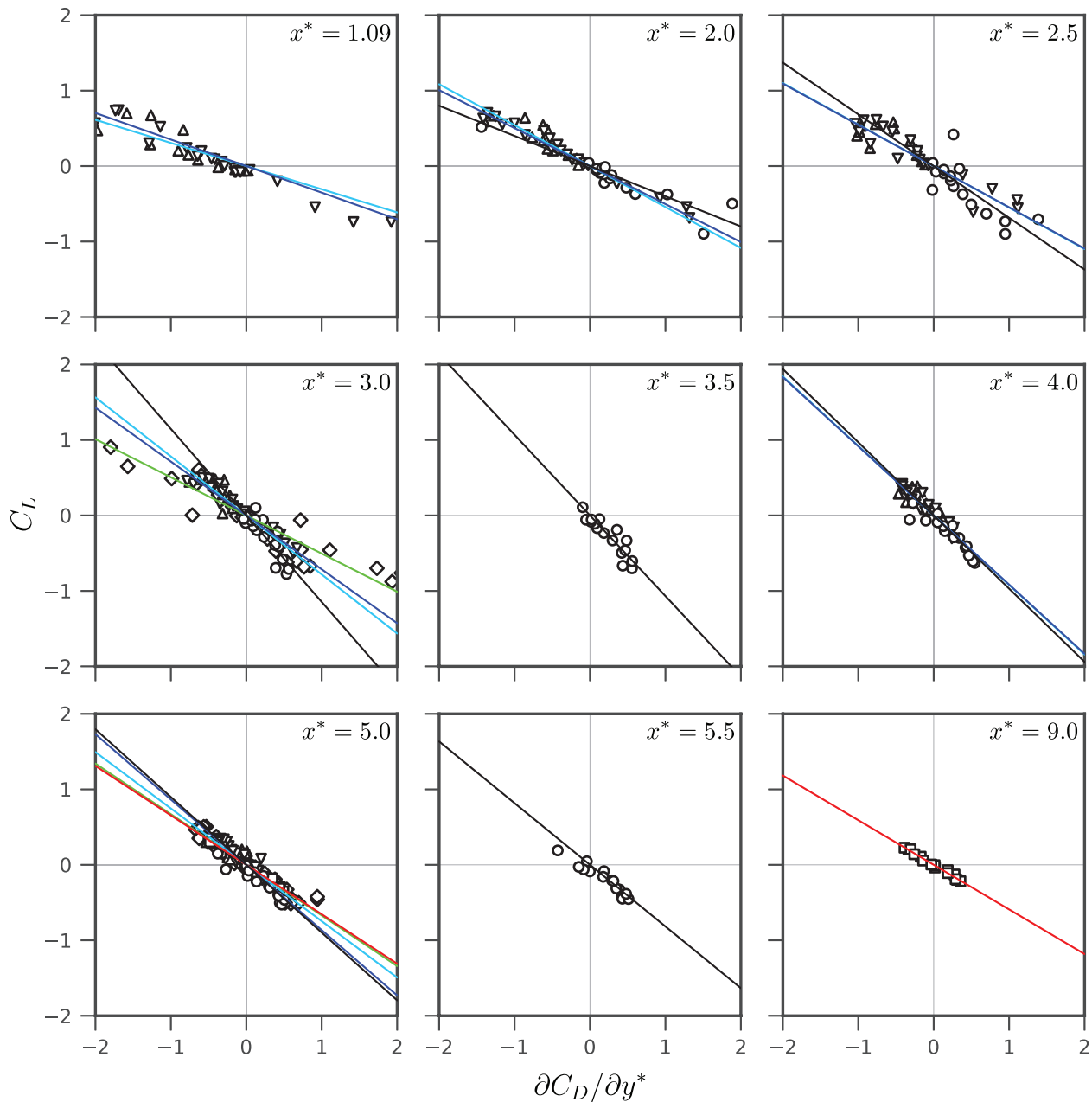
Figure 2.4: Experimental observation of C.B. Rawlins postulate (2.28) that lift is proportional to the transverse derivative of drag. The straight lines represent linear regression of each data set. The symbols and line colors represent different experimental sources: ∘, black, [8]; □, red, [41]; ◇, green, [39]; △, cyan, [10, $Re = 5900$]; ▽, blue, [10, $Re = 2600$].
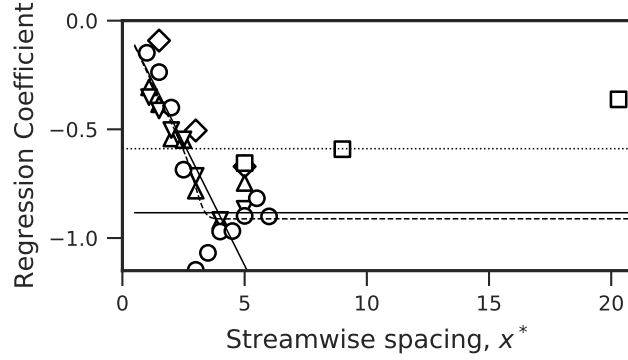
Figure 2.5: The slope of the linear regression for each data set. The dotted line represents the slope predicted by [37], the solid line represents the present expanded piecewise model, and the dashed line represents the smooth model. As above, the symbols represent different experiments: ○, [8]; □, [41]; ◇, [39]; △, [10, $Re = 5900$]; ▽, [10, $Re = 2600$].

2.4.4   Piecewise model

We combine all of the assumptions given above into a single model for fluid forces in the wake. First, we consider the expressions for fluid velocity modification in the wake, $u = U(x^*, y^*)/U_0$ for both the near wake (gap flow region) and far wake (wake-interference region), given by the subscripts g and w respectively.

$$
\begin{aligned}
u_g &= \left(1 - A_{1,g}\frac{C_{D0}}{x^*}\exp\left(\frac{-A_{2,g}y^{*2}}{C_{D0x^*}}\right)\right) \\
u_w &= \left(1 - A_{1,w}\frac{C_{D0}}{x^*}\exp\left(\frac{-A_{2,w}y^{*2}}{C_{D0x^*}}\right)\right)
\end{aligned}
\tag{2.30}
$$

As the free stream drag coefficient C_{D0} must be equal outside of the effects of the wake, this value remains constant. With these expressions for velocity, we define the resulting drag coefficients to be,

$$
\begin{aligned}
C_{D,g} &= A_{0,g} + (C_{D0} - A_{0,g})\, u_g\, |u_g|\,, \\
C_{D,w} &= C_{D0}u_w\, |u_w|\,.
\end{aligned}
\tag{2.31}
$$

These expressions for drag have squared dependence on the velocity, but change sign with the changing sign of velocity. The additive constant $A_{0,g}$ has also been added (and subtracted) to allow for further drag reduction in the gap.

The lift coefficients in the piecewise fluid force model are given by,

$$
\begin{aligned}
C_{L,g} &= A_{3,g} x^* \left|u_g\right| \left(\frac{C_{D0}}{x^*}\right)^{1/2} \frac{y^*}{x^*} \exp\left(\frac{-A_{2,g} y^{*2}}{C_{D0 x^*}}\right), \\
C_{L,w} &= A_{3,w} \left|u_w\right| \left(\frac{C_{D0}}{x^*}\right)^{1/2} \frac{y^*}{x^*} \exp\left(\frac{-A_{2,w} y^{*2}}{C_{D0 x^*}}\right).
\end{aligned}
\tag{2.32}
$$

This updated model follows the linear change in lift coefficient A_3 in the gap flow region shown in Figure 2.5

With the final update given by (2.31) for drag and (2.32), the model contains 7 degrees of freedom.

After fitting the data using a Nelder-Mead simplex search algorithm, we find the following coefficients for use in Eqs. (2.31) and (2.32),

$$
\begin{aligned}
A_{0,g} &= -7.79 \\
A_{1,g} &= 0.0965 & A_{1,w} &= 0.630 \\
A_{2,g} &= 2.76 & A_{2,w} &= 3.41 \\
A_{3,g} &= -1.68 & A_{3,w} &= -7.59
\end{aligned}
\tag{2.33}
$$

The results of this piecewise model can be seen in comparison with experimental data with the solid lines in Figures 2.6 and 2.7, in comparison with the drag at the wake centerline with the solid lines in Figure 2.9, and as a contour plot in Figure 2.8. This piecewise model will be most useful when it is known which wake regime the trailing cylinder will inhabit. However, the critical spacing is not always known, and a cylinder is rarely guaranteed to remain within one regime or the other. To account for these possibilities a smooth model may be preferable.

2.4.5 Smooth fluid force model

For use of a fluid force model in practice, a smooth model is typically preferable to a piecewise model. Therefore, we introduce a model which includes a smooth transition between the two regimes of the piecewise model considered above. Therefore, we introduce a set of smooth weighting functions $\phi_1(x)$ and $\phi_2(x)$ that always add to equal exactly one, $\phi_1(x) + \phi_2(x) =$
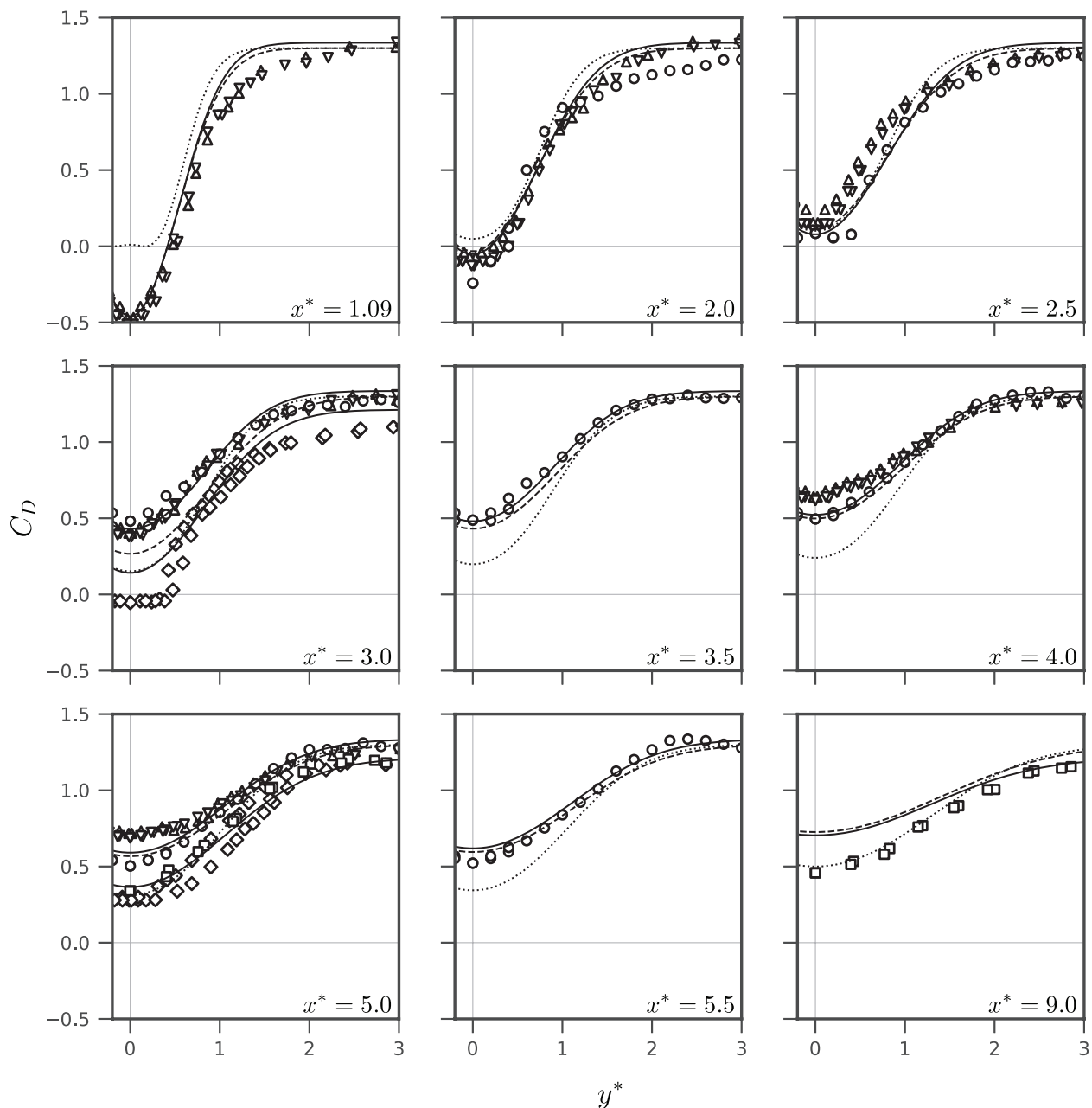
Figure 2.6: Comparison of modeled and experimental drag coefficients plotted against transverse displacement y^* at a variety of streamwise displacements x^*. The proposed piecewise model is given by the solid line, the smooth model is given by the dashed line, and the Blevins [37] model is given by the dotted line. The symbols represent different experiments: ∘, [8]; □, [41]; ◊, [39]; △, [10, $Re = 5900$]; ▽, [10, $Re = 2600$].
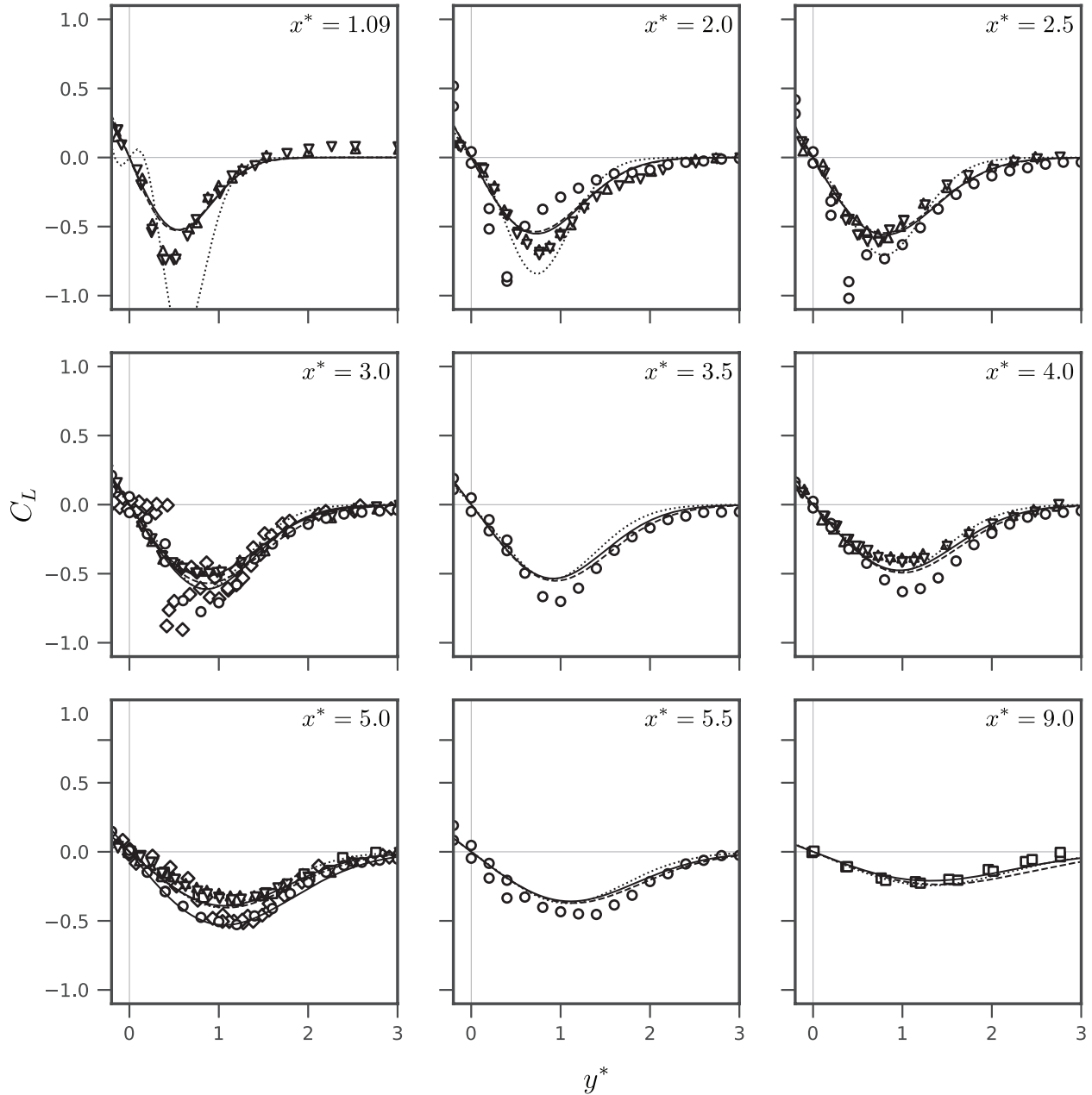
Figure 2.7: Comparison of modeled and experimental lift coefficients plotted against transverse displacement y^* at a variety of streamwise displacements x^*. The proposed piecewise model is given by the solid line, the smooth model is given by the dashed line, and the Blevins [37] model is given by the dotted line. The symbols represent different experiments: $\circ$, [8]; $\square$, [41]; $\diamond$, [39]; $\triangle$, [10, $Re = 5900$]; $\triangledown$, [10, $Re = 2600$].
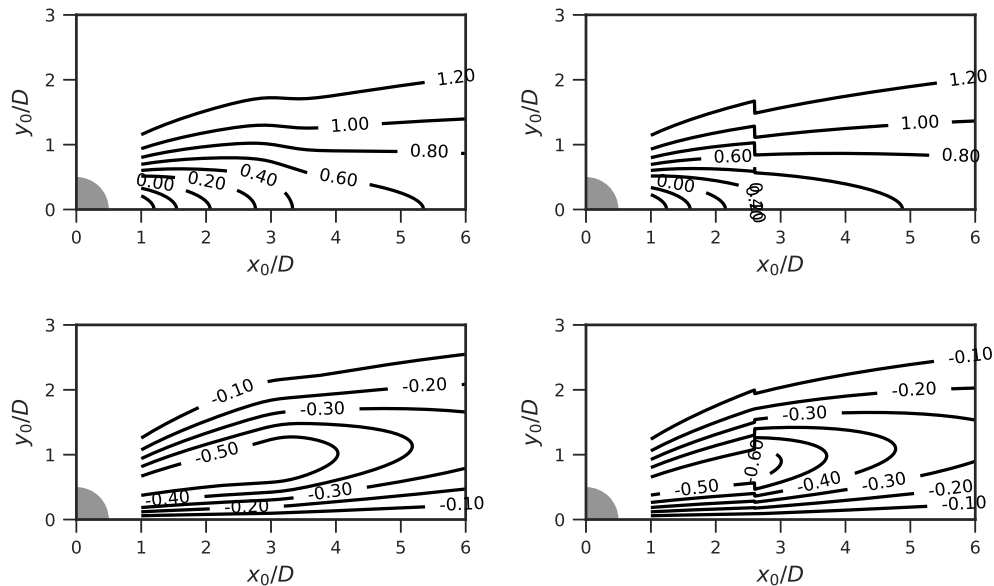
Figure 2.8: Contour plots of the smooth (left) and piecewise (right) updated models for comparison with Figure 2.3.
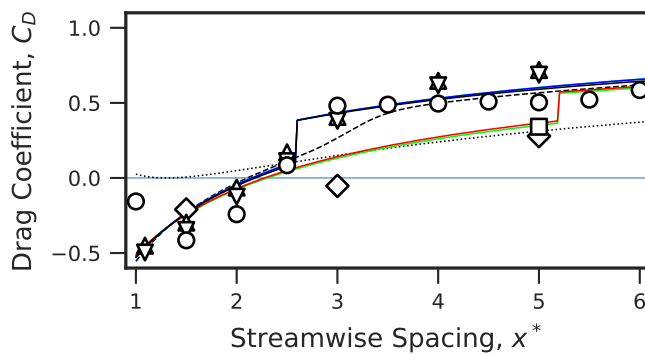
Figure 2.9: A comparison of the drag reduction at the wake centerline for each dataset. For each experimental data set, the drag coefficient measurements are linearly interpolated to identify the drag coefficient at the wake centerline. The symbols represent the different experiments considered: ∘, [8]; □, [41]; ◇, [39]; △, [10], $Re = 5900$; ▽, [10], $Re = 2600$.

$1\forall x$, but remain zero outside of the domain to which they are applied. Such functions may be used to smoothly transition between two unrelated functions, $f(x)$ and $g(x)$ by simply multiplying each by one of the weighting functions ϕ_j and adding them to achieve $F(x) = \phi_1(x)f(x) + \phi_2(x)g(x)$. The resulting function $F(x)$ gives an overall function with $F(x) = f(x)$ where $\phi_1(x) = 1$ and $F(x) = g(x)$ where $\phi_2(x) = 1$ and some combination of the two in between. We will use these weighting functions to fit separate functions for drag and lift in the gap flow region $(C_{D,g}, C_{L,g})$ and the wake-influenced region $(C_{D,w}, C_{L,w})$ and smoothly connect them. The weighting functions we will use are sigmoid functions, defined by,

$$S(x; x_c, \alpha) = \frac{1}{1 + e^{-\alpha(x-x_c)}}. \tag{2.34}$$

The sigmoid function smoothly transitions from 0 to 1 as the value of x increases past the point x_c. The parameter α determines how quickly this transition occurs. In the limit $\alpha \to \infty$, the sigmoid function becomes a step function. The critical value x_c is the transition value, at which $S(x_c; x_c, \alpha) = 0.5$. The weighting functions we will use are $\phi_1(x) = S(x; x_c, -\alpha)$ and $\phi_2(x) = S(x; x_c, \alpha)$. The choice of negative α for ϕ_1 reverses the sign of the exponent in (2.34), giving a function that approaches 1 below the critical spacing and 0 above the critical spacing. This gives the overall lift and drag to be,

$$C_D(x^*, y^*) = C_{D,g}(x^*, y^*)S(x^*; x_c, -\alpha) + C_{D,w}(x^*, y^*)S(x^*; x_c, \alpha),$$
$$C_L(x^*, y^*) = C_{L,g}(x^*, y^*)S(x^*; x_c, -\alpha) + C_{L,w}(x^*, y^*)S(x^*; x_c, \alpha). \tag{2.35}$$

If the critical spacing, or a good approximation of it, is known for a system, a large α allows for close approximation to the piecewise model above. Among the experimental data considered in this paper, different data sets have different critical spacings. Therefore, we allow for a smaller α such that the bistable region reflects behavior between the gap flow and wake-influenced regimes. To ensure that the transition occurs within the bistable region, we choose $\alpha = 5.0$, ensuring that 95% of the transition occurs within a spacing of 1.5 diameters.

We choose $C_{D,g}, C_{D,w}$ defined by (2.31) and $C_{L,g}, C_{L,w}$ defined by (2.32) for the component fluid force functions of (2.35), and allow the critical spacing x_c^* to be discovered by nonlinear regression. All together, this represents an 8 degree-of-freedom model for the data. We again use a Nelder-Mead simplex search algorithm with random initial conditions to identify the
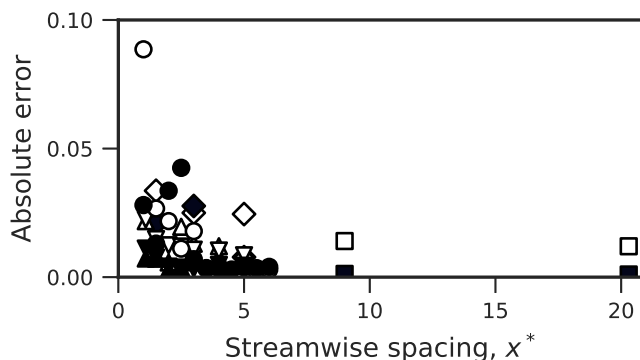
Figure 2.10: A comparison of the absolute error of the smooth function for each dataset. Solid shapes represent the error in lift and open shapes represent error in drag. The symbols represent the various experimental sources: $\circ$, [8]; $\square$, [41]; $\lozenge$, [39]; $\triangle$, [10, $Re = 5900$]; $\triangledown$, [10, $Re = 2600$].

optimal choice of coefficients. From this fit, we discover the coefficients,

$$
\begin{aligned}
x_c^* &= 3.16 \\
A_{0,g} &= -8.63 \\
A_{1,g} &= 0.0863 \qquad A_{1,w} = 0.660 \\
A_{2,g} &= 2.69 \qquad A_{2,w} = 3.44 \\
A_{3,g} &= -1.66 \qquad A_{3,w} = -8.29
\end{aligned} \tag{2.36}
$$

This smooth function is represented by the dashed lines in Figures 2.6, 2.7, and 2.9, and given on the left hand side of Figure 2.8. The absolute squared error of the smooth model for each data set is shown in Figure 2.10. The error is, in general, quite small, and worst at $x^* = 1.0$ from the data of [8]. At this spacing, the cylinders will be nearly touching, and the gap flow takes on a different characteristic.

2.4.6　Comment on force models

We encounter a paradox of sorts when considering the usage of these models. [8] show that the reduced velocity of the wake is not sufficient to induce wake-induced vibration. However, the formulation of the model developed by Blevins and updated in the present work is based on this same mean velocity reduction. The model matches quite well with quasi-steady

experiments. Is the mechanism of wake stiffness a result of the wake velocity reduction? If not, why does the form of wake forcing seem to match the mechanism?

It seems that wake stiffness is caused by mean vortex forcing following the form of velocity reduction, with empirically determined coefficients. It has been experimentally shown, in [8], that a cylinder does not vibrate when allowed to move in a velocity field matching the mean velocity field of a wake without vortex shedding. This, however, does not imply that the restoring force does not exist, or even that it does not follow the form of the mean velocity field. However, it does imply that the additional oscillatory forcing provided by the vortex shedding from the upstream body is necessary to drive the downstream cylinder into its periodic motion, particularly because the stiffness provided by the wake will never match the "lock-in" frequency of the shed vortices of the downstream cylinder. It appears that both the restoring force of the wake stiffness mechanism and the oscillating vortex forcing are required to induce wake-induced vibration.

It is clear, when comparing the various data sets of Figures 2.6 and 2.7, that the differences in experimental setup had a significant impact on the measured fluid forces. Free stream turbulence, Reynolds number, and even the materials used in each experiment provide different results. This is clearest when comparing, for instance, the measured drag at the wake centerline, from Figure 2.9. Therefore, it is preferable to fit a set of equations to experimental data in the same context as the desired situation. However, when collecting quasi-steady lift and drag data is impossible or inconvenient, a model which incorporates the dominant effects will prove very useful in engineering situations of flow-structure interaction. The model introduced in this section accounts for the drag reduction in the wake of a bluff body, the nonlinear stiffness of the wake, and the critical spacing between the extended body regime and the co-shedding regimes.

2.5 Full Nonlinear Wake Stiffness Model

Extending the nonlinear wake model of Section 2.3, we consider motion in both the transverse $y-$ and streamwise $x-$ directions. In the tandem example presented above, nonlinear effects remain small. However, in more general examples nonlinear effects may become increasingly dominant. If, for example, structural stiffness is added with an equilibrium offset from the wake centerline $y_0^* \neq 0$, nonlinear effects will become rapidly more important. If streamwise

motion is allowed, as in the example of clashing of ocean risers [37, 40], a nonlinear stiffness based on our drag model may be considered. A nonlinear model for wake stiffness will allow a variety of experimental configurations to be compared with one another through a common framework. This is essential to further our understanding of flow-induced vibration for multiple bluff bodies.

For the sake of generality, consider that the downstream cylinder is elastically mounted in both the steamwise and transverse directions with elasticity k_x and k_y respectively. These springs are centered about some point (x_{k0}, y_{k0}). Therefore

$$\mathbf{F}_{spring} = \left[\begin{array}{c} -k_x(x - x_{k0}) \\ -k_y(y - y_{k0}) \end{array} \right] \tag{2.37}$$

In addition, consider a general structural damping term of the same form, with damping coefficients c_x and c_y that act linearly on the body.

$$\mathbf{F}_{damping} = \left[\begin{array}{c} -c_x\dot{x} \\ -c_y\dot{y} \end{array} \right] \tag{2.38}$$

To deal with the unsteadiness of the wake forcing, we will consider the standard wake oscillator model [46] as a time-dependent force acting in addition to the quasi-steady wake forces. In general, the fluctuation of the drag force follows $f_D \approx 2f_{St}$, where f_{St} is the Strouhal vortex shedding frequency, because streamwise fluctuation occurs for each of the two vortices in a classical von Kármán wake [44]. Therefore, the fluid forces are given by

$$\mathbf{F}_{wake} = \frac{1}{2}\rho D U^2 \left[\begin{array}{c} \bar{C}_D(x,y) + \hat{C}_D \cos(4\pi f_{St}t) \\ \bar{C}_L(x,y) + \hat{C}_L \cos(2\pi f_{St}t) \end{array} \right] \tag{2.39}$$

where $\bar{C}_D$ and $\bar{C}_L$ are the nonlinear quasi-steady forces on the downstream cylinder as given by Eqs. (2.31) and (2.32) and $\hat{C}_D$ and $\hat{C}_L$ are constant coefficients which give the magnitude of the unsteadiness of wake forces.

Combining these forces, we arrive at the following equations of motion for a trailing cylinder,

$$\begin{aligned} m\ddot{x} + c_x\dot{x} + k_x(x - x_{k0}) - \frac{1}{2}\rho D U^2 \bar{C}_D(x,y) &= \frac{1}{2}\rho D U^2 \hat{C}_D \cos(4\pi f_{St}t) \\ m\ddot{y} + c_y\dot{y} + k_y(y - y_{k0}) - \frac{1}{2}\rho L D U^2 \bar{C}_L(x,y) &= \frac{1}{2}\rho L D U^2 \hat{C}_L \cos(2\pi f_{St}t). \end{aligned} \tag{2.40}$$

Applying the same non-dimensionalization as above, we replace $x^* = x/D$, $y^* = y/D$, $m = (m^* + c_A)\rho\pi\frac{1}{4}LD^2$, and $t^* = tU/D$ to achieve the following non-dimensionalized equations for a system with structural stiffness and nonlinear wake stiffness,

$$
\begin{aligned}
\ddot{x}^* + \frac{4c_x}{(m^* + c_A)\rho\pi LDU}\dot{x}^* &+ \frac{4k_x}{(m^* + c_A)\rho\pi LU^2}(x^* - x_{k0}^*) \\
&- \frac{2}{\pi(m^* + c_A)}\bar{C}_D = \frac{2}{\pi(m^* + c_A)}\hat{C}_D\cos(4\pi D/U f_{St}t^*), \\
\ddot{y}^* + \frac{4c_y}{(m^* + c_A)\rho\pi LDU}\dot{y}^* &+ \frac{4k_y}{(m^* + c_A)\rho\pi LU^2}(y^* - y_{k0}^*) \\
&- \frac{2}{\pi(m^* + c_A)}\bar{C}_L = \frac{2}{\pi(m^* + c_A)}\hat{C}_L\cos(2\pi D/U f_{St}t^*).
\end{aligned}
\tag{2.41}
$$

The first step, then, is to determine the static equilibrium of the system, given by solving the two-dimensional implicit equation,

$$
\begin{aligned}
x_0^* &= \frac{\rho D U^2}{2k_x}\bar{C}_D(x_0^*, y_0^*) + x_{k0}^*, \\
y_0^* &= \frac{\rho D U^2}{2k_y}\bar{C}_L(x_0^*, y_0^*) + y_{k0}^*.
\end{aligned}
\tag{2.42}
$$

Depending on the choice for quasi-steady fluid force equations, the determination of static equilibrium may be possible algebraically. Otherwise, a Newton scheme may be used to find this equilibrium.

Introducing a change of coordinates centered at the static equilibrium, $(\eta_x, \eta_y) = (x^* - x_0^*, y^* - y_0^*)$,

we can do a Taylor expansion of the lift and drag about $(\eta_x, \eta_y) = (0,0)$,

$$
\begin{aligned}
\bar{C}_D(\eta_x + x_0^*, \eta_y + y_0^*) = \bar{C}_D(x_0^*, y_0^*) &+ \frac{\partial \bar{C}_D}{\partial x^*}\eta_x + \frac{\partial \bar{C}_D}{\partial y^*}\eta_y \\
&+ \frac{1}{2}\left(\frac{\partial^2 \bar{C}_D}{\partial x^{*2}}\eta_x^2 + 2\frac{\partial^2 \bar{C}_D}{\partial x^* y^*}\eta_x\eta_y + \frac{\partial^2 \bar{C}_D}{\partial y^{*2}}\eta_y^2\right) \\
&+ \frac{1}{6}\left(\frac{\partial^3 \bar{C}_D}{\partial x^{*3}}\eta_x^3 + 3\frac{\partial^3 \bar{C}_D}{\partial x^{*2}y^*}\eta_x^2\eta_y + 3\frac{\partial^3 \bar{C}_D}{\partial x^* y^{*2}}\eta_x\eta_y^2 + \frac{\partial^3 \bar{C}_D}{\partial y^{*3}}\eta_y^3\right) \\
&+ \mathcal{O}\left(\eta_x^4 + \eta_y^4\right) \\
\bar{C}_L(\eta_x + x_0^*, \eta_y + y_0^*) = \bar{C}_L(x_0^*, y_0^*) &+ \frac{\partial \bar{C}_L}{\partial x^*}\eta_x + \frac{\partial \bar{C}_L}{\partial y^*}\eta_y \\
&+ \frac{1}{2}\left(\frac{\partial^2 \bar{C}_L}{\partial x^{*2}}\eta_x^2 + 2\frac{\partial^2 \bar{C}_L}{\partial x^* y^*}\eta_x\eta_y + \frac{\partial^2 \bar{C}_L}{\partial y^{*2}}\eta_y^2\right) \\
&+ \frac{1}{6}\left(\frac{\partial^3 \bar{C}_L}{\partial x^{*3}}\eta_x^3 + 3\frac{\partial^3 \bar{C}_L}{\partial x^{*2}y^*}\eta_x^2\eta_y + 3\frac{\partial^3 \bar{C}_L}{\partial x^* y^{*2}}\eta_x\eta_y^2 + \frac{\partial^3 \bar{C}_L}{\partial y^{*3}}\eta_y^3\right) \\
&+ \mathcal{O}\left(\eta_x^4 + \eta_y^4\right)
\end{aligned}
\tag{2.43}
$$

where all derivatives are evaluated at the point $(\eta_x, \eta_y) = (0,0)$ which is equivalent to $(x^*, y^*) = (x_0^*, y_0^*)$.

Substituting this expansion of lift and drag into (2.41) to third order gives,

$$
\begin{aligned}
\ddot{\eta}_x + \zeta_x\dot{\eta}_x + \omega_{x,eff}^2\eta_x + \frac{\partial \bar{C}_D}{\partial y^*}\eta_y - h_{D2} - h_{D3} &= \frac{2}{\pi(m^* + c_A)}\hat{C}_D\cos(4\pi\mathrm{St}t^*), \\
\ddot{\eta}_y + \zeta_y\dot{\eta}_y + \frac{\partial \bar{C}_L}{\partial x^*}\eta_x + \omega_{y,eff}^2\eta_y - h_{L2} - h_{L3} &= \frac{2}{\pi(m^* + c_A)}\hat{C}_L\cos(2\pi\mathrm{St}t^*),
\end{aligned}
\tag{2.44}
$$

where, to save space, the 2nd and 3rd order terms are given by,

$$
\begin{aligned}
h_{F2} &= \frac{1}{\pi(m^* + c_A)}\left(\frac{\partial^2 \bar{C}_F}{\partial x^{*2}}\eta_x^2 + 2\frac{\partial^2 \bar{C}_F}{\partial x^* y^*}\eta_x\eta_y + \frac{\partial^2 \bar{C}_F}{\partial y^{*2}}\eta_y^2\right), \\
h_{F3} &= \frac{1}{3\pi(m^* + c_A)}\left(\frac{\partial^3 \bar{C}_F}{\partial x^{*3}}\eta_x^3 + 3\frac{\partial^3 \bar{C}_F}{\partial x^{*2}y^*}\eta_x^2\eta_y + 3\frac{\partial^3 \bar{C}_F}{\partial x^* y^{*2}}\eta_x\eta_y^2 + \frac{\partial^3 \bar{C}_F}{\partial y^{*3}}\eta_y^3\right), \\
F &= \{L, D\}.
\end{aligned}
\tag{2.45}
$$

This expanded framework may be adapted to suit any problem in which a bluff body is allowed to move in the wake of an upstream bluff body. If such a system contains a constraint in the form of $f(x^*, y^*) = 0$, then the constraint may be used to restrict the two degree-of-

freedom system to a one degree-of-freedom oscillator as above in Section 2.3 for the example $x^* = k$.

2.6 Example: tandem, tethered cylinders

As an example of a novel system to which nonlinear wake stiffness may be applied, we consider a pair of circular cylinders in which the upstream cylinder is fixed in place and the trailing cylinder is constrained to move in a circular path around it. The two cylinders are tethered in the sense that the center-to-center distance between them remains constant, denoted by R. Based on this geometry, the constraint on the system may be defined as,

$$x^{*2} + y^{*2} = r^2, \tag{2.46}$$

where $r = R/D$ is the dimensionless fixed distance between the cylinders.
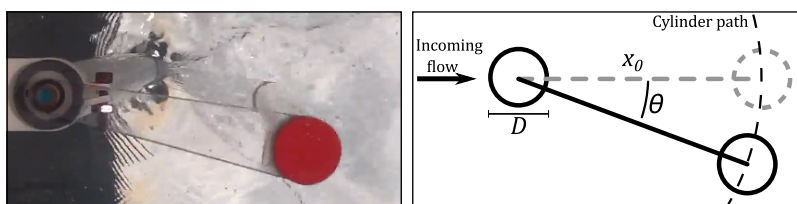
Figure 2.11: (a) A snapshot from experimental data. The trailing cylinder (red) is connected by an acrylic plate to a central rod running through the upstream cylinder. The position of the trailing cylinder is tracked and resulting angular position calculated. (b) Schematic of tethered cylinder system. Both cylinders have the same diameter, D, and the distance between the cylinders is fixed to the length x_0.

2.6.1 Predictions from the model

With this constraint, x and y must be parametrized by the angle θ such that $x^* = r \cos \theta$ and $y^* = r \sin \theta$, where θ is the counterclockwise angle with respect to the direction of the flow. Because of the constraint, forces in the radial direction are matched by the tension or compression in the connector. Therefore, the remaining forces are those that act perpendicular to the radial direction. We can define a resultant force coefficient acting in this direction by,

$$C_\theta = -C_D \sin \theta + C_L \cos \theta \tag{2.47}$$
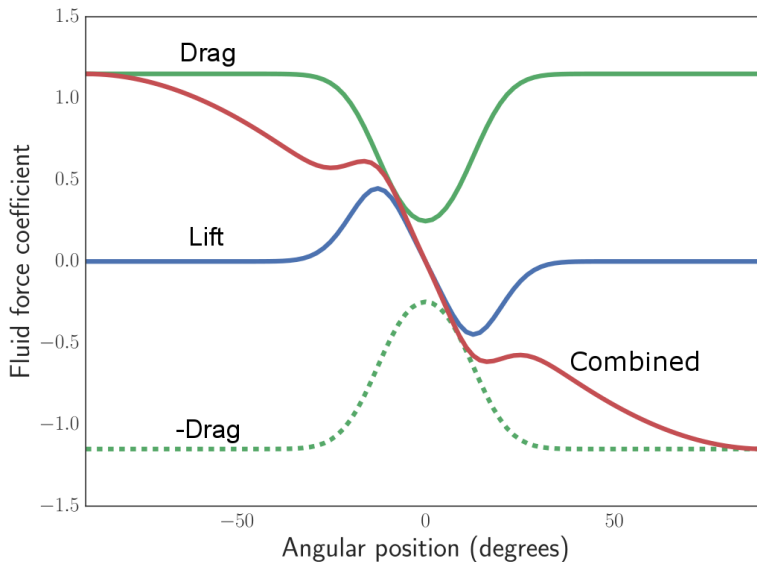
Figure 2.12: The combined fluid force coefficient C_θ defined by (2.47) compared against lift and drag over the range $\theta \in (-90°, 90°)$ at a spacing of $r = 4$.

When the cylinder is oriented directly in tandem with the upstream cylinder, $\theta = 0$, and the direction of motion is aligned with the y-direction. Therefore, $C_\theta = C_L$. Because of the counterclockwise definition of the angle, the force is aligned with drag, $C_\theta = C_D$, when $\theta = -\pi/2$ and aligned opposite drag, $C_\theta = -C_D$, when $\theta = \pi/2$. Fig. 2.12 shows the projection onto the combined C_θ coefficient defined by Eq. (2.47) using the Blevins [37] model for lift and drag at a spacing of $r = 4$. From this figure, it is clear that the linear wake stiffness will dominate, but the contributions of both lift and drag as in Sec. 2.5 are necessary to effectively predict the wake stiffness.

2.6.2   Experimental Setup

In order to compare our predictions with an experimental system, we conducted experiments on a tethered, tandem cylinder system, as shown in Figure 2.11. The upstream cylinder was secured at both ends in order to remain fixed throughout the testing. The trailing cylinder is free to move along a circular arc around the upstream cylinder, connected by two 6.35mm thick plates of acrylic which are visible in Figure 2.11. The system was designed with no structural restoring force; that is, in still water, the trailing cylinder remains wherever it is placed. Therefore, the only forces on the trailing cylinder are fluid forces, constraint forces,

and any system damping.

Tests were conducted in a re-circulating water channel in the AEThER Lab at Virginia Tech. A fixed 2.54 cm PVC cylinder was suspended by an aluminum frame, piercing the free-surface, and mounted to the frame 50.8 cm below the free surface. A trailing 2.54 cm acrylic tube was sealed at both ends and mounted by flat acrylic plates to a 0.64 cm steel shaft in the center of the upstream cylinder at the bottom of the leading cylinder and 10.2 cm below the free surface. The spacing between the cylinders was varied from 3 diameters to 5 diameters, and the flow speed was varied from 18.9 to 44.3 cm/s, giving a Reynolds number range of 4,800 to 11,250.

2.6.3 Experimental Results

By observing solely the kinematics of our system, we were able to observe several interesting behaviors.

Amplitude of Oscillation

In Figure 2.13, we show several different ways to interpret the amplitude signal. The top row of Figure 2.13 shows amplitudes as an angular displacement. However, in typical transverse oscillation studies, the amplitude is reported as dimensionless transverse displacement from the centerline, shown in the bottom row of Figure 2.13 for comparison.

In the left column, we show the mean of the absolute value of all positive and negative peaks in all trials for each test case. Because of the high variability in amplitudes reached during any given trial, we also show the mean of the top 10% of all peaks in the right column. This reflects the work of Hover and Triantfyllou [12], showing the maximum amplitudes of oscillation, and, in comparison with the mean value, the top 10% measurement shows the variation in oscillations.

The angular amplitude decreases as center-to-center spacing increases, and in all cases, amplitude increases with Reynolds number for the entire range tested. The most noticeable difference is between $x_0^* = 3$ and $x_0^* = 3.5$. This trend is also true for the top 10% of angular amplitudes, as shown in the top right corner of Figure 2.13. Surprisingly, the mean transverse amplitudes of oscillation for all $x_0^* \in 3.5, 4, 4.5, 5$ collapse to a single curve. Whatever the
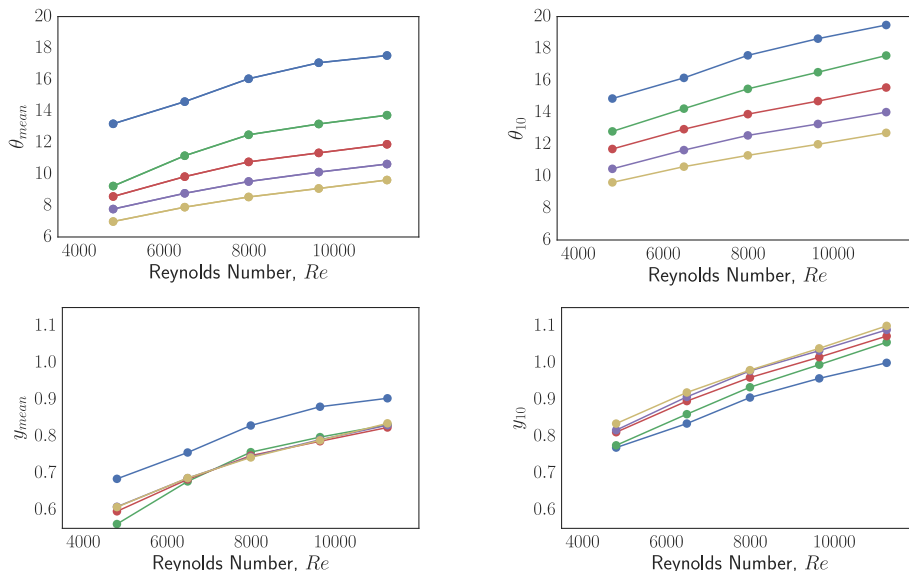
Figure 2.13: This figure shows mean amplitudes of oscillation in both angular distance and transverse position from the centerline. The left column shows the mean of the entire dataset, while the right column shows the mean of the top 10% of amplitudes. The top row represents angular distance, in degrees, while the bottom row represents transverse distance, nondimensionalized by diameter. The colors correspond to Figure 2.15.

cylinder spacing, the trailing cylinder was, on average, displaced the same distance from the wake centerline. However, the case of $x_0^* = 3$ remains distinct from the other cases. Finally, in the bottom right corner of Figure 2.13, we see that the mean of the top 10% of transverse amplitudes increase with center-to-center spacing, counter to angular displacement. Systems with longer connecting-arms have a higher upper bound on transverse displacement.

In the left column, the mean amplitude of oscillation appears to increase with approximately the square root of Reynolds number. It is also true that for low Reynolds numbers, the system does not oscillate at all. The system, therefore, has a single, stable fixed point at $\theta = 0$ for low Reynolds number which bifurcates into a stable periodic orbit about an unstable fixed point for higher Reynolds numbers. If this periodic orbit does indeed increase as the square root of Reynolds number, this represents a Hopf bifurcation in the system.

Frequency Measurements and Wake Stiffness

Figure 2.14 shows the mean power spectral density for each collection of tests. This figure shows the variation of behavior noted previously in the frequency domain. For each case of flow speed and center-to-center spacing, there is one dominant frequency peak and one secondary peak with a lower power intensity. For larger spacings, in particular $x^* = 5$, this secondary peak breaks apart into at least two frequency peaks.
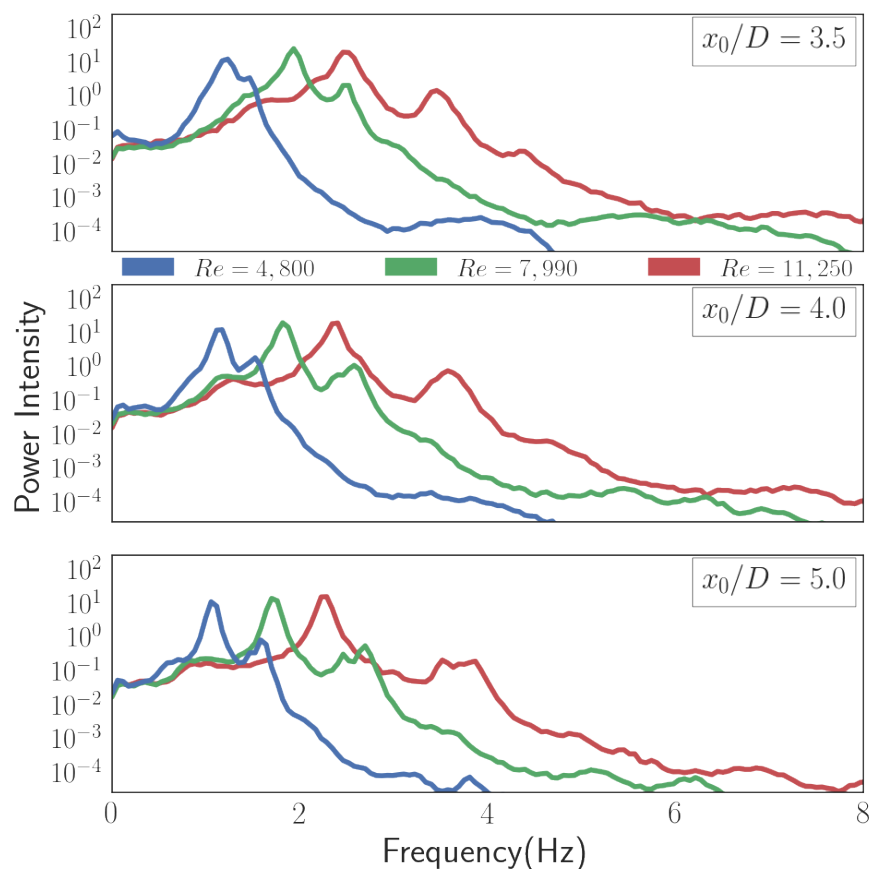
Figure 2.14: Power spectral densities for center-to-center spacings of $x^* = 3.5$ (top), $x^* = 4$ (middle) and $x^* = 5$ (bottom). As Reynolds number increases, the dominant frequencies increase, and the frequency response becomes increasingly broadband.

The secondary frequency peak can be associated with the Strouhal vortex shedding frequency for a cylinder of this size. This explains why the secondary peak is constant across different center-to-center spacings for the same Reynolds number. For the largest spacing, we see the effect of the reduced mean flow velocity that the trailing cylinder sees. The upstream and downstream cylinders have two different vortex shedding frequencies, which causes the

second frequency peak to split in two.

Based on our understanding of the physics of the flow discussed previously, this dominant frequency peak must be associated by the force of the wake on the trailing cylinder, the wake stiffness. We can observe the behavior of this dominant frequency with changing spacing and Reynolds number by numerically finding the location of the maximum of the power spectrum. Fig. 2.15 shows this measured dominant frequency.
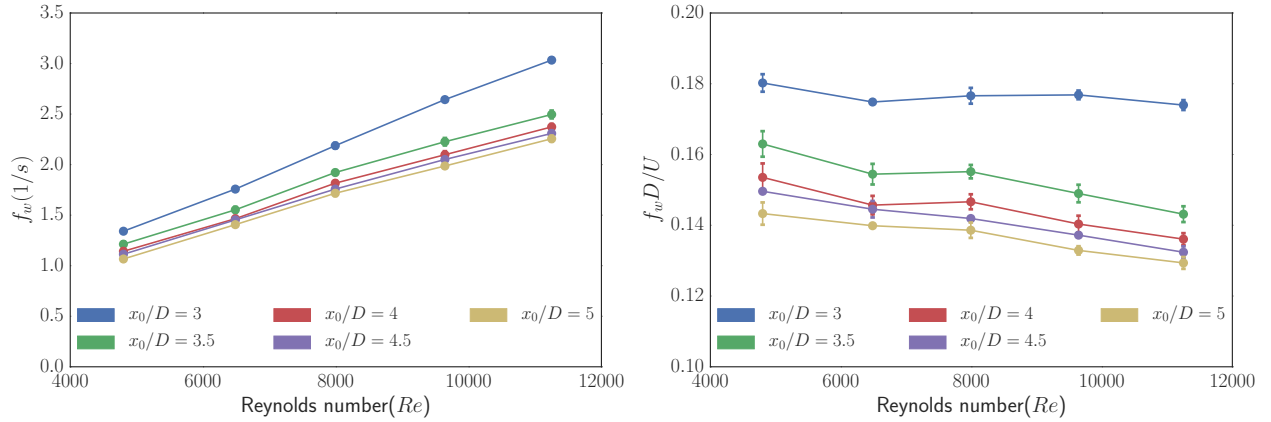
Figure 2.15: (Left) Measured dominant frequency shown for all Reynolds numbers and center-to-center spacings. Dominant frequency is found by numerically finding the power spectrum of measured cylinder kinematics. (Right) Nondimensionalizing this frequency measurement with cylinder diameter and flow velocity gives us the effective dimensionless wake frequency for comparison with Eq. (2.3).

From these frequency measurements, we can make a comparison with linear wake stiffness using the nondimensional wake stiffness parameter, $f_w D/U$ introduced in Eq. (2.3) above. As wake stiffness is assumed to be independent of Reynolds number, we compare each measured frequency with the overall mean frequency in Fig. 2.16. It is clear that, for spacings above the critical spacing, the dimensionless frequency decreases as Reynolds number increases. However, for a spacing of $x^* = 4$, the apparent wake stiffness remains approximately constant.

2.6.4   The Gap Flow Switching Regime

In the experimental results presented above, the gap flow switching behavior stands out from the wake-induced vibration behavior present beyond the critical spacing. Figure 2.13 shows
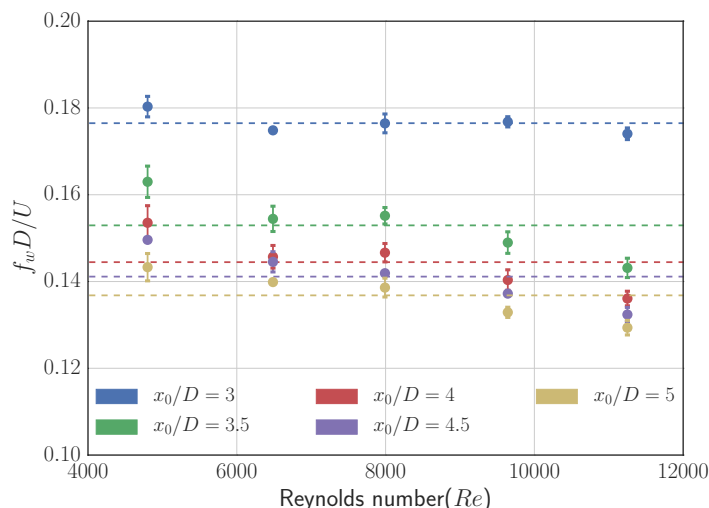
Figure 2.16: Comparison of the data points from above in Fig. 2.15 with the mean apparent wake stiffness value for each spacing.

that a spacing of $r = 3.0$ shows higher amplitudes of oscillation, and Figure 2.15 shows that these high amplitudes are coupled with a higher frequency of oscillation. Another distinction in this regime is the consistency of its oscillations, which we show more clearly in Figure 2.17. To show the nature of its behavior in comparison with other cylinder spacings, we consider both the raw time series from the experiment and its trajectory in phase space in Figure 2.17. The angular velocity has been calculated by taking a simple finite difference of the position data.

In the Wake Induced Vibration case of $x^* = 4$, there is not only inconsistency in the amplitudes of oscillation, but inconsistency in the frequency of oscillation. The 3rd and 4th positive peaks of the time series for $x^* = 4$ are significantly closer in time than the following oscillation. This amplitude and frequency inconsistency is made clear looking at the wide range of values covered in phase space on the right hand side of Figure 2.17. This shows that individual oscillations vary significantly.

2.6.5   Experimental observations

We have provided an example of how the modified Blevins model may be used for a system not previously studied- the tandem, tethered cylinder system. By projecting both the lift and drag curves of the modified Blevins model onto the free direction in our system, we can
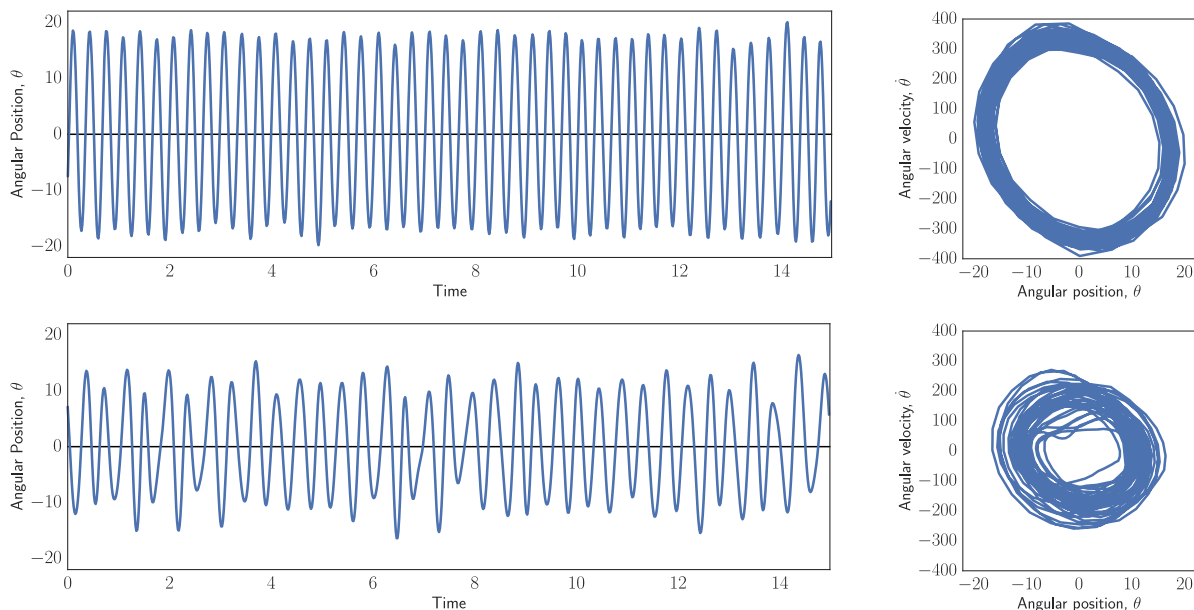
Figure 2.17: Time series of angular displacement (left column) and trajectory in position-velocity space (right column) for a 15 second sample of behavior at $Re = 11,250$ for $x^* = 3$ (top row) and $x^* = 4$ (bottom row)

extrapolate the model to fit our system. This provides a good first step in predicting the behavior of the system.

We have conducted experiments on this tandem, tethered cylinder system to observe the kinematics of the body oscillator and compare its motion with that predicted by the extended Blevins model. We have seen results which support the concept of wake stiffness in flow-structure interaction in the wake of a bluff body. However, there is still a gap between this prediction and the actual observed results. This gap must be attributed to the unsteady dynamics of the fluid oscillator. Given that these experiments solely observe the motion of the body oscillator in the system, we cannot give further insight into the mechanism that the unsteady fluid motion provides. Further investigation into this mechanism seems to be the necessary next steps, much like [8].

From these experiments, we have seen behavior similar to that reported in studies on transversely oscillating cylinders, but with key differences. We see persistent oscillations with inconsistent peaks, which is consistent with the work of Assi et al. [13] and Hover & Triantfyllou [12]. However, we also see a second frequency peak in the displacement signal, which is not reported in Assi et al. [8]. We see lower amplitudes, but higher frequencies in our

system than in Assi et al. [13], which may also be due to the difference in mass ratio.

Finally, we observed the Gap Flow Switching regime for tandem, tethered cylinders. This regime presented many intriguing differences when compared against the Wake Induced Vibration regime. This regime, characterized by smaller center-to-center spacings, produced much more consistent displacements at larger displacement amplitudes and frequencies. Previous observations of this flow regime would explain that there is no incoming vortex wake from the upstream cylinder and forces are given by discrete changes in the flow structure. We have shown that the wake-stiffness approach to modeling this regime is more effective as a model for the gap flow switching regime than for the wake-induced vibration regime for which it was originally developed. The present study highlights a need for a follow-up study to better understand the force mechanisms of this regime of flow-structure interaction.

2.7   Discussion

In the complexity of flow-induced vibrations, more general models are essential for predicting motion of a new system. The idea of the variation of fluid force coefficients having a stiffness-like effect, then becomes a powerful one, providing a stronger intuition for the effects of wake forcing. In this work, we have extended the notion of wake stiffness to consider nonlinear effects of displacement, either through a Taylor expansion of the position or a direct application of a nonlinear function for lift and drag.

We have extended the semi-analytical model of Blevins [37] to incorporate the effects of fluid forcing below the critical spacing, in the regime where the gap between the bodies is too small for a vortex wake to form. To generate this update, we modified the form of the model for drag coefficient based on the observations that the drag coefficient may be negative in the near wake, that forcing fundamentally changes at the critical spacing, and that the zero of the drag coefficient is unlikely to occur at the stagnation point of the asymptotic solution for velocity profile. We have also used existing experimental data to investigate the Rawlins postulate that lift depends on the transverse derivative of drag in the wake. In Figs. 2.7 and 2.5, we show that for a fixed streamwise spacing x^*, lift tends to vary linearly, but the streamwise variation of the relationship between lift and drag is not constant. For the updated lift model, we consider only a linear variation of lift coefficient with streamwise spacing within the gap region, but further investigation of the lift dependence

on spacing is necessary. Experimental investigation in the region $x^* \in (6.0, 20.0)$, where the trailing cylinder is completely beyond the critical spacing, could help uncover the streamwise relationship.

In this work, we have used data from several experimental sources [8, 10, 39, 41] to fit coefficients to the updated semi-analytical governing equations, but in application, it is preferable to fit coefficients to the specific application. Factors such as free stream turbulence and Reynolds number are not accounted for in this model, and their effect on the coefficients of the governing equations will need to be measured for high accuracy in a specific application. However, if quasi-steady experiments are not feasible for a specific application, we have provided both piecewise and smooth models which may be applied to, for example, predictions of oil riser clashing, wire vibrations, and even tandem models of gliding animals [47].

Acknowledgments

Bibliography

[1] Peter W. Bearman. Vortex shedding from oscillating bluff bodies. *Annual Review of Fluid Mechanics*, 16(1):195–222, 1984.

[2] M. M. Zdravkovich. Review of flow interference between two circular cylinders in various arrangements. *Journal of Fluids Engineering*, 99(4):618–633, December 1977. ISSN 0098-2202. doi: 10.1115/1.3448871.

[3] M. M. Zdravkovich. Review of interference-induced oscillations in flow past two parallel circular cylinders in various arrangements. *Journal of Wind Engineering and Industrial Aerodynamics*, 28(13):183–199, August 1988. ISSN 0167-6105. doi: 10.1016/0167-6105(88)90115-8.

[4] D. Sumner. Two circular cylinders in cross-flow: A review. *Journal of Fluids and Structures*, 26(6):849–899, 2010.

[5] D. Brika and A. Laneville. Vortex-induced vibrations of a long flexible circular cylinder. *Journal of Fluid Mechanics*, 250:481–481, 1993.

[6] A. Khalak and C. H. K. Williamson. Motions, forces and mode transitions in vortex-induced vibrations at low mass-damping. *Journal of Fluids and Structures*, 13(7):813–851, 1999.

[7] C.H.K. Williamson and R. Govardhan. Vortex-Induced Vibrations. *Annual Review of Fluid Mechanics*, 36(1):413–455, 2004. doi: 10.1146/annurev.fluid.36.050802.122128.

[8] G. R. S. Assi, P. W. Bearman, and J. R. Meneghini. On the wake-induced vibration of tandem circular cylinders: the vortex interaction excitation mechanism. *Journal of Fluid Mechanics*, 661:365–401, 2010. doi: 10.1017/S0022112010003095.

[9] P. W. Bearman. Circular cylinder wakes and vortex-induced vibrations. *Journal of Fluids and Structures*, 27(56):648–658, July 2011. ISSN 0889-9746. doi: 10.1016/j.jfluidstructs.2011.03.021.

[10] A. Bokaian and F. Geoola. Wake-induced galloping of two interfering circular cylinders. *Journal of Fluid Mechanics*, 146:383–415, September 1984. ISSN 1469-7645. doi: 10.1017/S0022112084001920.

[11] D. Brika and A. Laneville. The flow interaction between a stationary cylinder and a downstream flexible cylinder. *Journal of Fluids and Structures*, 13(5):579–606, July 1999. ISSN 0889-9746. doi: 10.1006/jfls.1999.0220.

[12] F. S. Hover and M. S. Triantafyllou. Galloping response of a cylinder with upstream wake interference. *Journal of Fluids and Structures*, 15(3):503–512, 2001.

[13] G. R. S. Assi, P. W. Bearman, B. S. Carmo, J. R. Meneghini, S. J. Sherwin, and R. H. J. Willden. The role of wake stiffness on the wake-induced vibration of the downstream cylinder of a tandem pair. *Journal of Fluid Mechanics*, 718:210–245, 2013.

[14] M. M. Zdravkovich. Flow-Induced Vibrations of Two Cylinders in Tandem, and their Suppression. In Eduard Naudascher, editor, *Flow-Induced Structural Vibrations*, pages 631–639, Karlsruhe, 1974. Springer-Verlag, Berlin, Germany.

[15] Tamotsu Igarashi. Characteristics of the flow around two circular cylinders arranged in tandem: 1st report. *Bulletin of JSME*, 24(188):323–331, 1981.

[16] Jiro Mizushima and Norihisa Suehiro. Instability and transition of flow past two tandem circular cylinders. *Physics of Fluids*, 17(10):104107, 2005.

[17] Wenchao Yang and Mark A. Stremler. Critical spacing of stationary tandem circular cylinders at $Re \approx 100$. *In preperation*, 2018.

[18] Bruno Souza Carmo, Julio Romano Meneghini, and SJ Sherwin. Possible states in the flow around two circular cylinders in tandem with separations in the vicinity of the drag inversion spacing. *Physics of Fluids*, 22(5):054101, 2010.

[19] Yuji Tasaka, Seiji Kon, Lionel Schouveiler, and Patrice Le Gal. Hysteretic mode exchange in the wake of two circular cylinders in tandem. *Physics of Fluids*, 18(8):084104, 2006.

[20] Tatsuno Huhe-Aode et al. Visual studies of wake structure behind two cylinders in tandem arrangement. *Reports of Research Institute for Applied Mechanics, Kyushu University*, 32(99):1–20, 1985.

[21] Georgios V Papaioannou, Dick KP Yue, Michael S Triantafyllou, and George E Karniadakis. Three-dimensionality effects in flow around two tandem cylinders. *Journal of Fluid Mechanics*, 558:387–413, 2006.

[22] Feifei Tong, Liang Cheng, and Ming Zhao. Numerical simulations of steady flow past two cylinders in staggered arrangements. *Journal of Fluid Mechanics*, 765:114–149, 2015.

[23] Seikan Ishigai, Eiichi Nishikawa, Keiya Nishimura, and Katsuzo Cho. Experimental study on structure of gas flow in tube banks with tube axes normal to flow: Part 1, karman vortex flow from two tubes at various spacings. *Bulletin of JSME*, 15(86): 949–956, 1972.

[24] G Xu and Y Zhou. Strouhal numbers in the wake of two inline cylinders. *Experiments in Fluids*, 37(2):248–256, 2004.

[25] M Kiya, M Arie, H Tamura, and H Mori. Vortex shedding from two circular cylinders in staggered arrangement. *Journal of Fluids Engineering*, 102(2):166–171, 1980.

[26] L Ljungkrona, CH Norberg, and B Sunden. Free-stream turbulence and tube spacing effects on surface pressure fluctuations for two tubes in an in-line arrangement. *Journal of Fluids and Structures*, 5(6):701–727, 1991.

[27] T Kitagawa and H Ohta. Numerical investigation on flow around circular cylinders in tandem arrangement at a subcritical reynolds number. *Journal of Fluids and Structures*, 24(5):680–699, 2008.

[28] Longjun Wang, Md Mahbub Alam, and Yu Zhou. Two tandem cylinders of different diameters in cross-flow: effect of an upstream cylinder on wake dynamics. *Journal of Fluid Mechanics*, 836:5–42, 2018.

[29] MM Zdravkovich and DL Pridden. Interference between two circular cylinders; series of unexpected discontinuities. *Journal of Wind Engineering and Industrial Aerodynamics*, 2(3):255–270, 1977.

[30] Md Mahbub Alam, Md Moriya, K Takai, and H Sakamoto. Fluctuating fluid forces acting on two circular cylinders in a tandem arrangement at a subcritical reynolds number. *Journal of Wind Engineering and Industrial Aerodynamics*, 91(1-2):139–154, 2003.

[31] David Biermann and William H Herrnstein Jr. The interference between struts in various combinations. 1933.

[32] M Arie, M Kiya, M Moriya, and H Mori. Pressure fluctuations on the surface of two circular cylinders in tandem arrangement. *Journal of Fluids Engineering*, 105(2):161–166, 1983.

[33] Atsushi Okajima. Flows around two tandem circular cylinders at very high reynolds numbers. *Bulletin of JSME*, 22(166):504–511, 1979.

[34] I Fylling, C Larsen, N Sødahl, E Passano, A Bech, A Engseth, H Lie, and H Ormberg. *RIFLEX User's Manual 3.6*. MARINTEK, Trondheim, Norway, 2008.

[35] *Orcaflex documentation, Online version 10.2c*. Orcina Ltd., 2018. URL https://www.orcina.com/SoftwareProducts/OrcaFlex/Documentation/. Accessed: 2018-05-15.

[36] Turgut Sarpkaya. A critical review of the intrinsic nature of vortex-induced vibrations. *Journal of Fluids and Structures*, 19(4):389–447, 2004.

[37] Robert D. Blevins. Forces on and Stability of a Cylinder in a Wake. *Journal of Offshore Mechanics and Arctic Engineering*, 127(1):39–45, March 2005. ISSN 0892-7219. doi: 10.1115/1.1854697.

[38] S. J. Price. Wake induced flutter of power transmission conductors. *Journal of Sound and Vibration*, 38(1):125–147, 1975.

[39] S. J. Price and M. P. Paidoussis. The aerodynamic forces acting on groups of two and three circular cylinders when subject to a cross-flow. *Journal of Wind Engineering and Industrial Aerodynamics*, 17(3):329–347, September 1984. ISSN 0167-6105. doi: 10.1016/0167-6105(84)90024-2.

[40] Erling Huse et al. Interaction in deep-sea riser arrays. In *Offshore Technology Conference*. Offshore Technology Conference, 1993.

[41] S. J. Price. The origin and nature of the lift force on the leeward of two bluff bodies. *Aeronautical Quarterly*, 27:154–168, 1976.

[42] A Simpson and SJ Price. Use of damped and undamped quasi-static aerodynamic models in study of wake-induced flutter. In *IEEE Transactions on Power Apparatus and Systems*, number 6, pages 1741–1741. IEEE-INST ELECTRICAL ELECTRONICS ENGINEERS INC 345 E 47TH ST, NEW YORK, NY 10017-2394, 1974.

[43] TL Morse and CHK Williamson. Prediction of vortex-induced vibration response by employing controlled motion. *Journal of Fluid Mechanics*, 634:5–39, 2009.

[44] Michael P Païdoussis, Stuart J Price, and Emmanuel De Langre. *Fluid-structure interactions: cross-flow-induced instabilities*. Cambridge University Press, 2010.

[45] A Simpson and JW Flower. An improved mathematical model for the aerodynamic forces on tandem cylinders in motion with aeroelastic applications. *Journal of Sound and Vibration*, 51(2):183–217, 1977.

[46] Christoffer Norberg. Fluctuating lift on a circular cylinder: review and new measurements. *Journal of Fluids and Structures*, 17(1):57–96, 2003.

[47] Gary K. Nave Jr., Mark Stremler, and Shane D. Ross. Wake stiffness and its application: oscillating cylinders and flying snakes. In *Proceedings of the 24th International Congress on Theoretical and Applied Mechanics (ICTAM)*, 2016.

Chapter 3

Global phase space structures in a model of passive descent

Abstract

Even the most simplified models of falling and gliding bodies exhibit rich nonlinear dynamical behavior. Taking a global view of the dynamics of one such model, we find an attracting invariant manifold that acts as the dominant organizing feature of trajectories in velocity space. This attracting manifold acts as a higher-dimensional analogue to the concept of terminal velocity, capturing the final slow phase of every passive descent. In this work, we present theoretical and numerical methods for approximating this manifold and discuss ways to approximate falling and gliding motion in terms of these underlying phase space structures.

Attribution

This chapter represents a collaborative work with Shane D. Ross, presently under review for publication in *Communication in Nonlinear Science and Numerical Simulation*. It is presented here just as it has been submitted to the journal.

3.1 Introduction

There are a wide variety of natural and engineered examples of systems which rely on aerodynamic forces for locomotion. Arboreal animals use gliding flight to catch prey or escape predators [1], while plant seeds may slowly follow the breeze to increase dispersion [2]. To compare different gliding animals with different morphologies, a variety of studies have resolved detailed motion of animals' glides from videos or other tracking methods [3, 4, 5, 6, 7]. Throughout their glide, animals may approach an equilibrium glide, but typically spend at least half of the glide between the initial ballistic descent, where aerodynamic forces are small, and the final equilibrium state when aerodynamic forces completely balance weight [5, 6, 7]. Falling seeds exhibit a variety of different falling motions as well, as fluid forces may drive rotation, fluttering, or tumbling as they descent [2]. These behaviors have provided inspiration for physical research and bio-inspired engineering design [8, 9, 10, 11]. To compare these behaviors and set the stage for future engineered models, it is useful to consider a mathematical model for this motion.

Both gliding animal flight and plant seed descent represent special cases of passive aerodynamic descent, which is a topic in fluid mechanics with very rich history dating back to at least the 19th century in the work of Maxwell and Zhukovskii [12, 13, 14]. Prior experimental works have identified several canonical behaviors exhibited by falling disks, plates, and plant seeds characterized by different couplings between rotation and translation in space [2, 15]. In all of these behaviors, an inherently high-dimensional system, which must consider velocities, angles, and angular velocities in 3D space, converges to a low-dimensional behavior, whether traveling in a single plane or going through a cycle of velocities [15, 16, 17, 18, 19, 20].

Mathematical models have offered many insights into passive descent. Ideal flow theory has been used to study the motion of a body both through a steady fluid and interacting with shed vortices [13, 21, 22, 23]. The Zhukovskii problem or phugoid model, which assumes that the wing travels with constant angle-of-attack, is a classic 2D ordinary differential equation for flight from which phugoid oscillations which couple forward velocity with pitch angle can be analyzed [14]. Andersen et al. developed a phenomenological model based on experiments and simulations which produce fluttering, tumbling, and even chaotic behavior through a 4D differential equation [17, 18]. To focus specifically on gliding animal flight and compare the gliding capabilities of different animals, Yeaton et al. [24] introduced a 2D model for non-equilibrium gliding of animals. It is a modification of this model which

we will consider in the present work. In this model, the authors decoupled translational and rotational dynamics in order to take a deeper view of the translational behavior and shape dependence based on lift and drag characteristics alone. To do so, inspired by the motion of gliding animals, the authors treat pitch angle as fixed with respect to the ground, assuming that the glider has some amount of control to hold this angle. Lift and drag are treated as functional parameters in this model, which is used to capture the differences in glider shapes. This model works especially well for gliding animals, but may be extended to general passive descent. The Zhukovskii problem [14] represents a special case of this model in which lift and drag are taken to be constant, while the Andersen et al. [18] model without rotation or added mass can be shown to be equivalent for a particular set of functions for lift and drag. Yeaton et al. [24] analyzed a variety of animal gliders and found that in most examples, trajectories in velocity space collapse onto a single curve as their velocities evolve slowly toward an equilibrium glide, as can be seen in Figure 3.2. In such examples, most of the dynamics of a passively descending body with constant pitch lie on or near an attracting normally hyperbolic invariant manifold in velocity space.

Attracting normally hyperbolic invariant manifolds, or simply attracting manifolds, such as the one found in Yeaton et al. [24], can play a very useful role in understanding the dynamics of a system [25]. As most of the dynamics occur near the manifold itself, the dimension of the system may be reduced by projecting the dynamics onto the attracting manifold [26]. In general, attracting manifolds also represent barriers to transport in the evolution of a system and therefore play a key role in understanding, for example, mixing in fluid systems [27, 28, 29]. The attracting manifold observed by Yeaton et al. [24] bears similarities to the idea of terminal velocity, acting as a barrier between trajectories which start with small velocity and those which begin with very large velocity. Therefore, we will refer to this curve as the *terminal velocity manifold*, or TVM. This comparison is made more clear in Section 3.2.1. The understanding of such a structure in this model will lead to a clear way to compare a variety of gliders with the same set of tools, it will allow for the dimension reduction of the system to understand the structure of these models, and and may lead to the possibility of controlling gliding flight with the intuition of the system's global structure.

The purpose of this paper is to investigate the glider model introduced by Yeaton et al. [24] more deeply by numerically identifying and analyzing the terminal velocity manifold. To analyze this manifold, we will use three example gliders, each one representing a potential application for this model. The first is the simplified mathematical model for a falling flat

plate [30]. The second is a biologically-inspired airfoil, based on water channel experiments on an object with the cross-sectional shape of a flying snake, *Chrysopelea paradisi* [31]. The third represents an engineering application, and uses wind-tunnel measurements on a NACA-0012 airfoil [32]. With these three examples, we will investigate the terminal velocity manifold, methods to find it, and how it changes with pitch angle, both as a bifurcation parameter and later as a time-varying parameter.

We begin the study by introducing the model from Yeaton et al. [24] which will be used in our analysis and describing the lift and drag functions for the flat plate, flying snake, and NACA-0012 airfoils in Section 3.2. In Section 3.3, we look at properties of the equilibrium points and bifurcations of the model. In Section 3.4, we discuss the terminal velocity manifold as it relates to stable and unstable manifolds of fixed points and numerical schemes to calculate it by bisection and the trajectory-normal repulsion factor. Once calculated, we vary the pitch parameter to look at changes in the terminal velocity manifold and simulate controlled changes in pitch in Section 3.5. From the work of this study, we gain new insights into gliding flight and the structure of slow-fast systems, discussed in Section 3.6.

3.2 A simple glider model

In their investigation of non-equilibrium gliding flight of animals, Yeaton et al. [24] introduce a general model for gliding flight which treats lift and drag as functions of angle-of-attack and pitch as a fixed parameter. This model provides a framework for comparing different gliding animals or objects through a non-dimensional scaling parameter, ϵ. As a dynamical system, the system presents an excellent model for investigation: it is naturally nonlinear, relies on intuitive assumptions which may be relaxed, and depends on functional input parameters.

To begin, consider a body moving in an unbounded, quiescent fluid medium under the force of gravity. The forces on the body consist solely of gravity and forces which arise from interactions with the surrounding fluid. The complexity of this problem, then, depends on the choice of model for the fluid forces. To fully capture the physics, a coupled infinite-dimensional fluid-structure model would be required.

For the purposes of presenting a low-dimensional model, however, we will consider only quasi-steady lift and drag, dependent solely on angle of attack, neglecting unsteady fluid forcing and Reynolds number dependence. As shown in the work of Andersen et al. [17, Sec.
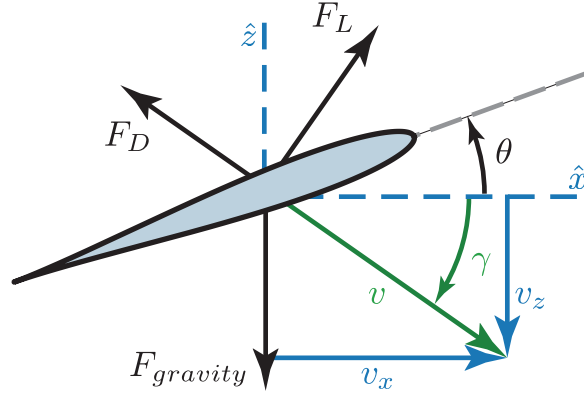
Figure 3.1: Definitions of angles and directions in the glider model used in this paper. The pitch angle θ represents the body's fixed orientation with respect to the ground. The black arrows show the lift force F_L, drag force F_D and gravitational force $F_{gravity}$ which give the model in (3.1). The magnitude v and direction γ of the body's velocity, shown in green, form the velocity-polar coordinates used in (3.3), while the $\hat{x}$ and $\hat{z}$ directions shown in blue comprise the inertial coordinates used in this study.

6] [18, Sec. 3.4], a quasi-steady assumption for lift and drag captures the dominant behavior in most situations of passive descent. The fluid forces, then, are given by $F_L = \frac{1}{2}\rho SV^2 C_L$ and $F_D = \frac{1}{2}\rho SV^2 C_D$, where ρ represents the density of the surrounding fluid, S represents the spanwise cross-sectional area of the body, V represents the magnitude of the body's velocity, and C_L and C_D represent the projection of the total fluid force onto coordinates perpendicular to (lift) and parallel to (drag) the direction of motion, respectively. The directions of these fluid forces are shown in Figure 3.1. For a glider consisting of an extruded 2-dimensional shape, $S = cs$ with c as the chord length of the body and s as the length of the span. As we are neglecting boundary effects and the fluid forces are the same anywhere in physical space, the position of the body represents two ignorable coordinates.

Under these assumptions, the equations of motion are given by the following equations, taking the parallel and perpendicular accelerations to be $a_\parallel = dV/dT$ and $a_\perp = V\,d\gamma/dT$, and the gravitational force as $F_{gravity} = mg$,

$$
\begin{aligned}
m\frac{dV}{dT} &= -\frac{1}{2}\rho csV^2 C_D + mg\sin\gamma, \\
mV\frac{d\gamma}{dT} &= -\frac{1}{2}\rho csV^2 C_L + mg\cos\gamma,
\end{aligned}
\tag{3.1}
$$

where m is the mass of the glider, g represents gravitational acceleration, and γ is the clockwise direction of velocity with respect to the horizontal as shown in Figure 3.1.

As in [24], we introduce nondimensional time t and velocity v, choosing $\frac{d}{dT} = \sqrt{g/c\epsilon}\frac{d}{dt}$ and $V = \sqrt{gc/\epsilon}v$ to rescale (3.1). This rescaling features a nondimensional factor, $\epsilon = \frac{\rho c S}{2m}$, which is the universal glide scaling parameter. It can be used to compare various gliders against one another [24]. The dimensionless equations of motion become,

$$\dot{v} = -C_D v^2 + \sin\gamma,$$
$$v\dot{\gamma} = -C_L v^2 + \cos\gamma, \tag{3.2}$$

where the dot represents differentiation with respect to the non-dimensional time, $(\dot{}) = d/dt$.

We consider these fluid force coefficients as functions of angle of attack only. As shown schematically in Figure 3.1, the angle of attack is given by the sum of the constant pitch angle θ, the counter-clockwise angle of the body with respect to the ground, and the glide angle γ, the clockwise angle of the body's velocity with respect to the ground. We will discuss these functions in more detail in Section 3.2.2

$$\dot{v} = -C_D(\gamma + \theta)v^2 + \sin\gamma,$$
$$\dot{\gamma} = -C_L(\gamma + \theta)v + \frac{1}{v}\cos\gamma. \tag{3.3}$$

Alternatively, we can express this system in an inertial reference frame aligned with an observer on the ground, where $v_x = v\cos\gamma$ is the horizontal velocity and $v_z = -v\sin\gamma$ is the vertical velocity. In terms of these inertial coordinates, the total velocity is given by $v = \sqrt{v_x^2 + v_z^2}$ and the glide angle is $\gamma = -\arctan v_z/v_x$. Allowing the functional dependence of lift and drag to again be implicit, the equations are given by,

$$\dot{v}_x = v^2\left(C_L\left(\gamma + \theta\right)\sin\gamma - C_D\left(\gamma + \theta\right)\cos\gamma\right),$$
$$\dot{v}_z = v^2\left(C_L\left(\gamma + \theta\right)\cos\gamma + C_D\left(\gamma + \theta\right)\sin\gamma\right) - 1. \tag{3.4}$$

These equations of motion end up being the most convenient to use, where we observe the system in inertial coordinates, but calculate the right hand side in terms of the velocity-polar coordinates.

In terms of these inertial coordinates, this system can also be expressed as,

$$\dot{v}_x = \sqrt{v_x^2 + v_z^2}\left(-C_L\left(v_x, v_z, \theta\right)v_z - C_D\left(v_x, v_z, \theta\right)v_x\right),$$
$$\dot{v}_z = \sqrt{v_x^2 + v_z^2}\left(C_L\left(v_x, v_z, \theta\right)v_x - C_D\left(v_x, v_z, \theta\right)v_z\right) - 1. \tag{3.5}$$
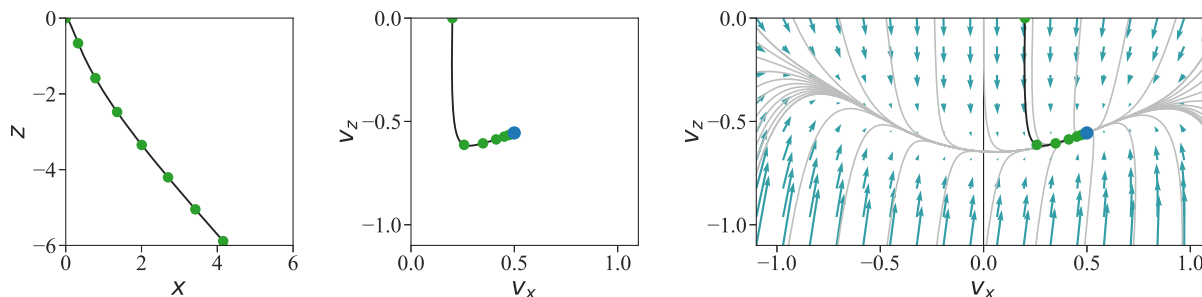
Figure 3.2: Example glide in position space (left) in which the glider launches with an initial velocity of $(v_x(0), v_z(0)) = (0.2, 0)$ and the associated velocities of that glide (center). The green points represent even the states at every 1.5 non-dimensional time units. Between the first two green points, the glider accelerates downward due to gravity. After that, the velocities change more slowly toward the equilibrium velocity shown in blue. Looking at the whole velocity space (right), trajectories shown in gray from a variety of initial conditions seem to collapse to a single curve in the velocity space. This attracting curve is the *terminal velocity manifold*. Additionally, the blue vector field shows the magnitude and direction of acceleration at every velocity, while the black vertical line represents $v_x = 0$.

3.2.1   The terminal velocity manifold

Terminal velocity is a common notion in popular explanations of fluid forces, defined as the value of velocity which balances wind resistance and gravity such that a falling body can no longer accelerate. We can express this concept mathematically with a one-dimensional model of vertical descent, using the same rescalings that we consider above in (3.2).

$$\dot{v}_z = C_D v_z^2 - 1 \tag{3.6}$$

From this one degree-of-freedom model, terminal velocity is the point where wind resistance (drag) balances gravity, which is the fixed point (3.6), $v_T = \sqrt{1/C_D}$ in our rescaled coordinates. The terminal velocity point is a 0-dimensional object, serving as a codimension 1 structure in the 1-dimensional model. It acts as a barrier to transport, because all trajectories of velocity approach the fixed point without crossing it. A small initial magnitude of velocity can never become larger than terminal velocity, while a large initial magnitude of velocity can never become smaller than terminal velocity. It divides the 1-dimensional phase space into two qualitatively distinct regions; those approaching the terminal velocity from below and those approaching it from above.

As discussed in the introduction, the *terminal velocity manifold*, or TVM, divides phase space into two regions without allowing trajectories to cross it on their way to an ultimate fixed point. The attracting 1-dimensional structure in the 2-dimensional model, shown in Figure 3.2, acts as a higher-dimensional analogue of terminal velocity. All trajectories rapidly converge onto the manifold and slowly evolve along it regardless of initial condition, just as all trajectories converge to the point of terminal velocity in the 1-dimensional model (3.6). The difference in time scales onto and along the manifold can be seen by the even snapshots in time represented by green dots in Figure 3.2.

3.2.2   Lift and drag as functional parameters

The behavior of this model depends entirely on the choice for lift and drag functions. For any object without an axisymmetric cross-sectional shape, the fluid forces will depend on the angle-of-attack of the object. As discussed before and shown in Figure 3.1, this angle of attack in our model is the sum of the pitch angle θ and the glide angle γ: $\alpha = \theta + \gamma$. We assume that the fluid force coefficients are independent of increasing Reynolds number.

The lift coefficient is a function which maps from angle of attack, a cyclic variable on $\mathbb{S}^1$, to a finite subset of $\mathbb{R}$, as an unbounded lift coefficient would lead to unbounded acceleration.

$$C_L : \mathbb{S}^1 \mapsto \mathcal{I}_L \subset \mathbb{R}. \tag{3.7}$$

The value may be positive or negative.

The range of the drag function, $\mathcal{I}_D$, on the other hand, must be positive. In a quiescent fluid, a passively falling body cannot produce thrust on its own, and, although small, there must be some small amount of viscous drag on the body,

$$C_D : \mathbb{S}^1 \mapsto \mathcal{I}_D \subset \mathbb{R}^+. \tag{3.8}$$

The details of each function depend on the body's shape. Below, we consider three example systems: a mathematical model for a falling flat plate, an airfoil based on the flying snake *Chrysopelea paradisi*, and experimental measurements of a NACA-0012 airfoil.

Falling flat plate

The motion of a falling flat plate has been researched extensively in the context of insect flight, falling leaves, and falling paper [16, 17, 18, 19, 30]. It provides a simple shape which can exhibit a wide range of behaviors from varying only a few parameters. For a holistic look at this problem, a pair of papers by Andersen, Pasavento, and Wang [17, 18] investigated this problem experimentally and computationally to develop a phenomenological model. In their investigation, the authors use the results of a previous paper [30] which considered the quasi-steady lift and drag on a flat plate for a range of angles-of-attack and found that lift and drag coefficients can be approximated simply by,

$$C_D(\alpha) = 1.4 - \cos(2\alpha),$$
$$C_L(\alpha) = 1.2\sin(2\alpha). \tag{3.9}$$

These functions are illustrated in Figure 3.3b. This model is based on the results of direct numerical simulation for a thin elliptical plate at $Re = 100$ [30], but represent a simple, analytical expression for lift and drag to develop our methods. Drag is at a minimum where the flat plate is horizontal to the incoming air and at a maximum at $\alpha = 90°$, while lift vanishes at $0°$ and $90°$, while reaching a maximum at $45°$. Using this model for lift and drag in the equations of motion found in (3.4), we can analyze the velocity space for a single flat plate falling through a fluid due to gravity, shown in Figure 3.3c for $\theta = -5°$.

The flying snake airfoil: the body shape of *Chrysopelea paradisi*

As a biologically based example, we consider the cross-sectional body shape for *Chrysopelea paradisi*, pictured in Figure 3.3d [33]. During the glide, the snake expands its ribs to form an airfoil-like shape that is horizontally symmetric. Holden et al. [31] determined the aerodynamic characteristics of this shape by 3-D printing the extruded cross-section and measuring its lift and drag in a water channel. Measurements were conducted over angles of attack from $-10°$ to $60°$. A variety of methods have been applied to understand and model this animal's behavior [1, 6, 24, 34, 35, 36, 37]. Here, we analyze how a fixed glider with the snake's characteristics would behave, similar to the work of Jafari et al. [35]. This simplified analysis will give insight into the more complex behavior of the snake itself. Its lift and drag characteristics are shown in Figure 3.3e, and the resulting phase space is shown in Figure 3.3f for $\theta = -5°$.
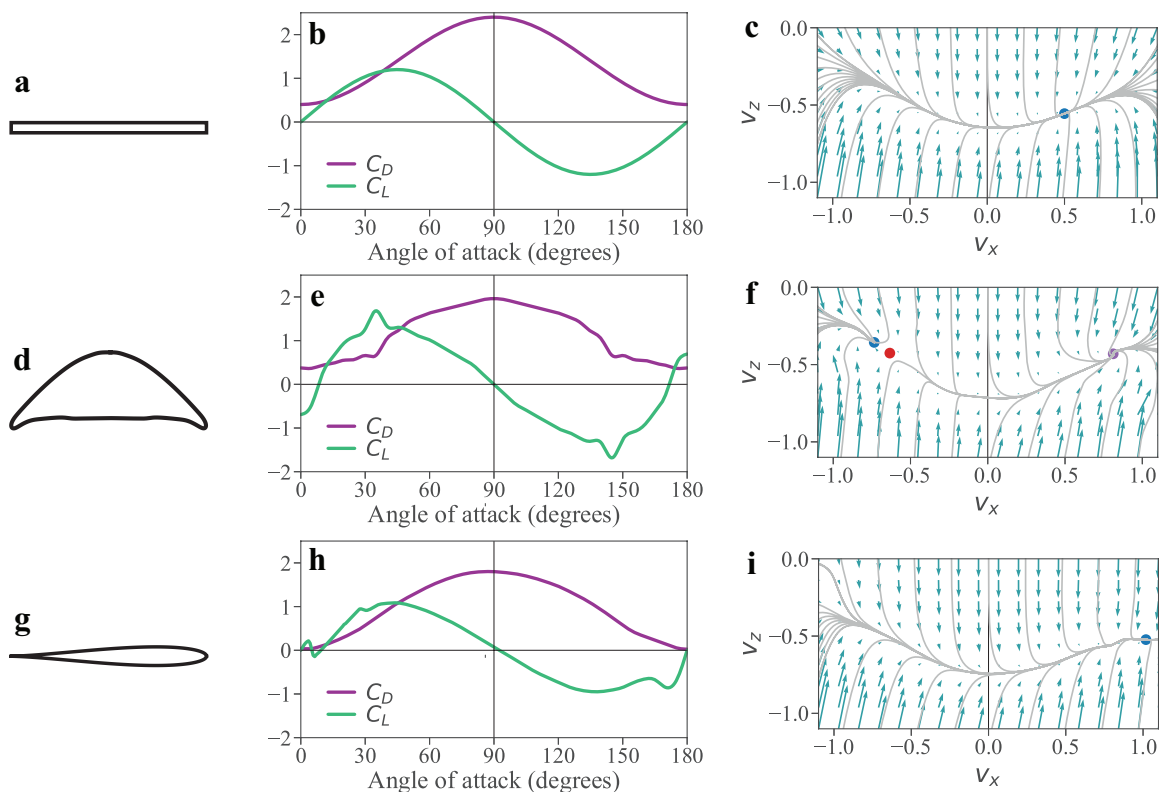
Figure 3.3: Comparison of the example airfoils considered in this paper. For each airfoil, the lift and drag curves are shown over the interval $\alpha \in (0°, 180°)$. The symmetry of drag and antisymmetry of lift for the flat plate (panel b) and flying snake airfoils (panel e) about $\alpha = 90°$ are evident. The NACA airfoil exhibits this same symmetry and anti-symmetry, but about $\alpha = 0°$ in panel h. In panels c, f, and i, the acceleration at each velocity is shown by the blue arrows and example trajectories are shown in gray for an example with a fixed pitch angle of $\theta = -5°$.

The NACA-0012 airfoil

As a representative of engineered gliding systems, we consider the example of a NACA-0012 airfoil. It is a vertically symmetric airfoil used in a variety of aircraft with a maximum thickness of 12% of its chord length, as shown in Figure 3.3g. Its lift and drag characteristics, shown in Figure 3.3h, were measured in a wind tunnel for angles of attack ranging from 0° to 180° for application to vertical axis wind turbines [32]. Lift increases near $\alpha = 0°$ before it drops off at the point of stall, then, lift continues to increase until approximately $\alpha = 45°$. The resulting phase space is shown in Figure 3.3i for $\theta = -5°$.

3.2.3   Shape symmetry and force coefficients

There are a number of symmetries present in the examples that we have chosen to study here. Both the snake airfoil and flat plate exhibit left-right symmetry, the NACA-0012 airfoil and flat plate exhibit top-bottom symmetry, and the flat plate also shows 180° rotational symmetry. Each of these symmetries has natural consequences for the functional symmetries of the fluid force coefficients.

The symmetry of rotation by 180°, as observed in the flat plate example, means that the shape at angle-of-attack α is the same as the shape at $\alpha + 180°$ for all angles of attack. Therefore,

$$
\begin{aligned}
C_L(\alpha) &= C_L(\alpha + 180°), \\
C_D(\alpha) &= C_D(\alpha + 180°).
\end{aligned}
\tag{3.10}
$$

These coefficients are therefore cyclic with period 180° rather than 360° for all other shapes. This fact causes the above model for the flat plate to depend on sinusoidal functions of 2α.

The top-bottom symmetry of the NACA-0012 airfoil and flat plate means that drag is the same whether the airfoil is pitched up or down, and that lift is exactly opposite for upward or downward pitch. These properties correspond to the properties of even and odd functions, respectively. Therefore,

$$
\begin{aligned}
C_L(\alpha) &= -C_L(-\alpha), \\
C_D(\alpha) &= C_D(-\alpha).
\end{aligned}
\tag{3.11}
$$

As a corollary, we find that $C_L(0) = 0$ for systems with this symmetry. This result follows naturally from $C_L(\alpha) = -C_L(-\alpha)$ when $\alpha = 0$.

Finally, the left-right symmetry of the snake and the flat plate is equivalent to the top-bottom symmetry, but rotated by 90°.

$$
\begin{aligned}
C_L\left(90° + \alpha\right) &= -C_L\left(90° - \alpha\right), \\
C_D\left(90° + \alpha\right) &= C_D\left(90° - \alpha\right).
\end{aligned}
\tag{3.12}
$$

Following the same logic as above, it's clear that $C_L(90°) = 0$ for systems with left-right symmetry.

3.3 Equilibrium points of the system

We begin our analysis of the phase space structure of the glider model by looking at the possible equilibrium glide points of the system. A criterion for these equilibrium points may be found in the expression for horizontal acceleration $\dot{v}_x$ of the glider from (3.4). Each fixed point must correspond with zero acceleration, and therefore, $v^2 \left(C_L \sin \gamma - C_D \cos \gamma \right) = 0$. This expression is only zero when $v = 0$ or $C_L \sin \gamma - C_D \cos \gamma = 0$. When $v = 0$, the vertical acceleration is given by gravity, $\dot{v}_z = -1$, so this point does not correspond to a fixed point. Therefore, any equilibrium points require the following condition on glide angle γ^*,

$$\cot \gamma^* = \frac{C_L}{C_D} \left(\gamma^* + \theta \right). \tag{3.13}$$

The condition for the magnitude of velocity at the fixed point is found by setting $\dot{v}_z = 0$ in (3.4), which gives the v_z-nullcline, which will be discussed in more detail in Section 3.4.2.

There will always exist one fixed point on the interval $\gamma \in (0, \pi)$, the lower half plane of velocity space. To show this, we must make two physical inferences, one regarding lift and one regarding drag, which we have already introduced in Section 3.2.2. Since the lift coefficient is a mathematical model of a real fluid force, an infinite lift coefficient would be physically unreasonable, and therefore this function maps to the finite interval $\mathcal{I}_L \subset \mathbb{R}$ as in (3.7). Secondly, as discussed above, in a quiescent field of fluid with a quasi-steady fluid force, it is impossible for a single body to generate negative drag, or thrust. Furthermore, there must be at least some viscous drag on a body moving through a fluid. Therefore, although it may be small, the range of the drag coefficient, $\mathcal{I}_D$, must be a subset positive of the positive reals, as in (3.8). Thus, it is physically reasonable to assume that the lift coefficient function is finite, and the drag coefficient function is everywhere positive.

Theorem 3.1. *For a 2-dimensional glider model as conceptualized in (3.4) with a smooth function with positive image for drag coefficient and a smooth function with finite range for lift coefficient, there must be at least one fixed point on the open domain $D = \{\gamma | \gamma \in (0, \pi)\}$.*

Proof. Consider the condition for equilibrium points given above in (3.13). This condition can be arranged to create a function $h : D \mapsto \mathbb{R}$.

$$h(\gamma) = \cot \gamma - \frac{C_L}{C_D} \left(\gamma + \theta \right) \tag{3.14}$$
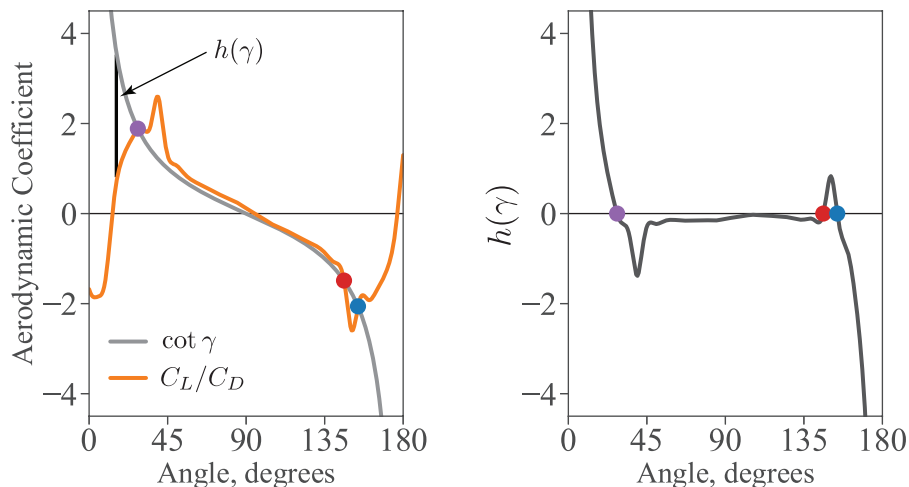
Figure 3.4: Graphical representation of (3.14). Every intersection between the two functions, or equivalently, every zero crossing of $h(\gamma)$, represents a fixed point of the system. This example is for the flying snake airfoil at pitch angle $\theta = -5°$, matching the phase space shown in Figure 3.3f.

Any value of γ such that $h(\gamma) = 0$ corresponds to a fixed point γ^* satisfying (3.13).

From our assumptions about the lift and drag coefficient, that lift is finite and drag is positive and therefore nonzero, we may infer that the lift to drag ratio $\frac{C_L}{C_D}(\gamma + \theta)$ is itself finite. Thus, our function $h(\gamma)$ is dominated by the contribution of $\cot\gamma$ at both endpoints of the domain.

$$\lim_{\gamma\to0^+} h(\gamma) = \lim_{\gamma\to0^+} \cot\gamma \quad \to \quad \infty$$
$$\lim_{\gamma\to\pi^-} h(\gamma) = \lim_{\gamma\to\pi^-} \cot\gamma \quad \to \quad -\infty$$

(3.15)

Since $h(\gamma) \to \infty$ as $\gamma \to 0$ and $h(\gamma) \to -\infty$ as $\gamma \to \pi$, by the Intermediate Value Theorem (IVT), there must be a point in between such that $h(\gamma) = 0$. Therefore, there must be at least one fixed point on the interval D. □

By this theorem, there must be some downward ($v_z < 0$) equilibrium point for any lift and drag functions obeying the quite general criteria of (3.7) and (3.8). This function that we have defined, $h(\gamma)$, has the important property of being topologically conjugate to the acceleration along the terminal velocity manifold. Furthermore, we can show that there must be an odd number of fixed points on the interval D outside of edge cases where the function grazes the 0-line, that is, $h = 0$ and $dh/d\gamma = 0$.

Theorem 3.2. *Outside of those cases where $h(\gamma^*) = 0$ and $dh/d\gamma|_{\gamma=\gamma^*} = 0$, it is guaranteed that there are an odd number of equilibrium points on the domain $D = \{\gamma | \gamma \in (0, \pi)\}$.*

Proof. Assume that there at least two equilibrium points $\gamma_1^*, \gamma_2^* \in (0, \pi)$ with $\gamma_1^* < \gamma_2^*$ and that $dh/d\gamma|_{\gamma=\gamma_1^*} < 0$.

If $dh/d\gamma|_{\gamma=\gamma_2^*} > 0$, then $h(\gamma_2^* + \epsilon) > 0$ for a small $\epsilon > 0$. Since, from the previous proof, $h(\pi) \to -\infty$, there must be a third fixed point γ_3^* on the interval (γ_2^*, π) by the IVT. Conversely, if $dh/d\gamma|_{\gamma=\gamma_2^*} < 0$, then $h(\gamma_2^* - \epsilon) > 0$ for a small $\epsilon > 0$. Under our assumption, $dh/d\gamma|_{\gamma=\gamma_1^*} < 0$ which implies $h(\gamma_1^* + \epsilon) < 0$. In this case, there must be a third fixed point γ_3^* on the interval (γ_1^*, γ_2^*) by the IVT.

This same logic applies if we assume $dh/d\gamma|_{\gamma=\gamma_2^*} < 0$ and consider both cases of $dh/d\gamma|_{\gamma=\gamma_1^*}$. Therefore, if there are at least two equilibrium points with nonzero derivatives of $h(\gamma)$, there must be a third. By the same argument, four equilibrium points implies a fifth and so on. $\square$

Furthermore, if a bifurcation occurs which transitions from one fixed point to three, the two new equilibrium points must have opposite derivatives. That is, $dh/d\gamma|_{\gamma=\gamma^*} > 0$ for one fixed point and $dh/d\gamma|_{\gamma=\gamma^*} < 0$ for the other. If we investigate this expression, we find that,

$$\left.\frac{dh}{d\gamma}\right|_{\gamma=\gamma^*} = -\csc^2\gamma^* - \left(\frac{C_L}{C_D}\right)'(\gamma^* + \theta), \tag{3.16}$$

where $(\cdot)'$ denotes the derivative of a function with respect to its argument.

In [24], the authors use the Jacobian of the equations of motion to express the conditions for different types of equilibrium points. These conditions are expressed in terms of two variables, $\tau = C_L'/C_D + 3$ and $\Delta = 1 + (C_L/C_D)^2 + (C_L/C_D)'$. Using trigonometric identities and (3.13), (3.16) can be rearranged to give,

$$\left.\frac{dh}{d\gamma}\right|_{\gamma=\gamma^*} = -1 - \left(\frac{C_L}{C_D}\right)^2(\gamma^* + \theta) - \left(\frac{C_L}{C_D}\right)'(\gamma^* + \theta) = -\Delta. \tag{3.17}$$

If $\Delta < 0$, the fixed point must be of saddle type. Therefore, if there exist more than one fixed point, γ_i^* on the interval $\gamma \in (0, \pi)$ ordered such that $\gamma_1^* < \gamma_2^* < ...$, then every even fixed point must be of saddle type. This can be seen below in Figure 3.5. Along every vertical slice, there are an odd number of fixed points, and anytime there are more than one, the even fixed points are saddle points, denoted by the red points.
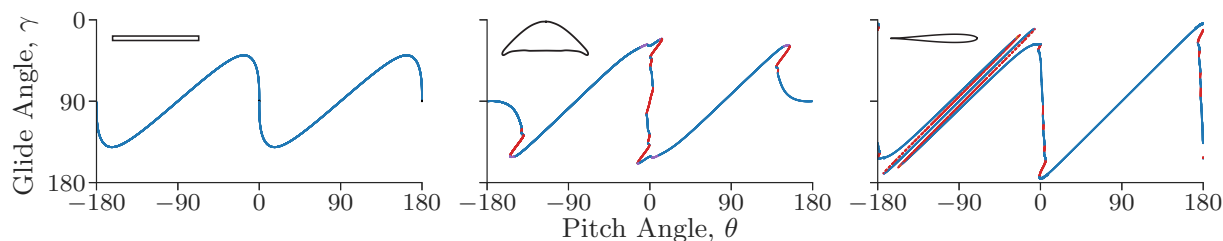
Figure 3.5: The bifurcation diagram showing the glide angle of the equilibrium points γ^* at each pitch angle θ for the flat plate(left), the flying snake cross section(center), and a NACA-0012 airfoil(right). The γ-axis is flipped such that forward equilibrium glides ($v_x > 0$, $\gamma^* < 90°$) are located at the top while backward equilibrium glides ($v_x < 0$, $\gamma^* > 90°$) are located in the lower half of each panel. The type of fixed point is indicated by the color. Blue indicates a saddle node, purple indicates a stable focus, red indicates a saddle point, and black indicates a center fixed point.

From the criterion given by (3.13), we show the numerically computed bifurcation diagrams for the three examples considered in this work below in Figure 3.5. These bifurcation diagrams are numerically found by pseudo-arclength continuation, and show the critical glide angle for each fixed point, γ^*, as a function of the pitch angle parameter θ. The colors indicate the equilibrium type, with blue points signifying stable nodes, purple points signifying stable foci, and red points signifying saddle points.

Note that this proof only deals with the appearance and number of fixed points, and does not preclude the possibility of Hopf bifurcations, which are possible within this model [24, Supplement]. The appearance and character of such bifurcations is left to future work.

3.4 Detecting the terminal velocity manifold

With a better understanding about the behavior of changes in fixed points, we turn our attention to the terminal velocity manifold. From the phase space of the system shown in the right panels of Figure 3.3 (c, f, and i), we can observe several properties of the TVM. As mentioned in the introduction, the TVM is an example of an attracting normally hyperbolic invariant manifold [25], meaning that at every point on the manifold, the eigenvalue of the linearized system normal to the manifold has a negative real part. Based on the properties of this structure, we employ a variety of methods to identify it.
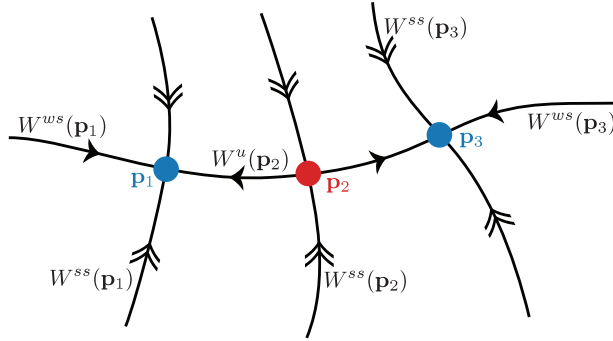
Figure 3.6: A schematic representation of the attracting manifold in the context of stable and unstable manifolds of fixed points.

As all fixed points of the system lie along the TVM, we will investigate this structure as it relates to the stable and unstable manifolds of fixed points [38]. Additionally, as shown schematically in Figure 3.6, motion along the manifold is slower than motion onto the manifold, giving it the behavior of a slow manifold [39], so we will approximate it using the v_z-nullcline, which serves as a proxy to a critical manifold. As discussed in section 3.2.1, the TVM acts as a barrier to transport in the velocity space, so we may employ a bisection method to find this structure. Finally, as the TVM is a globally attracting structure, we employ a method based on the attracting behavior of trajectories called the trajectory-normal repulsion factor [28].

3.4.1   Stable manifold expansion

As we have shown in Section 3.3, there must always be at least one equilibrium point on the interval $(0, \pi)$ and always an odd number of equilibrium points. The difference in time scales of motion onto and along the TVM is related to the magnitude of the eigenvectors of the Jacobian at the equilibrium points. The global terminal velocity manifold, then, is associated to the stable and unstable manifolds of the fixed points [40]. Figure 3.6 shows a schematic of the stable and unstable manifolds for an example system with two stable nodes and one saddle point.

For stable nodes, such as p_1 and p_3 in the figure, the stable manifold W^s is two dimensional. However, the stable manifold contains two one-dimensional embedded submanifolds, which are the strong stable $W^{ss} \subset W^s$ and weak stable $W^{ws} \subset W^s$ submanifolds of each point. These are the nonlinear expansions of the strong stable E^{ss} and weak stable E^{ws} eigenvectors

of the fixed point. The associated eigenvalues must have the ordering $\lambda^{ss} < \lambda^{ws} < 0$. For the saddle points, such as $\mathbf{p}_2$, there remains an ordering of the magnitudes of the eigenvalues $0 < \lambda^u < -\lambda^{ss}$. However, in this case, the strong stable submanifold represents the entirety of the stable manifold $W^{ss} = W^s$. From Section 3.3, the even fixed points are saddle points. The terminal velocity manifold is, in general, the union of the stable manifolds of all stable equilibrium points in the system.

The most logical method for extracting the TVM, then, is the semi-analytical method of integrating the weak stable eigendirection E^{ws} of each stable fixed point backward in time [38, 41]. However, because of the dominance of the strong stable eigenvalue $\lambda^{ss} < \lambda^{ws}$, in backward time the strong stable direction becomes a strong unstable direction. Any deviation from the weak stable submanifold W^{ws} in backward time will lead to the trajectory effectively peeling off of the weak stable submanifold. Integrating the unstable manifold of saddle fixed points W^u in forward time is able to identify the TVM between any stable fixed points. However, to take a global approach to the TVM, a method other than manifold expansion is required.

In the prior study by Yeaton et al. [24], the authors present the polynomial expansion of the unstable manifold in the neighborhood of equilibrium points in this system and the acceleration along it. This local approach is very successful at capturing the terminal velocity manifold near a fixed point. However, it is not able to accurately predict the TVM further from the fixed point, where higher order terms may no longer be neglected. Therefore, it is necessary to find a global approach for calculating the TVM if we are to analyze how the terminal velocity manifold changes with changes in both our functional lift and drag parameters and pitch parameter.

3.4.2   The v_z-nullcline

The TVM shows a separation in time scales of motion, as schematically shown in Figure 3.6, giving it the structure of an attracting slow manifold. Therefore, the methods used in this section to identify the TVM may be naturally extended to other slow-fast systems. However, the system given by (3.4) has no explicit slow parameter as in classical examples with slow-fast [39, 42, 43]. The search for an implicit slow parameter is left to possible future work. As a first step to identifying the terminal velocity manifold with a global approach, we follow Yeaton et al. [24] and present the v_z-nullcline as an approximation. Although there is no
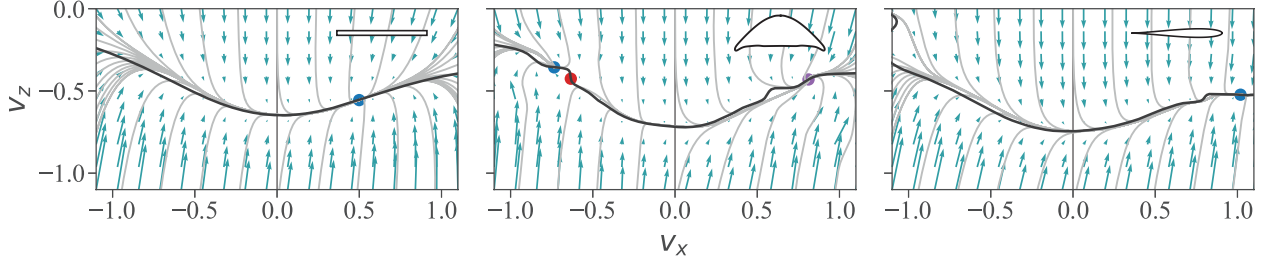
Figure 3.7: The v_z-nullcline as an approximation to the terminal velocity manifold for the flat plate=(left), the flying snake cross section(center), and a NACA-0012 airfoil(right) at pitch angle of $\theta = -5°$. The nullcline remains close to the most attracting curve, but does not lie along it.

explicit slow parameter in this system, this resembles the calculation of the critical manifold in a slow-fast system [39]. Similar to a critical manifold, the v_z-nullcline remains near the attracting manifold observed from trajectories, but the two do not necessarily coincide.

The v_z-nullcline may be found by setting $\dot{v}_z = 0$. The locus of points can be calculated directly from the second part of (3.4).

$$\dot{v}_z = v^2(C_L \cos \gamma + C_D \sin \gamma) - 1 = 0$$

Rearranging this equation gives a straightforward expression written in terms of the tangential-normal coordinates for convenience,

$$v = (C_L \cos \gamma + C_D \sin \gamma)^{-\frac{1}{2}} \tag{3.18}$$

This can be written parametrically from the definition of v_x and v_z as

$$\begin{aligned} v_x &= \quad (C_L \cos \gamma + C_D \sin \gamma)^{-\frac{1}{2}} \cos \gamma \\ v_z &= -(C_L \cos \gamma + C_D \sin \gamma)^{-\frac{1}{2}} \sin \gamma \end{aligned} \tag{3.19}$$

We consider the v_z-nullcline to be given as the range of glide angles γ which satisfy (3.18) between singular values. The singular values occur where the denominator of (3.18) goes to zero, given by

$$\gamma_s = \arctan\left(-\frac{C_L}{C_D}\right). \tag{3.20}$$

The v_z-nullclines compared against the trajectories for all three of our example gliders are shown in Figure 3.7. As previously discussed, the TVM is the curve onto which all trajectories collapse. However, in Figure 3.7, it is clear that many trajectories pass through the v_z-nullcline. Therefore, although the TVM and v_z-nullcline are close to one another, they are not the same curve. As the terminal velocity itself is an invariant manifold on which motion is slow and all acceleration is tangential and not generally perpendicular to the v_z direction, then the TVM is not generally the v_z-nullcline. That is, along the TVM vertical acceleration is nonzero in general, even though it is small $|\dot{v}_z| \ll 1$. The v_z-nullcline approximates the terminal velocity manifold, but is inexact.

3.4.3 Bisection method

Based on the observation that the TVM acts as a barrier to transport and its repelling nature in backward time, we introduce a bisection method to numerically identify the TVM. Bisection methods are typically used for identifying a zero-crossing of a function over a fixed interval. They are conceptually straightforward algorithms that have been extended for application to a variety of problems in dynamical systems to determine the boundaries between basins of stability [44, 45].

For a one dimensional function, one can find the zero-crossing of a function by beginning with endpoints on either side of the zero-crossing and evaluating the sign of the function at the midpoint of the two endpoints. If the function at the midpoint is negative, then the midpoint replaces the lower endpoint. If positive, the midpoint replaces the upper endpoint. The midpoint of the new endpoints is calculated and the process is repeated until the endpoints are within some tolerance of one another.

The implementation of a bisection method in our context is based on the origin of trajectories rather than the value of a function. Selecting a point in phase space and integrating backward in time, we check to see whether the trajectory heads toward positive values of vertical velocity or negative values of vertical velocity, which indicates whether the trajectory which crosses our test point began above or below the TVM. We select test points along a vertical slice of velocity space with a fixed initial horizontal velocity and do a bisection search for the v_z-value. The schematic of our bisection method based on this classification is shown in Figure 3.8. An initial Max and Min are selected above and below the true TVM (black), which is confirmed by their backward integration. Then the midpoint, Mid, is selected and,
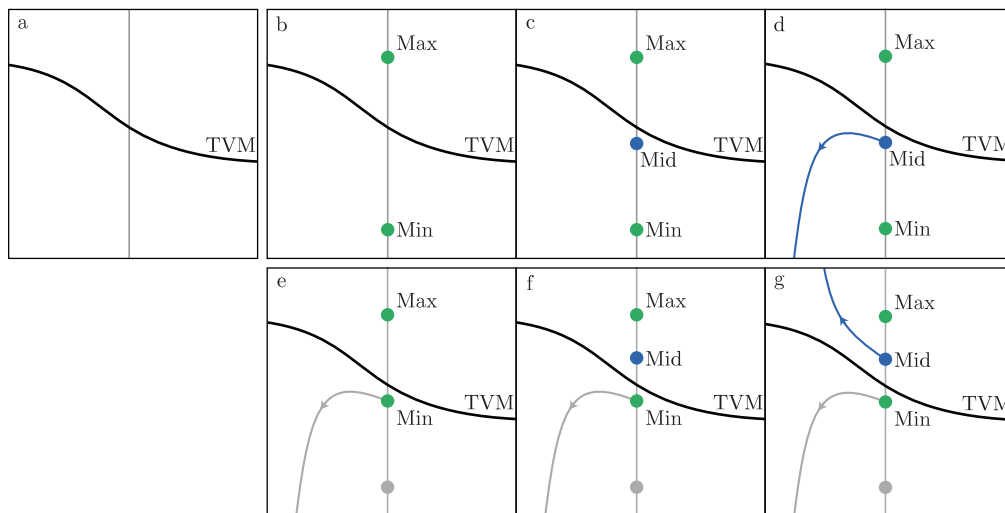
Figure 3.8: Schematic representation of a bisection algorithm to find the true TVM, shown in black, along a vertical slice of velocity space shown in gray (a). We select two points that bracket the manifold, labeled Max and Min and shown in green (b). Next, we calculate the midpoint of Max and Min, labeled Mid and shown in blue (c). We integrate Mid backward in time (d) and find that the trajectory moves downward. Therefore, Mid is selected as the new Min (e), a new Mid is selected (f) and integrated backward (g). This process is then repeated iteratively until the distance between Max and Min is smaller than a specified tolerance.

by integration, confirmed to be below the TVM. This point replaces Min and a new Mid is selected.

Figure 3.9 shows the results of our implementation of the bisection algorithm. A point along the terminal velocity manifold was found outside of the boundary of the figure through bisection and integrated forward in time. For the flying snake example in the center panel, the saddle fixed point was also calculated, and its unstable manifold integrated in forward time. Using the bisection method from the outside in conjunction with unstable manifold expansion from within the manifold provides a piecewise global approach to find the manifold. It is also possible, although more computationally expensive, to conduct a bisection search at a variety of points v_x across the entire domain to find the corresponding point v_z that lies along the manifold. These two approaches to the bisection algorithm give identical results.

We find that this method is very successful in identifying the TVM. Visual inspection of Figure 3.9 shows that all trajectories go to the calculated TVM in black. The success of this method confirms the observation that the TVM serves as the boundary between trajectories
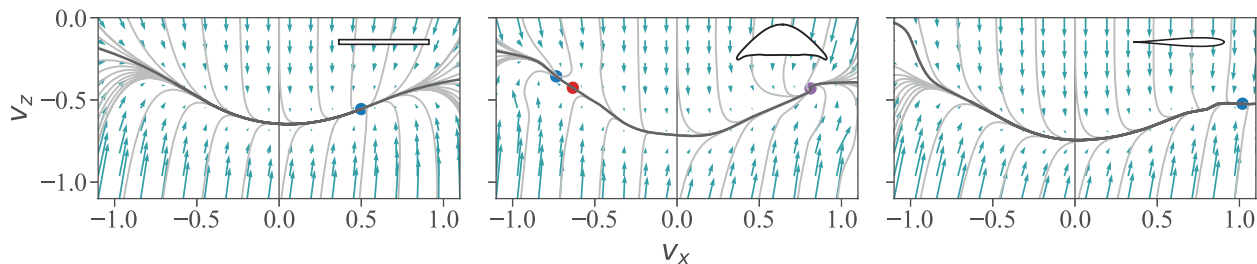
Figure 3.9: The velocity space at a pitch angle of $\theta = -5°$ for the flat plate (left), the flying snake cross section (center), and a NACA-0012 airfoil(right). The bisection method described in Figure 3.8 is able to accurately find the TVM (black), which attracts all trajectories (gray) of the vector field (blue).

with large negative initial vertical velocities and trajectories with zero or positive initial vertical velocities.

3.4.4   Normal repulsion factor

Another method, the *normal repulsion factor*, provides additional physical insight for the whole system [28]. This quantity gives a measure of how much an invariant manifold normally repels nearby trajectories over a finite time, T. In an autonomous system, every trajectory is an invariant manifold, so the repulsion factor gives a scalar value at every point x_0 that indicates how much nearby trajectories are normally repelled. As illustrated in Figure 3.10, this value is given by the forward mapping of trajectory-normal vectors,

$$\rho_T = \langle \mathbf{n}_T, \nabla F_T \mathbf{n}_0 \rangle, \tag{3.21}$$

where F_T and ∇F_T represent the flow map of the system over the interval $(0, T)$ and its gradient, $\mathbf{n}_0$ is unit the normal vector at time 0, and $\mathbf{n}_T$ is the unit normal vector at time T. The normal vectors are calculated by 90° counterclockwise rotation,

$$R = \begin{pmatrix} 0 & -1 \\ 1 & 0 \end{pmatrix}, \tag{3.22}$$

of the tangent vector given by the acceleration $\dot{\mathbf{v}}$ in our problem, normalized by the magnitude of that acceleration $|\dot{\mathbf{v}}|$: $\mathbf{n} = R\dot{\mathbf{v}}/|\dot{\mathbf{v}}|$.

In a Lagrangian method such as this one, globally attracting features in the system are found
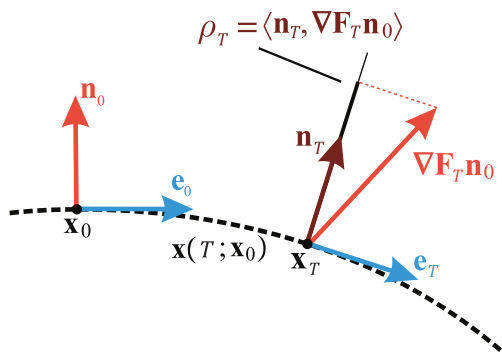
Figure 3.10: Graphical explanation of the trajectory-normal repulsion factor. The initial unit normal vector $\mathbf{n}_0$ is mapped forward by the gradient of the flow map $\nabla \mathbf{F}_T \mathbf{n}_0$. By taking an inner product with the new unit normal vector $\mathbf{n}_T$, we measure the stretching of phase space normal to the trajectory of $\mathbf{x}_0$ over the time T.
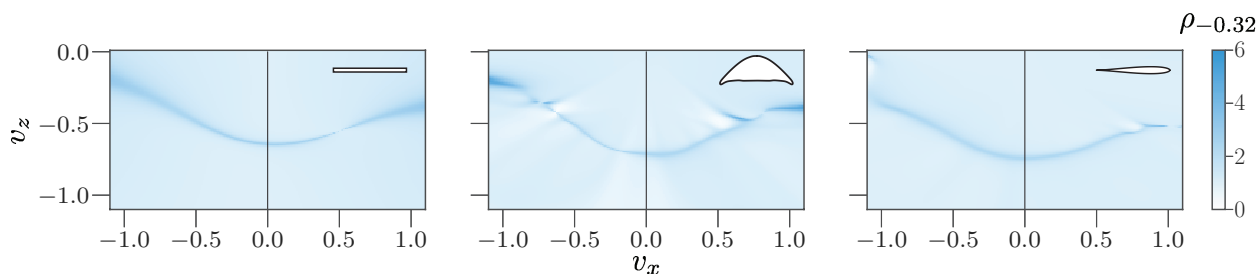
Figure 3.11: The velocity space at a pitch angle of $\theta = -5°$ for the flat plate(left), the flying snake cross section(center), and a NACA-0012 airfoil(right). The colormap shows the value of the trajectory-normal repulsion, described by (3.21) and illustrated in Figure 3.10, of the system when integrated backward. The black curve represents the results of the bisection method described in Figure 3.8.

by detecting repelling features in backward time. In Figure 3.11, we show a comparison of the trajectory-normal repulsion factor over an integration time of $T = -0.35$, expressed in the rescaled time of (3.2). This integration time was the longest computational time for which no integration for an initial condition in the domain failed using the LSODA integration pack through SciPy [46]. In backward time, the squared dependence on velocity causes each integration step to get increasingly large.

There are regions, particularly in the velocity space for the flying snake airfoil and the NACA-0012 airfoil, where portions of other trajectories may be more attracting than the nearby TVM over the integration time used. Therefore, we must require additional constraints to identify the TVM. The TVM is the trajectory which maximizes the backward time trajectory-normal repulsion factor.
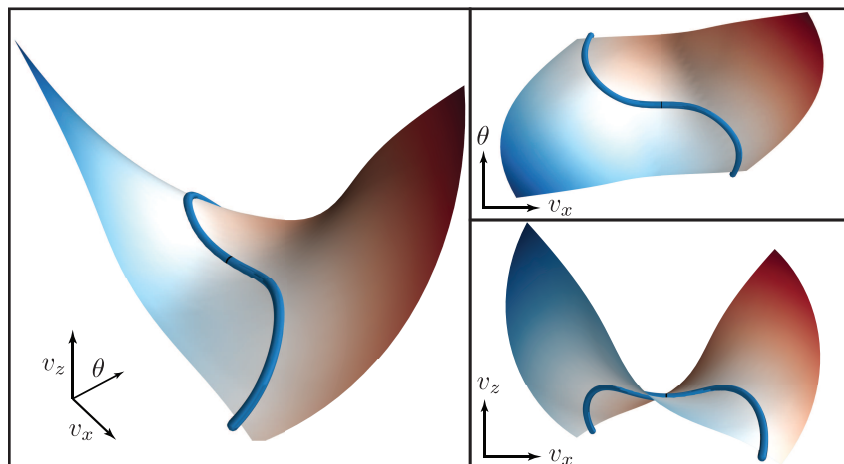
Figure 3.12: The terminal velocity manifold as a 2-dimensional surface embedded in 3-dimensional space for the flat plate for parameter values $\theta \in [-45°, 45°]$. Blue values indicate positive acceleration along the manifold and red values indicate negative acceleration along the manifold, while the 1-dimensional curve shows the equilibrium points of the system, including stable nodes (blue) and the center equilibrium point (black, at the center of the manifold).

3.5 Pitch angle dependence of the terminal velocity manifold

The bifurcation diagrams of Figure 3.5 do not capture how the terminal velocity manifold itself changes with respect to the pitch angle. Therefore, we look at how the terminal velocity manifold changes with pitch angle and visually represent this change in extended phase space. We then prescribe pitch angle control and observe the classical behaviors of gliding and fluttering as occurring along along the extended terminal velocity manifold.

3.5.1 The terminal velocity manifold in extended phase space

To consider the effects of the pitch parameter θ on the TVM, we look to a 3-dimensional extended phase space, including pitch angle as an independent variable without motion. This view of the system allows us to visualize changes of the manifold in the parameter direction while still maintaining the same dynamics of the equations of motion (3.4). We re-cast the
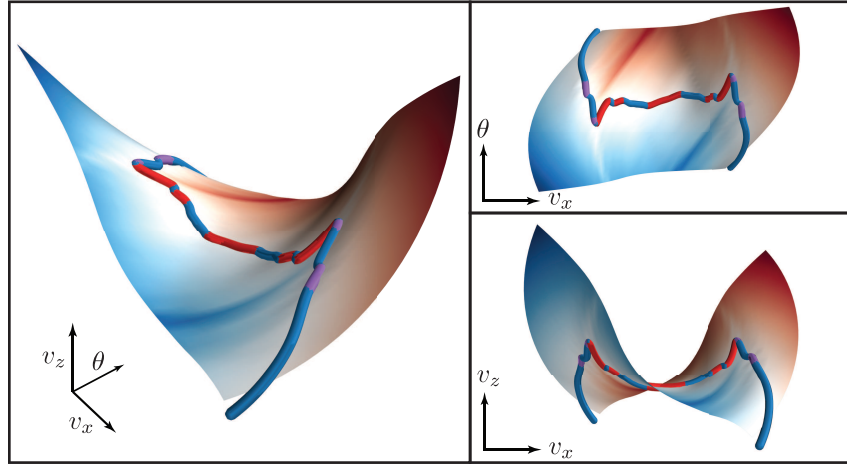
Figure 3.13: The terminal velocity manifold as a 2-dimensional surface embedded in 3-dimensional space for the flying snake airfoil over a pitch domain of $\theta \in [-45°, 45°]$. Blue values indicate positive acceleration along the manifold and red values indicate negative acceleration along the manifold, while the 1-dimensional curve shows the equilibrium points of the system, including stable nodes (blue), saddle points (red), and stable foci (purple).

system into extended phase space with the following equations,

$$
\begin{aligned}
\dot{v}_x &= v^2(C_L\,(\gamma + \theta)\sin\gamma - C_D\,(\gamma + \theta)\cos\gamma), \\
\dot{v}_z &= v^2(C_L\,(\gamma + \theta)\cos\gamma + C_D\,(\gamma + \theta)\sin\gamma) - 1, \\
\dot{\theta} &= 0.
\end{aligned}
\tag{3.23}
$$

In this model, every fixed point of the 2-dimensional system remains a fixed point because of the negligible dynamics, and the motion in the θ-direction is infinitely slow. Therefore, the 1-dimensional TVM will become 2-dimensional as it is extended in the θ-direction. As the accelerations $\dot{v}_x$ and $\dot{v}_z$ depend smoothly on θ, we should be able to uncover a smooth extended TVM. To visualize this, we calculate the 1-dimensional TVM from the 2-dimensional model of (3.4) using the bisection method over a variety of pitch angles and stitch these together to form a 2-dimensional surface in the extended, 3-dimensional model. The resulting surfaces are shown in Figures 3.12, 3.13, and 3.14 over the interval $\theta \in [-45°, 45°]$.

In each figure, the colormap on the surface shows the acceleration at every point on the manifold. Blue regions are associated with positive acceleration and red regions are associated with negative acceleration, where the positive direction is associated with the positive v_x axis. As the TVM is an invariant manifold, the vector field is purely tangential to the
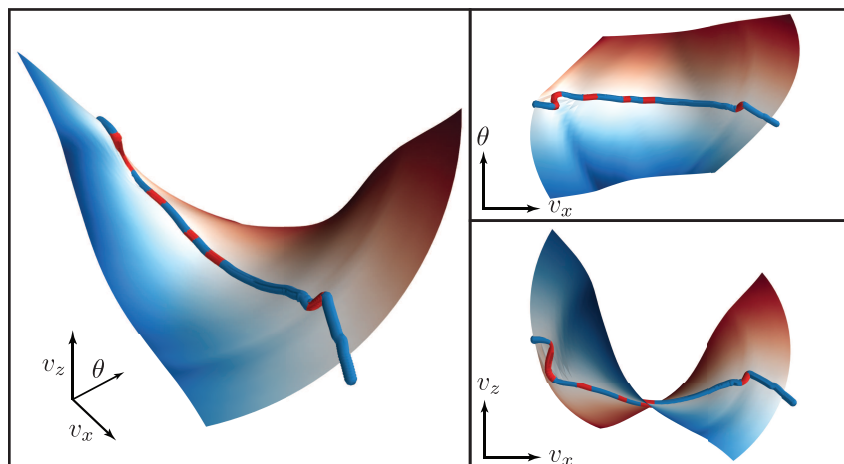
Figure 3.14: The terminal velocity manifold as a 2-dimensional surface embedded in 3-dimensional space for the NACA-0012 airfoil over a pitch domain of $\theta \in [-45°, 45°]$. Blue values indicate positive acceleration along the manifold and red values indicate negative acceleration along the manifold, while the 1-dimensional curve shows the equilibrium points of the system, including stable nodes (blue) and saddle points (red). Equilibrium velocities with a larger horizontal velocity of $|v_x| > 1.5$ were also omitted.

manifold itself. The equilibrium points of the system are shown along the manifold as well, representing the bifurcation diagram of the system. The colors of Figure 3.5 still hold: blue points are stable nodes, red points are saddle points, and purple are stable foci. For the flat plate considered in Figure 3.12, there is a single stable node in all cases, except $\theta = 0$ which contains a stable center manifold. The saddle-node bifurcations of the flying snake are evident in Figure 3.13. The left-right symmetry of these two airfoils is also visible in the anti-symmetry of the TVM in the v_x direction about $\theta = 0$. The NACA-0012 airfoil has a broad range of equilibria over a very small region, showing its sensitivity to pitch angle. In Figure 3.14, we only show equilibria with a horizontal velocity magnitude smaller than 1.5, for comparison at the same scale as the other two TVM figures. As seen in 3.5, there is a wide range of fixed points for this system on the interval $\theta \in [-45°, 45°]$. Outside of this narrow range, all of those fixed points have a much larger magnitude of velocity.

3.5.2 Conceptualizing motion with the terminal velocity manifold

With the 2-dimensional TVM in extended phase space, we now look toward allowing variation in pitch with time. To consider the effects of the fluid moment on the body, it would become

necessary to account for pitch rate in the dynamics of the system. Therefore, we will instead specify controlled pitch kinematics and allow the system to evolve translationally through the 2-dimensional equations of motion of (3.4).

$$
\begin{aligned}
\dot{v}_x &= v^2(C_L\,(\gamma + \theta)\sin\gamma - C_D\,(\gamma + \theta)\cos\gamma), \\
\dot{v}_z &= v^2(C_L\,(\gamma + \theta)\cos\gamma + C_D\,(\gamma + \theta)\sin\gamma) - 1, \\
\dot{\theta} &= \theta(t).
\end{aligned} \tag{3.24}
$$

Note that we are further assuming that $\dot{\theta}$ is small enough to neglect additional forces which arise from pitch dynamics which are considered by, for instance, Andersen et al. [17, 18]. If the pitch dynamics are slower than the motion onto the manifold, then all motion after an initial transient will occur on this higher dimensional TVM. With this in mind, we consider the phenomena of gliding flight and fluttering.

Gliding flight has served as an initial motivation for this model [24]. Therefore, to look at how the motion of a gliding body occurs along the TVM, we consider pitch dynamics which slowly increase throughout the motion. This serves to represent the way that animal gliders begin with an initial downward descent and pitch up before landing [1, 7, 47]. Next, we look to fluttering descent as considered in a variety of studies on falling seeds, disks, and plates [2, 15, 16, 17, 18, 19, 20]. These pitch dynamics are given by slowly oscillating the pitch angle throughout the motion. In real examples, the oscillating pitch angle is the result of varying fluid moments on the body, so we choose a simple sinusoidal oscillation to represent the resulting kinematics. By considering these example motions, we can visualize the ways in which the translational forces considered in this model contribute to the full physics of a passively descending body.

Gliding flight

For animals exhibiting gliding flight, a typical glide includes: (1) an initial, ballistic acceleration; (2) a shallowing glide through the middle of the motion; and finally (3) a landing maneuver in which they slow descent [1, 7]. We represent this behavior here with a simulation of a gliding snake airfoil which increases its pitch angle through the glide, starting from an initially downward pitch angle [34, 47]. This gives a larger initial pitch angle to maximize ballistic acceleration, a shallowing pitch angle through the glide as the animal passes through its maximum lift-to-drag ratio, and finally a pitch up to decelerate overall
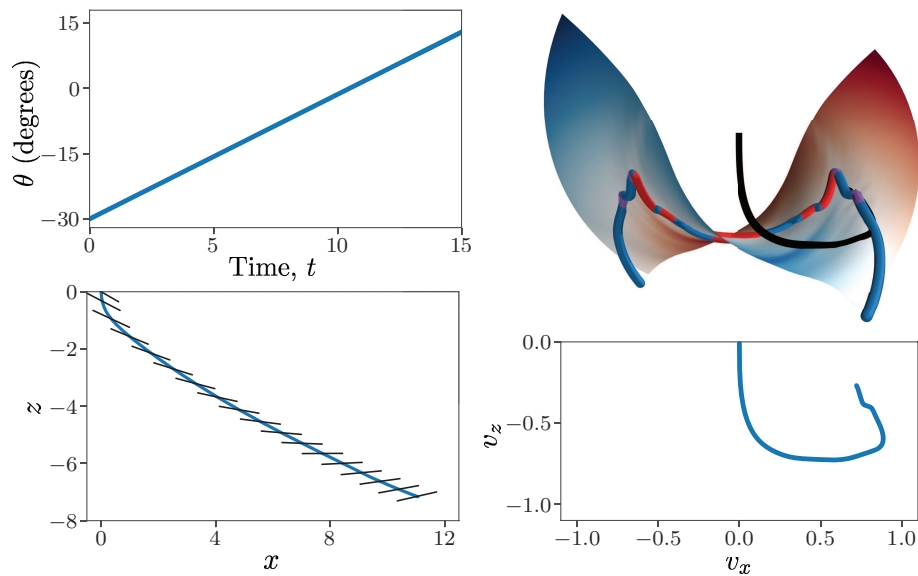
Figure 3.15: In this figure, we show an example glide of a snake-shaped glider with a linearly increasing pitch angle θ with respect to time, as shown in the top-left corner. The resulting motion in physical space is shown in the bottom-left, with the pitch angle marked by the intersecting lines. This motion is shown in extended phase space with respect to the extended TVM in the top-right, with the black line representing the trajectory. The bottom-right panel shows motion in velocity space. The glider is quickly drawn toward fast downward motion, but as it pitches up, the trajectory moves along the terminal velocity manifold toward a stable forward glide before slowing descent just before landing.

for landing. A linear increase in pitch is the simplest way to represent this phenomenon. The results of this linearly increasing pitch angle can be seen in Figure 3.15. The hallmarks of the behavior can be found in the velocity space, which shows the projection of motion in the v_x-v_z plane. Initially, with a negative pitch angle, motion onto the TVM is rapid, and acceleration occurs quickly. Next, the horizontal velocity increases as the glide moves forward. Finally, as the glider's pitch angle levels out, both vertical and horizontal velocity decrease for a safer landing.

Fluttering plates

The fluttering of a thin body through a fluid has been studied extensively in a variety of studies [15, 16, 17, 18, 19, 20]. This is a frequently-observed behavior of passively descending plates characterized by coupled oscillations of pitch angle and horizontal motion as the plate descends vertically. We can emulate this behavior with our extended 3-dimensional model
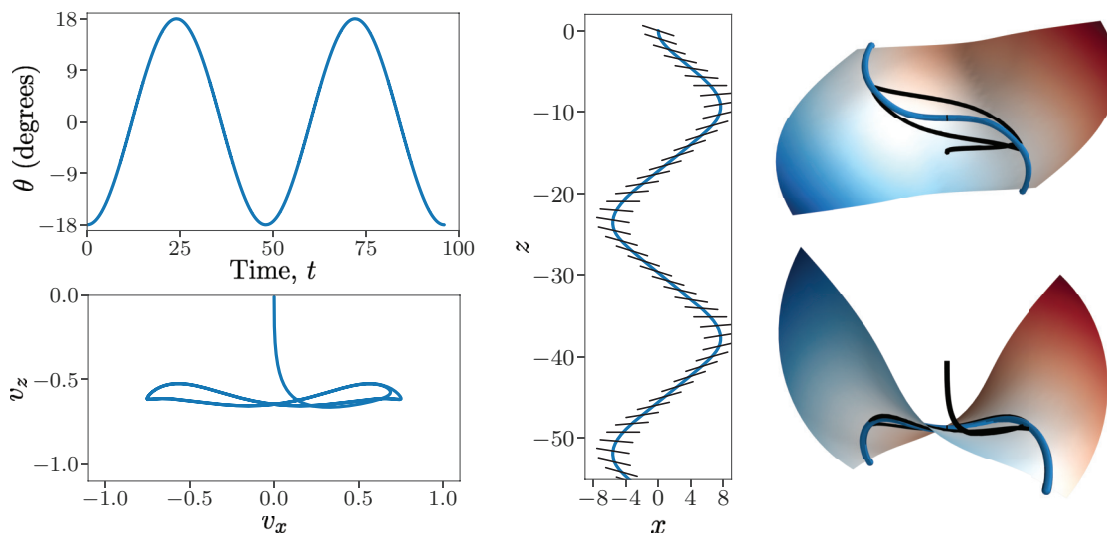
Figure 3.16: In this figure, we show the example of fluttering descent of a flat plate. The controlled pitch angle, θ, varies sinusoidally, as shown in the top-left. The resulting motion in physical space is shown in the central panel, with snapshots of the flat plate shown in black. The motion in extended phase space is shown in the two panels on the right side relative to the terminal velocity manifold. The motion projected into velocity space is shown in the bottom-left corner.

by prescribing oscillating pitch kinematics which are faster than the motion along the TVM but slower than the time scale of motion onto the manifold.

With oscillating pitch control, we are able to replicate dynamics which closely resemble classical fluttering. The trajectory forms a limit cycle oscillation which lies entirely along the extended TVM, as shown in Figure 3.16. The magnitude of controlled oscillations determine the size of the limit cycle.

3.6 Summary and Conclusion

In the present work, we have taken the observation of a terminal velocity manifold (TVM) from Yeaton et al. [24] and placed it on a more mathematically rigorous footing. Through the various methods of computing this curve, we have gained insights into its properties. First, it is the union of all weak stable submanifolds of stable equilibrium points. Because of this structure, computational techniques are required. We have employed a bisection

method to identify the TVM via dichotomy by integrating trajectories in backward time to find their origin. From this method, we have seen that the terminal velocity manifold divides velocity space into trajectories with initial vertical accelerations aligned with the direction of gravity from those which initially accelerate opposite the direction of gravity. We also calculate the trajectory-normal repulsion rate [28] in backward time to show that the TVM is the most normally attracting curve in velocity space in forward time. Finally, we show the terminal velocity manifold in parameter-extended phase space to provide visual intuition for the mechanics of gliding flight and passive descent.

The glider model considered in this paper presents a naturally nonlinear model with interesting mathematical properties. The TVM represents an epsilon-free slow-fast system in which there is a separation of time scales without an explicit slow parameter, and the methods discussed in this paper to discover the TVM may have implications for the analysis of other slow-fast systems. This model also presents the challenge of analyzing functional parameters in a system. Through our proof of fixed point conditions, we show one way in which these kinds of functional parameters may be analyzed, deducing information about the system based on the constraints on the space of possible functions. In this case, the physical assumption of finite lift-to-drag ratio gave insight into the possible equilibria of the system. This work provides a new physical intuition into the behavior of gliding bodies, and demonstrates a variety of methods for the computation of influential geometric structures in mathematical models.

Acknowledgments

Bibliography

[1] Farid Socha, John J.and Jafari, Yonatan Munk, and Greg Byrnes. How animals glide: from trajectory to morphology. *Canadian Journal of Zoology*, 93(12):901–924, 2015.

[2] Shizuka Minami and Akira Azuma. Various flying modes of wind-dispersal seeds. *Journal of Theoretical Biology*, 225(1):1–14, 2003.

[3] Stephen M. Jackson. Glide angle in the genus Petaurus and a review of gliding in mammals. *Mammal Review*, 30(1):9–30, 2000.

[4] Karl Vernes. Gliding performance of the northern flying squirrel (*glaucomys sabrinus*) in mature mixed forest of eastern Canada. *Journal of Mammalogy*, 82(4):1026–1033, 2001.

[5] Robert McGuire, Jimmy A.and Dudley. The cost of living large: comparative gliding performance in flying lizards (Agamidae: *Draco*). *The American Naturalist*, 166(1): 93–106, 2005.

[6] John J. Socha, Kevin Miklasz, Farid Jafari, and Pavlos P. Vlachos. Non-equilibrium trajectory dynamics and the kinematics of gliding in a flying snake. *Bioinspiration & Biomimetics*, 5(4):045002, 2010.

[7] Joseph W. Bahlman, Sharon M. Swartz, Daniel K. Riskin, and Kenneth S. Breuer. Glide performance and aerodynamics of non-equilibrium glides in northern flying squirrels (*glaucomys sabrinus*). *Journal of The Royal Society Interface*, 10(80):20120794, 2013.

[8] Steven Vogel. *Life in moving fluids: the physical biology of flow.* Princeton University Press, 1994.

[9] Mirko Kovač, Oriol Fauria, Jean-Christophe Zufferey, Dario Floreano, et al. The EPFL jumpglider: A hybrid jumping and gliding robot with rigid or folding wings. In *Robotics and Biomimetics (ROBIO), 2011 IEEE international conference on*, pages 1503–1508. IEEE, 2011.

[10] Jonathan E. Dickson, James D.and Clark. Design of a multimodal climbing and gliding robotic platform. *IEEE/ASME Transactions on Mechatronics*, 18(2):494–505, 2013.

[11] Naomi E. Leonard, Derek A. Paley, Russ E. Davis, David M. Fratantoni, Francois Lekien, and Fumin Zhang. Coordinated control of an underwater glider fleet in an adaptive ocean sampling field experiment in Monterey Bay. *Journal of Field Robotics*, 27(6):718–740, 2010.

[12] James Clerk Maxwell. On a particular case of the descent of a heavy body in a resisting medium. *The Cambridge and Dublin Mathematical Journal*, 9:145–148, 1854.

[13] Horace Lamb. *Hydrodynamics*. Cambridge University Press, 1932.

[14] Aleksandr A. Andronov, Aleksandr A. Vitt, and Semen E. Khaikin. *Theory of Oscillators: Adiwes International Series in Physics*, volume 4. Elsevier, 2013.

[15] Stuart B. Field, M. Klaus, M. G. Moore, and Franco Nori. Chaotic dynamics of falling disks. *Nature*, 388(6639):252–254, 1997.

[16] Patricia Ern, Frédéric Risso, David Fabre, and Jacques Magnaudet. Wake-induced oscillatory paths of bodies freely rising or falling in fluids. *Annual Review of Fluid Mechanics*, 44:97–121, 2012.

[17] A. Andersen, U. Pesavento, and Z. Jane Wang. Unsteady aerodynamics of fluttering and tumbling plates. *Journal of Fluid Mechanics*, 541:65–90, 2005.

[18] A. Andersen, U. Pesavento, and Z. Jane Wang. Analysis of transitions between fluttering, tumbling and steady descent of falling cards. *Journal of Fluid Mechanics*, 541: 91–104, 2005.

[19] Daniel Tam, John W.M. Bush, Michael Robitaille, and Arshad Kudrolli. Tumbling dynamics of passive flexible wings. *Physical Review Letters*, 104(18):184504, 2010.

[20] Lionel Vincent, W. Scott Shambaugh, and Eva Kanso. Holes stabilize freely falling coins. *Journal of Fluid Mechanics*, 801:250–259, 2016.

[21] Hassan Aref and Scott W. Jones. Chaotic motion of a solid through ideal fluid. *Physics of Fluids A: Fluid Dynamics*, 5(12):3026–3028, 1993.

[22] Alexey V. Borisov, Ivan S. Mamaev, and Sergey M. Ramodanov. Dynamic interaction of point vortices and a two-dimensional cylinder. *Journal of Mathematical Physics*, 48 (6):065403, 2007.

[23] Johan Roenby and Hassan Aref. Chaos in body–vortex interactions. *Proceedings of the Royal Society of London A: Mathematical, Physical and Engineering Sciences*, 466 (2119):1871–1891, 2010.

[24] Isaac J. Yeaton, John J. Socha, and Shane D. Ross. Global dynamics of non-equilibrium gliding in animals. *Bioinspiration & Biomimetics*, 12(2):026013, 2017.

[25] Stephen Wiggins. *Normally hyperbolic invariant manifolds in dynamical systems*, volume 105. Springer Science & Business Media, 2013.

[26] Ioannis G Kevrekidis, C William Gear, James M Hyman, Panagiotis G Kevrekidid, Olof Runborg, Constantinos Theodoropoulos, et al. Equation-free, coarse-grained multiscale computation: Enabling mocroscopic simulators to perform system-level analysis. *Communications in Mathematical Sciences*, 1(4):715–762, 2003.

[27] Shawn C. Shadden, Francois Lekien, and Jerrold E. Marsden. Definition and properties of lagrangian coherent structures from finite-time lyapunov exponents in two-dimensional aperiodic flows. *Physica D: Nonlinear Phenomena*, 212(3):271–304, 2005.

[28] George Haller. A variational theory of hyperbolic Lagrangian coherent structures. *Physica D: Nonlinear Phenomena*, 240(7):574–598, 2011.

[29] George Haller. Lagrangian Coherent Structures. *Annual Review of Fluid Mechanics*, 47 (1):137–162, 2015.

[30] Z. Jane Wang and Michael H. Birch, James M .and Dickinson. Unsteady forces and flows in low Reynolds number hovering flight: two-dimensional computations vs robotic wing experiments. *Journal of Experimental Biology*, 207(3):449–460, 2004.

[31] Daniel Holden, John J. Socha, Nicholas D. Cardwell, and Pavlos P. Vlachos. Aerodynamics of the flying snake *chrysopelea paradisi*: how a bluff body cross-sectional shape

contributes to gliding performance. *The Journal of Experimental Biology*, 217(3):382–394, 2014.

[32] Robert E. Sheldahl and Paul C. Klimas. Aerodynamic characteristics of seven symmetrical airfoil sections through 180-degree angle of attack for use in aerodynamic analysis of vertical axis wind turbines. Technical report, Sandia National Labs., Albuquerque, NM (USA), 1981.

[33] John J. Socha. Gliding flight in *chrysopelea*: Turning a snake into a wing. *Integrative and Comparative Biology*, 51(6):969–982, 2011.

[34] John J Socha. Kinematics: Gliding flight in the paradise tree snake. *Nature*, 418(6898):603–604, 2002.

[35] Farid Jafari, Shane D. Ross, Pavlos P. Vlachos, and John J. Socha. A theoretical analysis of pitch stability during gliding in flying snakes. *Bioinspiration & Biomimetics*, 9(2):025014, 2014.

[36] Anush Krishnan, John J. Socha, Pavlos P. Vlachos, and L.A. Barba. Lift and wakes of flying snakes. *Physics of Fluids*, 26(3):031901, 2014.

[37] Farid Jafari, Sevak Tahmasian, Shane D. Ross, and John J. Socha. Control of gliding in a flying snake-inspired n-chain model. *Bioinspiration & Biomimetics*, 12(6):066002, 2017.

[38] Wang Sang Koon, Martin W Lo, Jerrold E Marsden, and Shane D. Ross. *Dynamical systems, the three-body problem and space mission design.* Citeseer, 2008.

[39] Christian Kuehn. *Multiple time scale dynamics*, volume 1. Springer, 2016.

[40] Bernd Krauskopf, Hinke M. Osinga, Eusebius J. Doedel, Michael E. Henderson, John Guckenheimer, Alexander Vladimirsky, Michael Dellnitz, and Oliver Junge. A survey of methods for computing (un) stable manifolds of vector fields. *International Journal of Bifurcation and Chaos*, 15(03):763–791, 2005.

[41] Shibabrat Naik and Shane D. Ross. Geometry of escaping dynamics in nonlinear ship motion. *Communications in Nonlinear Science and Numerical Simulation*, 47:48–70, 2017.

[42] Neil Fenichel. Geometric singular perturbation theory for ordinary differential equations. *Journal of Differential Equations*, 31(1):53–98, 1979.

[43] Christopher K.R.T. Jones. Geometric singular perturbation theory. In *Dynamical Systems*, pages 44–118. Springer, 1995.

[44] Peter M. Battelino, Celso Grebogi, Edward Ott, James A. Yorke, and Ellen D. Yorke. Multiple coexisting attractors, basin boundaries and basic sets. *Physica D: Nonlinear Phenomena*, 32(2):296–305, 1988.

[45] Joseph D. Skufca, James A. Yorke, and Bruno Eckhardt. Edge of chaos in a parallel shear flow. *Physical Review Letters*, 96(17):174101, 2006.

[46] Eric Jones, Travis Oliphant, and Pearu Peterson. {SciPy}: open source scientific tools for {Python}. 2014.

[47] Kristin L Bishop. The relationship between 3-D kinematics and gliding performance in the southern flying squirrel, *glaucomys volans*. *Journal of Experimental Biology*, 209(4): 689–701, 2006.

Chapter 4

The normal repulsion rate

Abstract

This paper introduces the trajectory divergence rate, a scalar field which locally gives the instantaneous attraction or repulsion of adjacent trajectories. This scalar field may be used to find highly attracting or repelling invariant manifolds, such as slow manifolds, to rapidly approximating hyperbolic Lagrangian coherent structures, or to provide the local stability of invariant manifolds. This work presents the derivation of the trajectory divergence rate and the related trajectory divergence ratio for 2-dimensional systems, investigates their properties, shows their application to several example systems, and presents their extension to higher dimensions.

Attribution

This chapter represents a collaborative work with Peter J. Nolan and Shane D. Ross, which is presently under review in *Nonlinear Dynamics*. Mr. Nolan's contributions include the work with the ocean model and calculation of Lagrangian coherent structures for the comparison presented in Sec. 4.4.2. Dr. Ross contributed collaboratively to the development of the ideas and derivation of the main result through frequent meetings and conversations.

Acknowledgments

4.1   Introduction

To better understand the properties of mathematical models and experimental measurements, it is often convenient to look at the geometric structure of the flow of a resulting vector fields. There often exist lower-dimensional manifolds which dominate the attraction and repulsion, swirling, or shearing of trajectories advecting under the flow. Methods to find such structures have been applied to better understand topics including plant pathogen spread [1], animal locomotion [2, 3], seabird foraging patterns [4], geophysical flows [5, 6], chemical reactions [7], comet distributions [7], and structural mechanics [7].

In autonomous systems, the simplest geometric structure of interest is the fixed point, which is a 0-dimensional invariant manifold in the flow. Stable, unstable, and center manifolds of a fixed point may be calculated through a number of classical methods, including "growing" the stable or unstable manifolds by integrating the eigendirections of fixed points backward or forward in time [8]. However, in the context of weak stable submanifolds, these methods begin to break down [3]. Some weak submanifolds are part of a class of geometric structures known as *slow manifolds* which exhibit a separation of time scales [9], attracting or repelling other trajectories in phase space. This difference in time scales between motion along a slow manifold and the motion normal to it allows them to be classified as normally hyperbolic invariant manifolds (NHIMs) [10].

Geometric structure may also be present in the absence of fixed points or slow manifolds. Recent developments in dynamical systems have led to several useful generalizations of some key geometric features. Distinguished hyperbolic trajectories generalize stable and unstable manifolds to aperiodic flows, and are identified using the "M-function" [11]. Hyperbolic coherent structures represent dynamically evolving transport barriers in flows [12, 13]. Although the methods of coherent structures are typically situated within the context of fluid dynamics, such structures have applications to the flow of general vector fields [3, 14, 15, 16].

Detecting and analyzing the underlying structures of flows gives a better understanding of how the system evolves, whether that flow represents the motion of a fluid or some other general dynamical system.

Methods to identify coherent structures may be based on integrated trajectory information or may be calculated from the instantaneous vector field for the entire volume. Most state of the art methods are trajectory-based, using finite-time integration of trajectories to calculate coherent structures [13, 17]. There is a wide variety of trajectory-based methods to identify coherent structures or coherent sets, including transfer operator methods [18, 19], topological methods [20, 21], and stretching-based methods such as the finite-time Lyapunov exponent (FTLE) [12]; see Hadjighasem et al. [22] for a review. However, trajectory-based methods involve significant computational resources, requiring trajectory integration over an ensemble of initial conditions [23, 24].

There is much to be gained by looking at the instantaneous information of vector fields. Although the trajectory-dependent coherent structures are more robust to the flow, the short time behavior of these structures may be of interest [25]. Vector field schemes are also much more computationally efficient, and their changes can be tracked in time for nonautonomous flows. Historically, most vector field-based methods have focused on elliptic, or vortex-like, coherent structures [26]. More recent work has developed the notion of objective Eulerian coherent structures for 2-dimensional flows [27], which include hyperbolic and parabolic structures in addition to objectively defined elliptic coherent structures. However, while objectivity is necessary for detecting, for instance, vortex-like coherent structures in a fluid, objectivity may be a disadvantage in other examples of dynamical systems [28, 29].

4.1.1 Main result

This paper introduces the *trajectory divergence rate* for 2-dimensional vector fields, given by Eq. (4.17),

$$\dot{\rho} = \mathbf{n}^\dagger \mathbf{S} \mathbf{n},$$

where $\mathbf{n} = \mathbf{R}\mathbf{v}/|\mathbf{v}|$ is the unit normal vector field, and $\mathbf{S} = \frac{1}{2}\left(\nabla\mathbf{v} + (\nabla\mathbf{v})^\dagger\right)$ is the rate-of-strain tensor, representing the symmetric component of the Jacobian of the system. In this work, the dagger, $(\cdot)^\dagger$, indicates the matrix transpose to avoid confusion with time-integrated methods. The trajectory divergence rate is an inherent property of C^1 vector fields, measur-

ing the extent to which the trajectory passing through each point instantaneously repels or attracts nearby trajectories. This paper will show that this quantity may be used as a diagnostic tool to approximate slow manifolds and hyperbolic coherent structures by showing regions of strong instantaneous repulsion or attraction.

Instantaneous attraction and repulsion has been considered previously, through other metrics such as the normal infinitesimal Lyapunov exponent (NILE) [25] and the strain acceleration tensor [30]. These methods have primarily been applied to partition the space or look into regions of local stability or instability, particularly within applications of turbulence. The trajectory divergence rate introduced herein is intended to serve as a "rough and ready" method for approximating hyperbolic, or stretching-based, geometric structures in the flows of general nonlinear dynamical systems. Much like local curvature [31], this quantity may be thought of as an inherent property of continuously differentiable vector fields, showing the instantaneous local divergence or convergence of nearby trajectories. Under certain conditions, the regions of highest local divergence or convergence serve to approximate finite-time coherent structures.

The idea of stability is asymptotic in nature; a stable invariant manifold is one for which nearby trajectories stay close for $t \to \infty$. Although transport barriers and invariant manifolds in flows are calculated based on the long-term dynamics of the system, and therefore the long-term repulsion of the manifold in question, the instantaneous repulsion of invariant manifolds provides additional insights into the character of an invariant manifold, as regions of a globally attracting invariant manifold may be instantaneously repelling [30, 32]. The trajectory divergence rate is easily computable, requiring only the vector field and its gradient, and can serve as a useful diagnostic in the search for influential geometric structures in flows.

Section 4.2 gives the mathematical preliminaries and notation to provide the mathematical context for the divergence rate. Section 4.3 shows the derivation of the trajectory divergence rate and discusses its properties. Section 4.4 shows several applications of the divergence rate over a different situations in which it may prove useful. Section 4.5 extends the trajectory divergence rate from 2-dimensional to higher dimensional systems and provides a 3-dimensional example. Finally, Section 4.6 provides some discussion about the work of this paper to conclude the work.

4.2   Background and notation

To begin, consider a general 2-dimensional, autonomous ordinary differential equation

$$\dot{\mathbf{x}} = \mathbf{v}(\mathbf{x}), \quad \mathbf{x} \in U \subseteq \mathbb{R}^2, \, t \in \mathbb{R}, \tag{4.1}$$

with its time-T mapping all initial conditions forward to their positions after a duration T,

$$\begin{aligned} \mathbf{F}_T : U &\to U, \quad T \in \mathbb{R}, \\ \mathbf{x}_0 &\mapsto \mathbf{x}_T = \mathbf{x}(T; \mathbf{x}_0). \end{aligned} \tag{4.2}$$

For any $\mathbf{x} \in U$ with $\mathbf{v}(\mathbf{x}) \neq \mathbf{0}$ (that is, excluding equilibrium points), one can define the following unit vector fields parallel and normal to the governing vector field $\mathbf{v}(\mathbf{x})$, respectively,

$$\begin{aligned} \mathbf{e}(\mathbf{x}) &= \frac{\mathbf{v}(\mathbf{x})}{|\mathbf{v}(\mathbf{x})|}, \\ \mathbf{n}(\mathbf{x}) &= \mathbf{R}\mathbf{e}(\mathbf{x}), \quad \mathbf{R} = \begin{pmatrix} 0 & -1 \\ 1 & 0 \end{pmatrix}. \end{aligned} \tag{4.3}$$

The gradient of the time-T flow map $\nabla \mathbf{F}_T$ defines a mapping from vectors based at $\mathbf{x}_0$, such as $\mathbf{e}(\mathbf{x}_0)$ and $\mathbf{n}(\mathbf{x}_0)$, to vectors based at $\mathbf{x}_T$, showing how those vectors deform with the flow. The tangent vector, in general, maps to the new tangent direction, but the normal vector does not map to the normal direction at time T due to the shear of the flow.

4.2.1   Trajectory-normal repulsion rate

For any trajectory passing through a point $\mathbf{x}_0 \in U$ with $\mathbf{v}(\mathbf{x}_0) \neq \mathbf{0}$, the *trajectory-normal repulsion rate* $\rho_T(\mathbf{x}_0)$ [28] over the time interval $[0, T]$ may be defined locally as the projection of $\nabla \mathbf{F}_T(\mathbf{x}_0)\mathbf{n}_0$ onto the new normal vector $\mathbf{n}_T$,

$$\rho_T(\mathbf{x}_0) = \langle \mathbf{n}_T, \nabla \mathbf{F}_T(\mathbf{x}_0)\mathbf{n}_0 \rangle, \tag{4.4}$$

where $\mathbf{n}_T = \mathbf{n}(\mathbf{x}_T) = \mathbf{n}(\mathbf{F}_T(\mathbf{x}_0))$ and $\langle \cdot, \cdot \rangle$ is the usual inner product in $\mathbb{R}^2$. As illustrated in Figure 4.1, $\rho_T(\mathbf{x}_0)$ is a measure of the growth of infinitesimal perturbations normal to the invariant manifold containing $\mathbf{x}_0$ over the time interval $[0, T]$. If the projection $\rho_T(\mathbf{x}_0) > 1$,
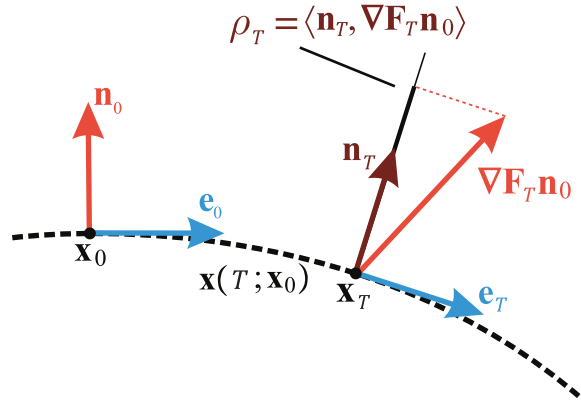
Figure 4.1: Geometry of the trajectory-normal repulsion rate, reproduced from [3].

then infinitesimal perturbations normal to the trajectory through $\mathbf{x}_0$ grow over the time interval $[0, T]$. Note that, although overall growth over the duration T may be repelling (attracting), it is possible for the invariant manifold to be instantaneously attracting (repelling) [32].

This scalar field $\rho_T(\mathbf{x}_0)$ can be used to extract the most influential invariant manifolds in the flow, in the sense that it reveals those manifolds that normally repel (or attract) other manifolds at the largest rate. Using this trajectory-normal repulsion rate, one can calculate, for example, slow-manifolds, such as those found in the examples below.

4.2.2 Trajectory-normal repulsion ratio

A related quantity is the *trajectory-normal repulsion ratio* [28], which is the ratio of normal repulsion to the tangential stretching along an invariant manifold passing through the point $\mathbf{x}_0$ over the time interval $[0, T]$,

$$\nu_T(\mathbf{x}_0) = \frac{\rho_T(\mathbf{x}_0)}{|\nabla \mathbf{F}_T(\mathbf{x}_0)\mathbf{e}_0|}. \tag{4.5}$$

Where the trajectory-normal repulsion ratio $\nu_T(\mathbf{x}_0) > 1$, the normal stretching dominates the tangential stretching of the curve.

Both the trajectory-normal repulsion rate and trajectory-normal repulsion ratio can be written in terms of the right Cauchy-Green tensor $\mathbf{C}_T(\mathbf{x}_0)$, well-known from continuum mechanics

[33], as well as its use in FTLE and LCS calculations [28],

$$\rho_T(\mathbf{x}_0) = \sqrt{\frac{|\mathbf{v}(\mathbf{x}_0)|^2 \det \mathbf{C}_T(\mathbf{x}_0)}{\langle \mathbf{v}(\mathbf{x}_0), \mathbf{C}_T(\mathbf{x}_0)\mathbf{v}(\mathbf{x}_0)\rangle}}$$

$$\nu_T(\mathbf{x}_0) = \frac{|\mathbf{v}(\mathbf{x}_0)|^2 \sqrt{\det \mathbf{C}_T(\mathbf{x}_0)}}{\langle \mathbf{v}(\mathbf{x}_0), \mathbf{C}_T(\mathbf{x}_0)\mathbf{v}(\mathbf{x}_0)\rangle}$$

(4.6)

As a matter of notation, in this work $(\cdot)_T$ will indicate a value calculated over the interval $[0, T]$ and $(\cdot)^\dagger$ will indicate the matrix transpose. Note that T may be positive or negative. Because of their dependence on the normal vector in the derivation of these expressions, these scalar fields both remain defined only for 2-dimensional systems.

When both $\rho_T(\mathbf{x}) > 1$ and $\nu_T(\mathbf{x}) > 1$ for all $\mathbf{x} \in \gamma$, where γ is an invariant manifold, and γ is a ridge of the ρ_T-field, γ is a constrained Lagrangian coherent structure [28], in the sense that the variational search for attracting or repelling curves is constrained to the space of invariant manifolds.

4.3   The trajectory divergence rate

The trajectory-normal repulsion rate ρ_T may be useful in finding attracting (or repelling) structures in a 2-dimensional flow [28], but calculation of the time-T flow map over the domain of interest is computationally expensive. Therefore, this work seeks an instantaneous measure that gives the leading order behavior of this scalar field.

For scalar and tensor fields, the dependence on $\mathbf{x}_0$ will be notationally dropped for clarity, as it will be understood. For small time T, the right Cauchy-Green tensor, $\mathbf{C}_T$, may be expanded in terms of integration time T,

$$\mathbf{C}_T = \mathbf{C}_0 + \left.\frac{d\mathbf{C}_T}{dT}\right|_{T=0} T + \frac{1}{2} \left.\frac{d^2\mathbf{C}_T}{dT^2}\right|_{T=0} T^2 + \cdots$$

(4.7)

Because all derivatives are evaluated at $T = 0$, $\left.\frac{d}{dt}\right|_{t=0} = \left.\frac{d}{dT}\right|_{t=0}$. The derivatives of the right
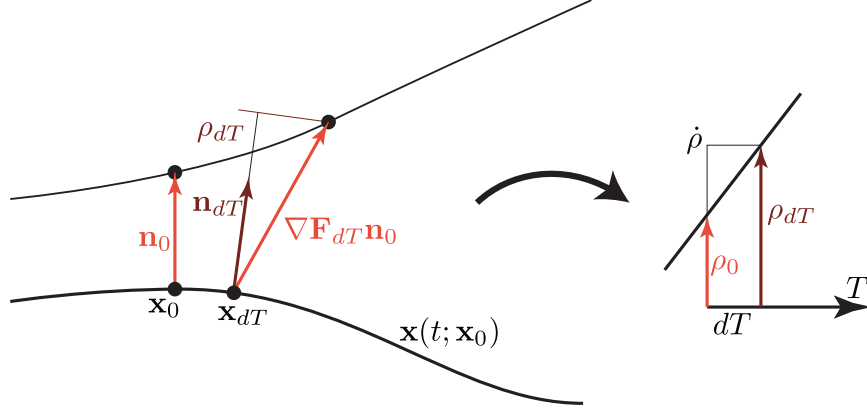
Figure 4.2: This schematic shows the relationship between the divergence rate and the time-T repulsion rate ρ_T. The divergence rate is the instantaneous rate of change of the repulsion rate, which is therefore signified as $\dot\rho$.

Cauchy-Green are given by the Rivlin-Ericksen tensors [33],

$$
\begin{aligned}
\frac{d^k \mathbf{C}_T}{dt^k} &= \nabla \frac{d\mathbf{x}}{dt} + \left(\nabla \frac{\mathbf{x}}{dt} \right)^\dagger, & k = 1, \\
\frac{d^k \mathbf{C}_T}{dt^k} &= \nabla \frac{d^k \mathbf{x}}{dt^k} + \left(\nabla \frac{d^k \mathbf{x}}{dt^k} \right)^\dagger + \sum_{i=1}^{k-1} \binom{k}{i} \left(\nabla \frac{d^i \mathbf{x}}{dt^i} \right)^\dagger \nabla \frac{d^{k-i} \mathbf{x}}{dt^{k-i}}, & k \geq 2.
\end{aligned}
\tag{4.8}
$$

For small $T \ll 1$, the leading order behavior is given by the first Rivlin-Ericken tensor $(\nabla \mathbf{v} + (\nabla \mathbf{v})^\dagger)$. Neglecting higher order dependence on T, the expansion of the Cauchy-Green tensor (4.7) simplifies to,

$$
\mathbf{C}_T = \mathbf{I} + 2\mathbf{S}T + \mathcal{O}(T^2),
\tag{4.9}
$$

where $\mathbf{S}$ represents the symmetric rate-of-strain tensor, defined as,

$$
\mathbf{S} = \tfrac{1}{2} \left(\nabla \mathbf{v} + \nabla \mathbf{v}^\dagger \right).
\tag{4.10}
$$

This expansion of the Cauchy-Green tensor admits the small time expansion for the trajectory-normal repulsion rate from (4.4) and Fig. 4.1. For a 2-dimensional system, the following identity allows the expansion of the determinant within the trajectory-normal repulsion rate,

$$
\det(\mathbf{A} + \mathbf{B}) = \det \mathbf{A} + \det \mathbf{B} + \det \mathbf{A} \cdot \mathrm{tr}(\mathbf{A}^{-1}\mathbf{B}),
\tag{4.11}
$$

Neglecting the higher order dependence on T in (4.9) admits the substitution $\mathbf{C}_T = \mathbf{I} + 2T\mathbf{S}$. Therefore, $\det \mathbf{C}_T$, can be expressed as,

$$
\begin{aligned}
\det \mathbf{C}_T &= \det(\mathbf{I} + 2T\mathbf{S}) \\
&= \det(\mathbf{I}) + \det(2T\mathbf{S}) + \det(\mathbf{I})\mathrm{tr}(2T\mathbf{I}^{-1}\mathbf{S}) \\
&= 1 + 4T^2 \det(\mathbf{S}) + 2T\mathrm{tr}(\mathbf{S}) \\
&= 1 + 2T\mathrm{tr}(\mathbf{S}) + \mathcal{O}(T^2).
\end{aligned}
\tag{4.12}
$$

To finish the expansion of (4.6), the same substitution $\mathbf{C}_T = \mathbf{I} + 2T\mathbf{S}$ gives the following result.

$$
\begin{aligned}
\frac{|\mathbf{v}|^2}{\mathbf{v}^\dagger \mathbf{C}_T \mathbf{v}} &= \frac{|\mathbf{v}|^2}{|\mathbf{v}|^2 + 2T\mathbf{v}^\dagger \mathbf{S}\mathbf{v} + \mathcal{O}(T^2)} \\
&= \frac{1}{1 + \frac{1}{|\mathbf{v}|^2} 2T\mathbf{v}^\dagger \mathbf{S}\mathbf{v} + \mathcal{O}(T^2)} \\
&= 1 - 2T \frac{\mathbf{v}^\dagger \mathbf{S}\mathbf{v}}{|\mathbf{v}|^2} + \mathcal{O}(T^2)
\end{aligned}
\tag{4.13}
$$

Combining these two substitutions gives the following relation for the trajectory-normal repulsion ratio.

$$
\begin{aligned}
\rho_T &= \sqrt{\frac{|\mathbf{v}|^2 \det \mathbf{C}_T}{\mathbf{v}^\dagger \mathbf{C}_T \mathbf{v}}} \\
&= \sqrt{\left(1 + 2T\mathrm{tr}\left(\mathbf{S}\left(\mathbf{x}_0\right)\right) + \mathcal{O}(T^2)\right)\left(1 - 2T\frac{\mathbf{v}^\dagger \mathbf{S}\mathbf{v}}{|\mathbf{v}|^2} + \mathcal{O}(T^2)\right)} \\
&= 1 + \left(\mathrm{tr}(\mathbf{S}) - \frac{\mathbf{v}^\dagger \mathbf{S}\mathbf{v}}{|\mathbf{v}|^2}\right)T + \mathcal{O}(T^2)
\end{aligned}
\tag{4.14}
$$

Neglecting higher order terms for small T,

$$
\rho_T = 1 + \left(\mathrm{tr}(\mathbf{S}) - \frac{\mathbf{v}^\dagger \mathbf{S}\mathbf{v}}{|\mathbf{v}|^2}\right)T
\tag{4.15}
$$

Therefore, the leading order behavior of ρ_T for small T is given entirely by the quantity $\dot{\rho} = \frac{d\rho_T}{dT}\big|_{T=0}$,

$$
\dot{\rho} = \mathrm{tr}(\mathbf{S}) - \frac{\mathbf{v}^\dagger \mathbf{S}\mathbf{v}}{|\mathbf{v}|^2}
\tag{4.16}
$$

which is the *trajectory divergence rate*. Fig. 4.2 shows a schematic of the geometric interpretation of this derivation.

This quantity is independent of the choice of the time parameter T, and, furthermore, does not require integration to be calculated. It is dependent solely on the given vector field $\mathbf{v}(\mathbf{x})$ and its gradient through the rate-of-strain tensor $\mathbf{S}$. As shown in Appendix 4.7, for 2-dimensional systems, this expression reduces to simply

$$\dot{\rho} = \mathbf{n}^{\dagger}\mathbf{S}\mathbf{n} \tag{4.17}$$

The instantaneous rate of normal repulsion is given by a quadratic form on the rate-of-strain tensor by the unit normal vector. The trajectory divergence rate can also be derived via the following expression for the rate of change of length of an infinitesimal vector ℓ,

$$\frac{1}{2}\frac{d}{dt}|\ell|^2 = \ell^{\dagger}\mathbf{S}\ell. \tag{4.18}$$

4.3.1   Trajectory divergence ratio

Following the same procedure as the expansion of the repulsion rate, the trajectory-normal repulsion ratio may be expanded by,

$$\nu_T = \frac{|\mathbf{v}|^2\sqrt{\det\mathbf{C}_T}}{\langle\mathbf{v}, \mathbf{C}_T\mathbf{v}\rangle}, \tag{4.19}$$

for small T to find its instantaneous rate of growth. From (4.12),

$$\sqrt{\det\mathbf{C}_T} = 1 + T\operatorname{tr}(\mathbf{S}) + \mathcal{O}(T^2), \tag{4.20}$$

and using (4.13),

$$\begin{aligned}
\nu_T &= \left(1 + T\operatorname{tr}(\mathbf{S}) + \mathcal{O}(T^2)\right)\left(1 - 2T\frac{\mathbf{v}^{\dagger}\mathbf{S}\mathbf{v}}{|\mathbf{v}|^2} + \mathcal{O}(T^2)\right) \\
&= 1 + T\left(\operatorname{tr}(\mathbf{S}) - 2\frac{\mathbf{v}^{\dagger}\mathbf{S}\mathbf{v}}{|\mathbf{v}|^2}\right) + \mathcal{O}(T^2)
\end{aligned} \tag{4.21}$$
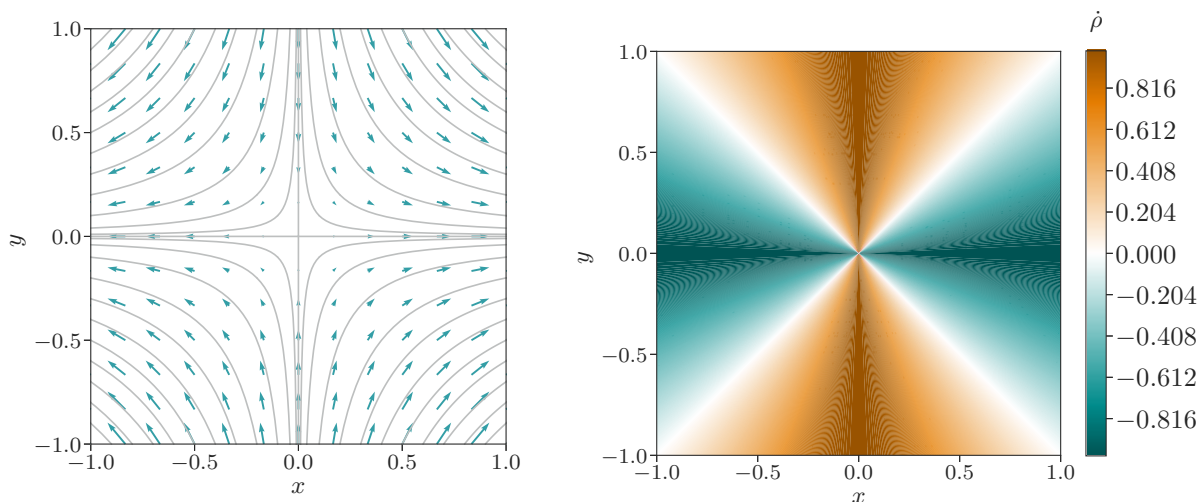
Figure 4.3: The phase portrait (left) and trajectory divergence rate field (right) for Example 4.1.

And the rate of ν_T is given as

$$\dot{\nu} = \frac{\mathbf{v}^\dagger \left(\mathrm{tr}(\mathbf{S})\mathbf{I} - 2\mathbf{S} \right) \mathbf{v}}{|\mathbf{v}|^2} \tag{4.22}$$

Similar to the trajectory divergence rate $\dot{\rho}$, the divergence rate is dependent only on the rate-of-strain tensor and therefore does not require the calculation of trajectories. These scalar fields give a measurement of the instantaneous stretching of normal vectors throughout phase space and can be used to find the most attracting and repelling structures with much less computational cost.

4.3.2 Physical interpretation of the trajectory divergence rate

The trajectory divergence rate provides a scalar measurement of how much a trajectory is attracting or repelling nearby trajectories, representing the time-normalized slope of the normal distance between nearby trajectories, as visualized in Figure 4.2. Therefore, as shown in Figure 4.4, a positive divergence rate indicates diverging trajectories, a negative divergence rate indicates converging trajectories, and a zero divergence rate shows the regions of the flow where trajectories are parallel. To visualize this, consider the simple linear saddle flow.

Example 4.1. *– Linear saddle flow.*
The saddle-point flow represents the simplest case of stable and unstable manifolds. The
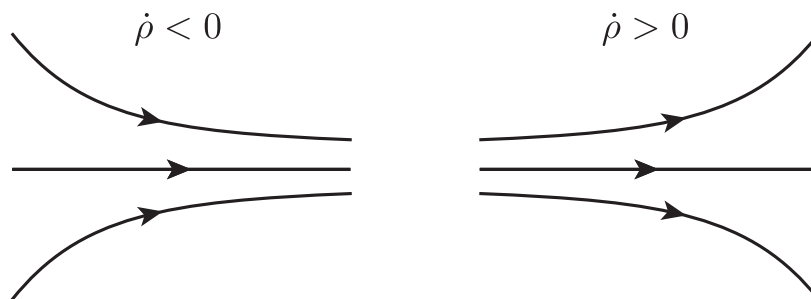
Figure 4.4: Schematic of the physical interpretation of the trajectory divergence rate $\dot{\rho}$. Negative values indicate converging trajectories while positive values indicate diverging trajectories.

system is given by

$$\dot{x} = x,$$
$$\dot{y} = -y. \tag{4.23}$$

As is visible in Figure 4.3, the linear saddle flow repels trajectories from the y-axis and attracts them to the x-axis in forward time.

The unit normal vector and rate-of-strain tensor are given by

$$\mathbf{n} = \frac{1}{\sqrt{x^2 + y^2}} \begin{bmatrix} y \\ x \end{bmatrix}, \quad \mathbf{S} = \begin{bmatrix} 1 & 0 \\ 0 & -1 \end{bmatrix}. \tag{4.24}$$

From these, the trajectory divergence rate is computed to be,

$$\dot{\rho} = \frac{y^2 - x^2}{x^2 + y^2}. \tag{4.25}$$

Figure 4.3 shows trajectories in phase space and the trajectory divergence rate of the linear saddle. From (4.25) and the trajectory divergence rate in the figure, trajectories are converging when $x^2 > y^2$ and diverging when $y^2 > x^2$. Trajectories are parallel where $y = \pm x$, as shown in white. The positive and negative ridges of the trajectory divergence rate field give the most repelling and attracting curves in the field: the vertical and horizontal axes, respectively. Interestingly, the forward and backward finite-time Lyapunov exponents are both uniform for the linear saddle flow, indicating no structure [28].

A similar quantity has been applied to the normal direction of a candidate Lagrangian coherent structure as a test of hyperbolicity, using gradients of the finite-time Lyapunov

exponent field to determine the tangent and normal directions [34]. The trajectory divergence rate, in contrast, uses the vector normal to trajectories of the dynamical system. From this observation, it is clear that the trajectory divergence rate gives the normal hyperbolicity field of the vector field.

4.3.3   Remarks on the trajectory divergence rate

(Lack of) objectivity of the trajectory divergence rate

The trajectory divergence rate (4.17) is not an objective quantity, as a scalar quantity such as $\dot{\rho}$ would be objective only if it remained unchanged under any translation and rotation of reference frame [27, 33]. In other words, objective scalar values remain invariant under transformations belonging to the Special Euclidean group $SE(n)$. Because the trajectory divergence rate depends on the tangent vectors, which are not objective, the quantity itself is not objective. However, as shown in the context of Lagrangian descriptors, objectivity is not always a desirable trait [29]. For the example of a rotating saddle flow, the finite-time Lyapunov exponent, which is an objective quantity, gives no structure at all. However, in that example, Lagrangian descriptors, which are not objective, are able to show the rotating saddle at every snapshot in time. Under situations where objectivity is necessary, the trajectory divergence rate may not be the appropriate tool to use. However, objectivity is not always a desirable property, and makes no sense in general abstract phase spaces.

Relationship to Objective Eulerian Coherent Structures

In their paper introducing objective Eulerian coherent structures [27], Serra and Haller introduce two objective quantities to calculate these structures: the stretching rate $\dot{p}$ and shear rate $\dot{q}$. These equations depend on the tangent vectors x' of a general curve γ parametrized by its arclength s.

$$\dot{p} = \frac{\langle x'(s), \mathbf{S}x'(s) \rangle}{\langle x'(s), x'(s) \rangle} \tag{4.26}$$

$$\dot{q} = \frac{\langle x'(s), (\mathbf{SR} - \mathbf{RS})\, x'(s) \rangle}{\langle x'(s), x'(s) \rangle} \tag{4.27}$$

These scalar functions are objective because they depend generally on $\mathbf{S}$, which is an objective tensor, and tangent vectors to a curve γ, which is not dependent on the vector field. If these

curves are restricted to trajectories following the vector field rather than general curves, then their tangent vectors become the vector field $x' = \mathbf{v}$, and $\dot{p}$ and $\dot{q}$ become quadratic forms on vectors $\mathbf{v}$ like the trajectory divergence rate and trajectory divergence ratio. However, they lose the objectivity that is central to the previous work. As discussed above, there are situations where objectivity is less important, so trajectory-based variations of the stretch rate $\dot{p}_v$ and shear rate $\dot{q}_v$ which depend on the vector field may prove useful. Considering the unit tangent vector $\mathbf{e} = \mathbf{v}/|\mathbf{v}|$, these are given by,

$$
\begin{aligned}
\dot{p}_v &= \langle \mathbf{e}, \mathbf{S}\mathbf{e} \rangle, \\
\dot{q}_v &= \langle \mathbf{e}, (\mathbf{SR} - \mathbf{RS})\,\mathbf{e} \rangle.
\end{aligned}
\tag{4.28}
$$

Together with the trajectory divergence rate introduced above, these three quadratic forms measure the instantaneous rates of tangential stretching, normal stretching, and shear of the vector field. The trajectory stretch rate $\dot{p}_v$ and trajectory shear rate $\dot{q}_v$ are worth further exploration in future studies.

On the other hand, removing the restriction of the trajectory divergence rate to trajectories of the vector field to instead calculate the normal repulsion of a general surface, the trajectory divergence rate becomes an objective scalar value just like the stretching and shear rates above.

From the stretch rate $\dot{p}$ criterion, the authors find that hyperbolic OECSs must contain isolated local minima or maxima of the eigenvalues of $\mathbf{S}$, s_1 and s_2, respectively.

4.4 Applications of the trajectory divergence rate

As a measure of normal attraction and repulsion of trajectories of a system, the trajectory divergence rate can be applied to a variety of special cases to identify influential structures in dynamical systems. It may serve as a good approximation for hyperbolic Lagrangian coherent structures or as a method to identify slow manifolds. Additionally, it may be relevant to calculate the normal hyperbolicity of a particular trajectory for applications in control.
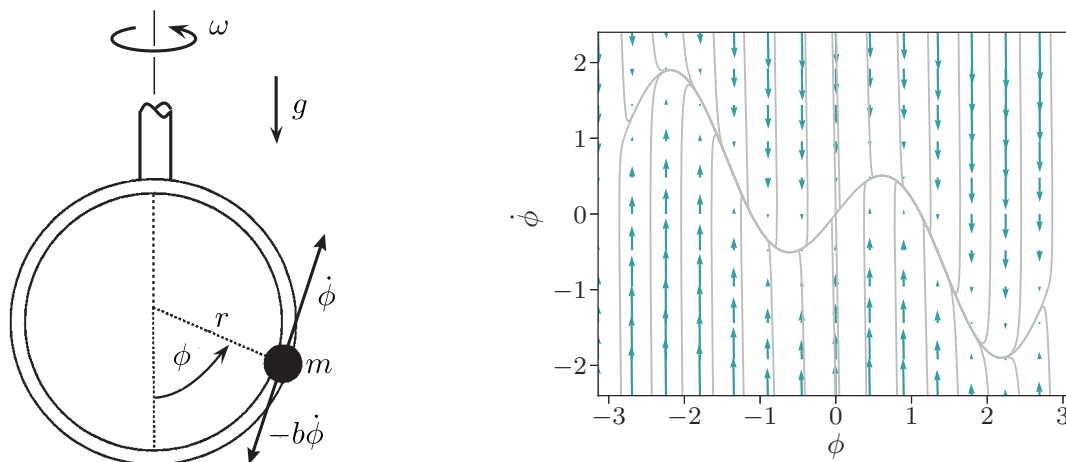
Figure 4.5: (Left) Schematic of an overdamped bead on a rotating hoop, Coulomb friction directly opposes the motion along the hoop, while the entire hoop rotates about the vertical axis with rotational velocity ω. (Right) The phase portrait for the model of Example 4.2 defined by (4.29), using $\varepsilon = 0.02$ and $\mu = 2.3$.

4.4.1 Approximation of slow manifolds and normally hyperbolic invariant manifolds

Given the interpretation of the trajectory divergence rate as a measure of normal hyperbolicity, it becomes a natural tool to identify normally hyperbolic invariant manifolds (NHIMs). One of the key examples of NHIMs is in the study of slow manifolds of multiple time scale systems [9]. In such systems there is a lower-dimensional manifold on which most of the dynamics occur, referred to as the slow manifold. This is typically conceptualized as an attracting manifold, but may be repelling in some cases. Outside of the slow manifold, the motion moves more quickly onto (or away from) the slow manifold.

Example 4.2. *–Overdamped bead on a rotating hoop.*
This example comes from Strogatz [35, Section 3.5], providing a nice example of a slow-fast system. The system conceptualizes a bead moving along a circular hoop of radius r while the hoop is spinning with constant angular velocity ω about a vertical axis. Considering a dimensionless time $T = \frac{b}{mg}$ and parameters $\mu = \frac{r\omega^2}{g}$ and $\varepsilon = \frac{m^2 gr}{b^2}$, the forces on the body reduce to the equations given by (4.29). When the damping coefficient b is large, the parameter ε becomes very small, and trajectories collapse quickly to the curve $\Omega = \sin\phi(\mu\cos\phi - 1)$ due to the high damping in the system, and then ooze along it toward one of several fixed points. This system is illustrated in Fig. 4.5.
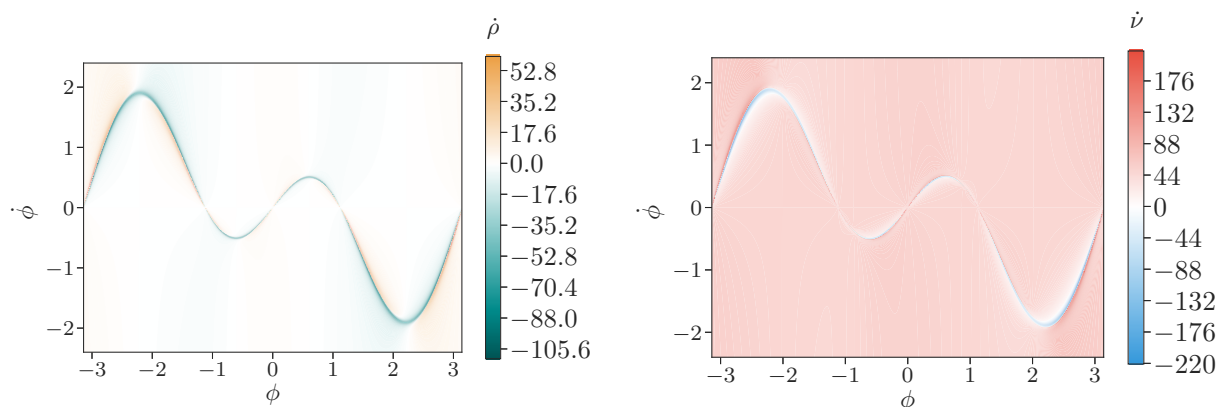
Figure 4.6: (left) The trajectory divergence rate and (right) the trajectory divergence ratio of Example 4.2 with $\varepsilon = 0.02$ and $\mu = 2.3$. These diagnostics both show strong attraction along the slow manifold visible above in Fig. 4.5.

$$
\begin{aligned}
\dot{\phi} &= \Omega \\
\dot{\Omega} &= \frac{1}{\varepsilon} \left(\sin\phi(\mu\cos\phi - 1) - \Omega \right)
\end{aligned}
\tag{4.29}
$$

For the parameters shown in Figs. 4.5 and 4.6, both $\phi = 0$, representing the bottom of the hoop, and $\phi = \pi$, representing the top of the hoop, give unstable fixed points, and a pair of fixed points on either side of the bottom of the hoop, at $\phi = \pm\arccos\frac{1}{\mu}$ become stable fixed points.

Figure 4.6 shows that the trajectory divergence rate is quite effective at capturing the slow manifold for this example. The red curve represents the attracting slow manifold onto which all trajectories converge. The trajectory divergence rate disappears near the equilibria of the system which are found each time the curve crosses the horizontal axis. As the trajectory divergence rate is calculated with normal vectors which are normalized by the magnitude of velocity, it is undefined at precisely the equilibria of the system.

Search for the curve which minimizes the trajectory divergence rate

The trajectory which minimizes the trajectory divergence rate may be identified as the most attractive invariant manifold in phase space. The arc-length averaged trajectory divergence
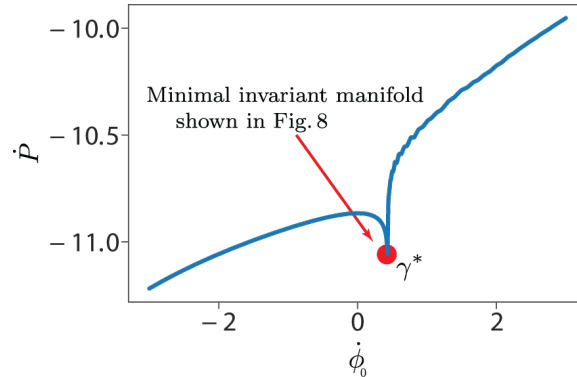
Figure 4.7: The arc-length averaged trajectory divergence rate $\dot{\rho}$ over 1,000 trajectories integrated both forward and backward along the vertical slice $\phi = -3$.

rate along a trajectory γ gives a way to identify this minimizing trajectory, defined by,

$$\dot{P} = \frac{1}{\sigma(\gamma)} \left(\int_\gamma \dot{\rho} ds \right), \tag{4.30}$$

where $\sigma(\gamma) = \int_\gamma ds$ is the arc length of γ.

Next, the arc-length averaged divergence rate $\dot{P}$ is minimized among a collection of trajectories Γ to find the minimizing trajectory γ^*,

$$\gamma^* = \min_{\gamma \in \Gamma} \dot{P}. \tag{4.31}$$

Fig. 4.7 shows the result of the calculation of arc-length averaged divergence rate for trajectories intersecting $\phi = -3$ over a range $\dot{\phi}_0 \in [-3, 3]$. These trajectories were integrated forward until they reached a fixed point and integrated backward until they reached $\dot{\phi} = \pm 11$. The results of this numerical minimization are shown in Fig. 4.8 by identifying the minimizing trajectory γ^* by its intersection with $\phi = -3$ by the red circle and showing its forward integration in red. This process is repeated for $\phi = -0.1$, and by symmetry, the values are obtained for $\phi = 0.1$ and $\phi = 3.0$.
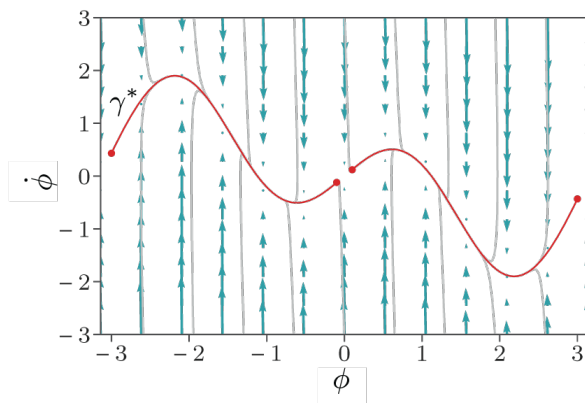
Figure 4.8: The results of the minimization of (4.31) as shown in Fig. 4.7. The red dot shows the minimum point found from the simulations, and the red curve shows the forward integration of this trajectory. Local minima were calculated at the points $\phi = \{-3.0, -0.1, 0.1, 3.0\}$ and integrated forward.
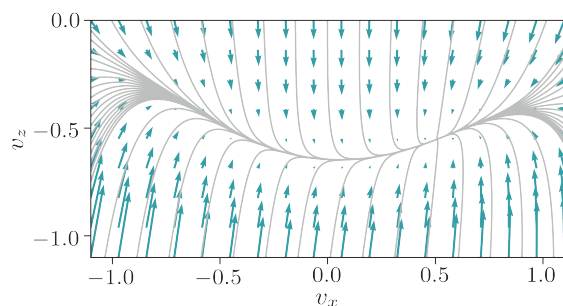
Figure 4.9: The phase portrait for Example 4.3, showing the weak unstable manifold passing through the origin.

Comparison with other methods

As an example of a situation where trajectory-restricted measurements are useful, consider the following example from [28], presented in the introduction of the trajectory-normal repulsion rate.

Example 4.3. – *The terminal velocity manifold in gliding flight.*
In a simplified model of passive gliding flight, a globally attracting codimension-one manifold may be observed in the glider's velocity space [3, 36]. Because every trajectory is rapidly attracted to this structure and evolves along or near it, it serves as a higher dimensional analogue to terminal velocity and is therefore referred to as the terminal velocity manifold.

The glider's motion under this model is given by the nondimensional equations of motion,

$$
\begin{aligned}
\dot{v}_x &= v^2 \left(C_L \left(\gamma + \theta \right) \sin \gamma - C_D \left(\gamma + \theta \right) \cos \gamma \right), \\
\dot{v}_z &= v^2 \left(C_L \left(\gamma + \theta \right) \cos \gamma + C_D \left(\gamma + \theta \right) \sin \gamma \right) - 1,
\end{aligned}
\tag{4.32}
$$

where $v_x = \frac{\epsilon}{gc} V_x$ and $v_z = \frac{\epsilon}{gc} V_z$ are the dimensionless horizontal and vertical components of velocity, θ is the body's fixed pitch angle with respect to the ground, $\gamma = \arctan \frac{-v_z}{v_x}$ is the angular direction of motion of the body, C_L and C_D represent lift and drag as functions of angle of attack $\gamma + \theta$, and derivatives are with respect to dimensionless time $t = \sqrt{c\epsilon/g}T$. The universal glide scaling parameter $\epsilon = \frac{\rho c S}{2m}$ included in these scalings allows for comparison of different gliders with the same equations [36]. Within these dimensionless variables are the horizontal and vertical velocity V_x, V_z, chord length c, glider span S, gravity g, time T, fluid density ρ, and mass m.

The phase portrait of this example for a falling flat plate with a fixed pitch of $\theta = -5°$ is shown in Fig. 4.9. From the stable fixed point located at $(v_x, v_z) = (0.50, -0.56)$, there are both strong and weak stable submanifolds within the . Because many invariant manifolds intersect the origin with the same tangent direction, the weak stable submanifold is nonunique, and methods such as the trajectory-normal repulsion rate may be used to identify the most influential weak stable submanifold [3, 28].

For this example, Fig. 4.10 presents the finite-time Lyapunov exponent σ_T, the trajectory-normal repulsion rate ρ_T, the largest eigenvalue of the rate-of-strain tensor $\mathbf{S}$ denoted by s_1, and the trajectory divergence rate $\dot{\rho}$ over the domain as a comparison of these methods. The finite-time Lyapunov exponent σ_T and eigenvalue of the rate-of-strain tensor s_1 both represent measures of pure stretching, and are therefore dominated by the tangential stretching. These measures both give no structure in the system. Hyperbolic objective Eulerian structures, as would be measured by s_1, must contain an isolated local maximum or minimum of s_1 [27], and no such isolated maximum or minimum exists in this example.

The two trajectory-based measures, on the other hand, both show the structure of the system, with the integrated measure of ρ_T giving a more defined ridge by taking into account longer time information.
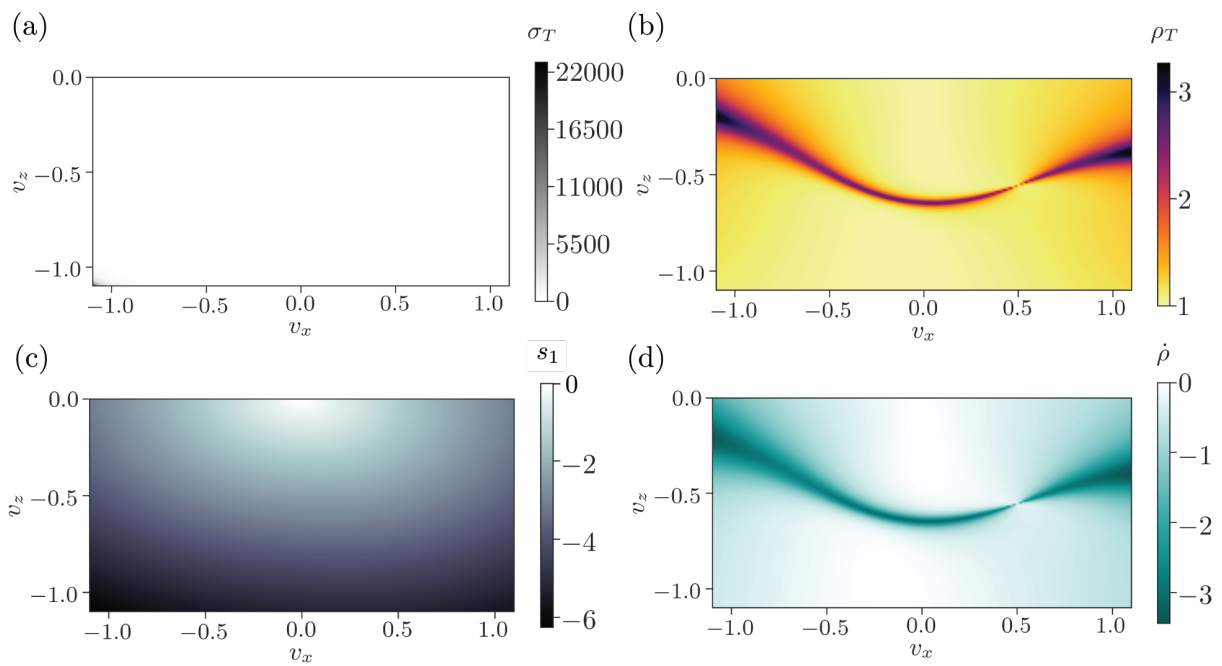
Figure 4.10: Comparison of methods to extract structure from Ex. 4.3. The scalar field calculations using (a) the finite-time Lyapunov exponent [12], (b) the trajectory-normal repulsion rate [28], (c) minimum eigenvalue of $\mathbf{S}$ from the objective Eulerian coherent structure approach [27], and (d) the trajectory divergence rate. Panels (a) and (b) were calculated by integrating trajectories with $T = -0.33$.
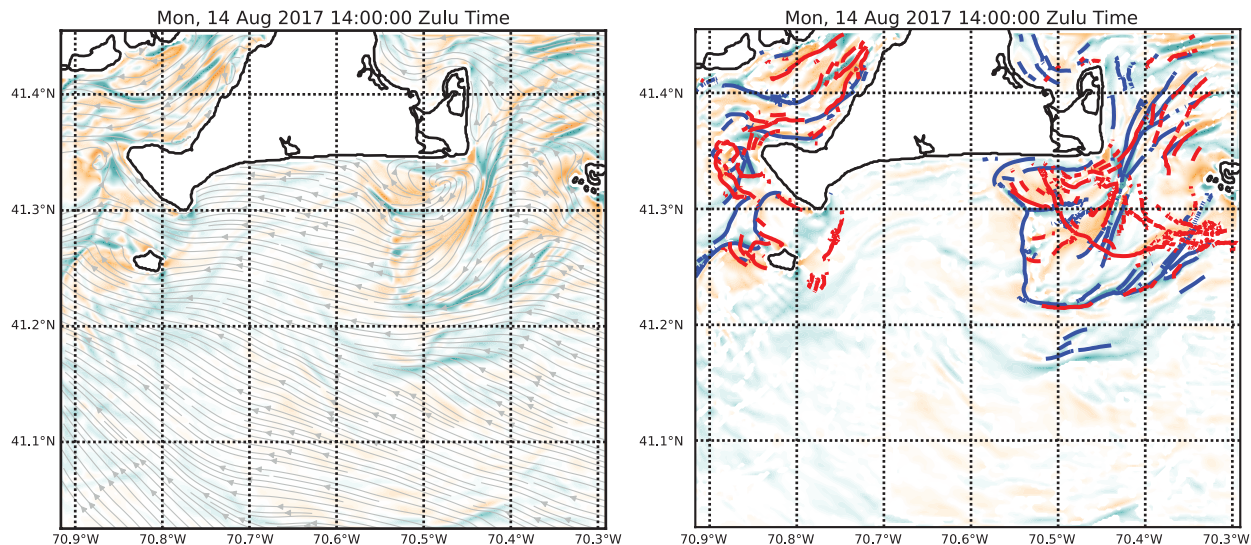
Figure 4.11: Simulation of ocean flow around Martha's Vineyard in August 2017 using the MSEAS model [38]. Streamlines of the ocean flow are shown in gray in the left figure. Lagrangian coherent structures calculated using C-ridges [39] for an integration time of 2 hours are shown as solid lines in the right figure, with attracting LCSs in blue and repelling LCSs in red. The trajectory divergence rate, shown in the background shows regions of attraction (cyan) and repulsion (orange). The inset figure shows the trajectory divergence rate $\dot{\rho}$ along 41.3°N latitude from 70.6°W to 70.3°W, marked by the points A and B. Intersecting attracting and repelling LCSs are shown with the blue and red vertical lines, respectively.

4.4.2   Approximation of hyperbolic Lagrangian coherent structures

As discussed in the introduction, in fluid flows, it can be very useful to look at finite-time barriers to transport in the fluid, known as Lagrangian coherent structures (LCSs) [12].

Two key limitations of many Lagrangian methods for detecting flow structures are the computation time for advecting trajectories [23, 24] and dealing with limited experimental data [37]. By considering an Eulerian (i.e., instantaneous) approximation of Lagrangian structures, the trajectory divergence rate can provide a first look at the structure of a given vector field. It may even be applied to nonautonomous flows to show the attraction and repulsion of the vector field at each time step. Although there may be exceptions [32], in most cases the short time transport barriers of a system are locally attracting or repelling. Therefore, the trajectory divergence rate may be used to approximate Lagrangian coherent structures.

Example 4.4. *–Data-driven ocean model.*
This example presents simulations in Fig. 4.11 of the ocean flow around Martha's Vineyard,

Massachusetts in August 2017 using the MIT-MSEAS primitive-equation ocean model [40]. With this simulation, it is possible to calculate trajectories of advected ocean flow to generate the flow map and therefore the right Cauchy Green tensor. The Lagrangian coherent structures are identified by calculating derivatives of the finite-time Lyapunov exponent in the largest eigendirection of the right Cauchy-Green tensor to find C-ridges [39]. These quantities are calculated over a forward or backward integration time of 2 hours for repelling and attracting features, respectively. In Fig. 4.11, it is clear that many of the LCSs align with regions of high repulsion or attraction and generally follow the ridges of these highly attracting or repulsive regions.

The trajectory divergence rate, because it measures normal growth of normal vectors, will be most aligned with the finite-time Lyapunov exponent, which measures maximum growth, when the direction of maximum growth occurs normal to a trajectory. In addition, because FTLE is a time-integrated measure, LCS will be most easily approximated by the trajectory divergence rate when the vector field is changing slowly relative to the dynamics.

Ridges and valleys of the trajectory divergence rate do not exactly correspond with hyperbolic LCSs, but they can serve as an approximation for a much lower computational cost. The trajectory divergence rate, for large geophysical fluid flows, can prove particularly helpful for identifying regions of interest in the flow quickly. This can be very important in search-and-rescue situations, or may be used as the first step in, for instance, an adaptive mesh algorithm to identify finite-time structures [41, 42].

4.4.3 Repulsion rate along a limit cycle

Because the trajectory divergence rate $\dot{\rho}$ gives the instantaneous attraction or repulsion of nearby trajectories, it can be applied to analyze the local stability of trajectories. For instance, it has been shown that globally attracting limit cycles may be locally repelling in places, which has significant implications for control [43, 44]. As an example, consider the classical Van der Pol oscillator.

Example 4.5. – *Van der Pol oscillator.*
The Van der Pol oscillator is another slow-fast system, but the folds along the slow manifold separate stable and unstable branches, which admit a so-called "canard explosion," leading to a limit cycle [9, 45]. The limit cycle is globally attracting, with two branches evolving
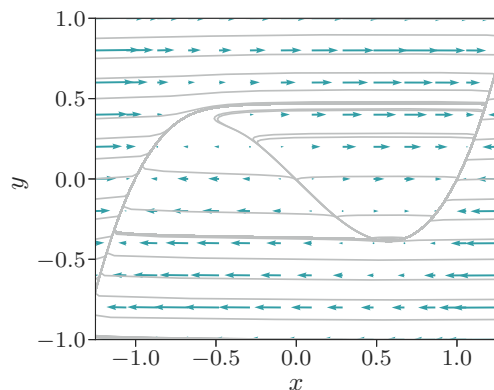
Figure 4.12: The phase portrait of the Van der Pol oscillator given by Example 4.5, using $\varepsilon = 0.01$ and $a = 0.575$.

along the slow manifold and the other two moving quickly across the system, as shown in Fig. 4.12.

The governing equations of the system are given by,

$$
\begin{aligned}
\dot{x} &= \frac{1}{\varepsilon}\left(y + x - x^3\right), \\
\dot{y} &= a - x,
\end{aligned}
\tag{4.33}
$$

with $0 < \varepsilon \ll 1$ and $a \in \mathbb{R}$. In this system, the slow dynamics occur along a slow manifold near $y = -x + x^3$, which is the critical manifold of the system. As the parameter a is increased from 0, the location of the fixed point changes until a Hopf bifurcation occurs, first forming a small limit cycle around the fold of the slow manifold before expanding to a loop around both fold points.

Several works have shown that although a limit cycle may be globally stable, it is not always locally stable [43, 44]. That is, there may be regions of a globally attracting limit cycle which are locally repelling. These regions may play a critical role in attempts to control dynamics which naturally occur in an oscillatory way, identifying the location along the limit cycle trajectory most sensitive to perturbation. The trajectory divergence rate along the trajectory, shown in Figure 4.13, provides an excellent tool for looking at this sensitivity to perturbation along a limit cycle. In this example it is applied to the Van der Pol oscillator of Example 4.5. The cycle is attracting for most of its space, but there are moments, when moving across the fold point to the opposite stable branch, when the trajectory is normally
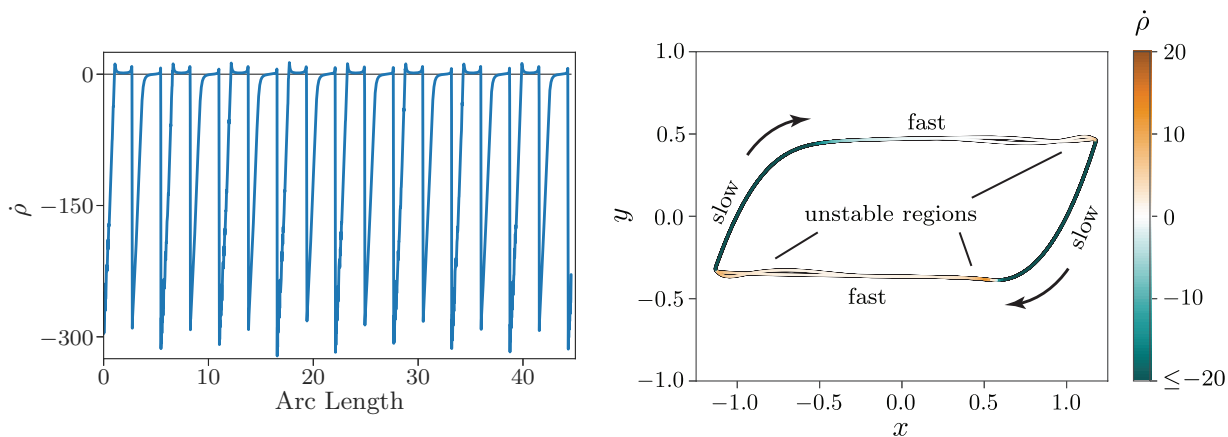
Figure 4.13: The trajectory divergence rate along the limit cycle in the Van der Pol oscillator of Example 4.5. Along the limit cycle, the outer branches along the slow manifold are very attractive, but the fast branches are instantaneously repelling.

repelling.

4.5   Extension to higher dimensions

With the intuition of the trajectory divergence rate in two dimensions, this method may be extended to higher dimensions. While the derivation used in Section 4.3 relies on the 2-dimensionality of the system, the understanding of the results. The two dimensional trajectory divergence rate calculates the normal projection of the instantaneous rate of deformation of the unique trajectory-normal vector $\dot{\rho} = \langle \mathbf{n}, \mathbf{Sn} \rangle$. In higher dimensions, trajectories remain one dimensional, so the normal direction becomes a normal hyperplane. Therefore, in higher dimensions, the normal projection of the instantaneous rate of deformation of the normal hyperplane, $\mathbf{N}$, may be written using the analogous formula,

$$\dot{\mathbf{R}} = \mathbf{N}^{\dagger}\mathbf{SN}. \tag{4.34}$$

In $\mathbb{R}^k$, $\mathbf{S}$ is the $k \times k$ rate-of-strain tensor, still given by $\mathbf{S} = \frac{1}{2}\left(\nabla\mathbf{v} + \nabla\mathbf{v}^{\dagger}\right)$ and $\mathbf{N}$ is the $k \times (k-1)$ matrix representing the hyperplane normal to the tangent vector $\mathbf{v}$. Therefore $\dot{R}$ will be of dimension $(k-1) \times (k-1)$. The eigenvalues of $\dot{R}$ give the principal trajectory divergence rates and the eigenvectors give the directions. The maximal eigenvalue of $\dot{R}$ gives the dominant attraction or repulsion of every point. The lower eigenvalues give the
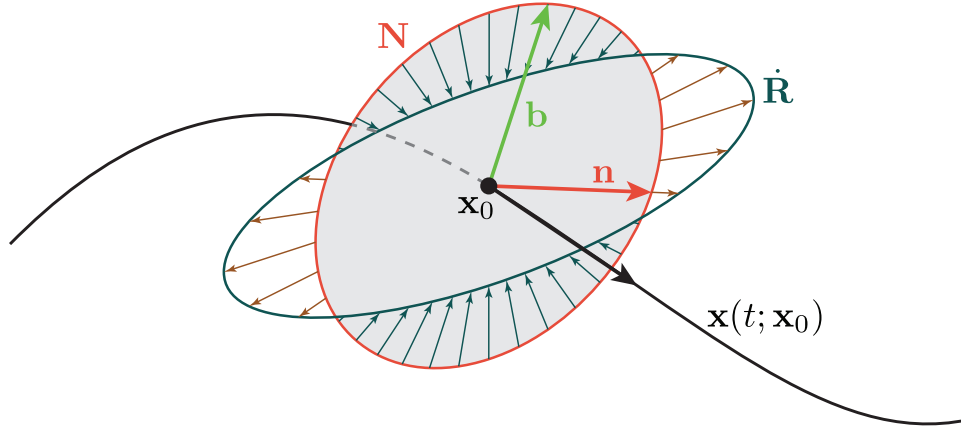
Figure 4.14: Representation of the divergence rate in a 3-dimensional system, $\dot{\mathbf{R}}$. The circle represents the normal plane N to the trajectory, and the ellipse represents the slope of normal stretching as in Fig. 4.2. The eigenvalues of $\dot{\mathbf{R}}$ give the principal stretching within the normal plane.

dimension of this attraction.

In 3 dimensions, the Frenet-Serret reference frame gives the normal plane to a trajectory γ with a tangent vector γ' and an acceleration γ''. In this frame, the normal plane is defined by two vectors: the normal $\mathbf{n}$ and binormal $\mathbf{b}$. The normal vector is defined to be in the direction of change of the tangent vector $\mathbf{e}$.

$$
\begin{aligned}
\mathbf{n} &= \frac{\frac{d\mathbf{e}}{ds}}{\left|\frac{d\mathbf{e}}{ds}\right|}, \\
\frac{d\mathbf{e}}{ds} &= \frac{\gamma' \times \gamma''}{|\gamma'|^3}.
\end{aligned}
\tag{4.35}
$$

The binormal, which must be perpendicular to both the tangent and normal vectors, can be found with their cross product,

$$
\mathbf{b} = \mathbf{e} \times \mathbf{n}.
\tag{4.36}
$$

The normal plane $\mathbf{N}$ is then defined by the normal and binormal unit vectors,

$$
\mathbf{N} = [\mathbf{n}, \, \mathbf{b}].
\tag{4.37}
$$
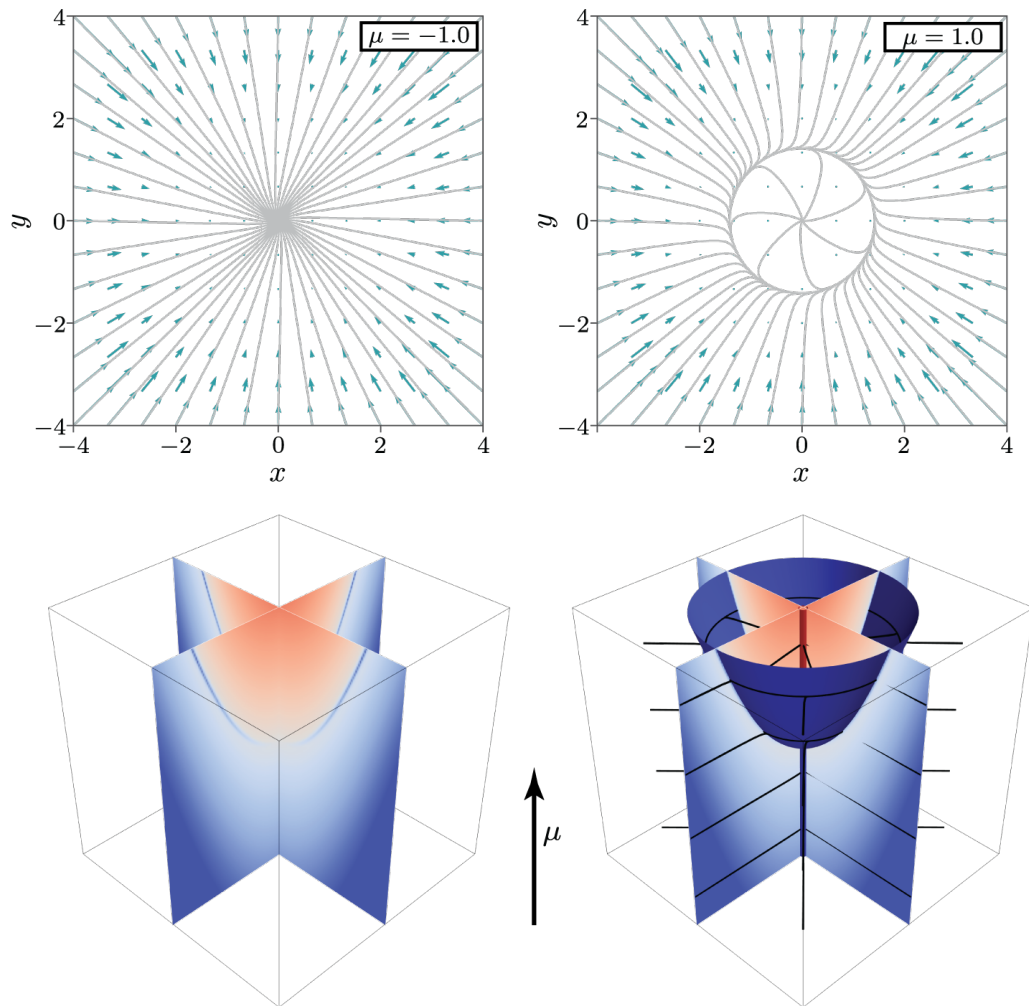
Figure 4.15: The phase portrait for Example 4.6 with $\mu = -1$ and $\mu = 1$, and results of the 3D computation of the trajectory divergence rate. In the bottom left, two slices of the largest eigenvalue of $\dot{\mathbf{R}}$ from Eq. (4.34) are shown for the Hopf bifurcation in extended phase space as described by (4.39), with $\epsilon = 0.25$. In the bottom right, this has been overlaid with the attracting manifold (blue) and example trajectories.

With this definition of the normal plane in 3 dimensions, (4.34) may be rewritten as,

$$\dot{R} = \begin{bmatrix} \langle \mathbf{n}, \mathbf{Sn} \rangle & \langle \mathbf{n}, \mathbf{Sb} \rangle \\ \langle \mathbf{b}, \mathbf{Sn} \rangle & \langle \mathbf{b}, \mathbf{Sb} \rangle \end{bmatrix}. \tag{4.38}$$

Calculating the higher-dimensional trajectory divergence rate of (4.34) shows the rates of stretching of the plane normal to each trajectory. Fig. 4.14 shows a visualization of this interpretation. There are an infinite number of vectors normal to the trajectory, so the higher-dimendsional trajectory divergence rate $\dot{\mathbf{R}}$ measures the rates of deformation of the entire plane, and eigenvalues of this matrix give the principal magnitudes and directions of repulsion and attraction.

Example 4.6. *–Supercritical Hopf bifurcation* .
The Poincaré-Andronov-Hopf, or simply Hopf, bifurcation is one of the most fundamental to nonlinear dynamics. As a parameter is increased, a single fixed point reverses its stability as a limit cycle appears. In parameter extended phase space, the Hopf bifurcation becomes a three-dimensional system, with the bifurcation parameter μ representing the third dimension [46], in which case the limit cycle is represented as a paraboloid. As an example of the application of the 3-dimensional trajectory divergence rate $\dot{\mathbf{R}}$ from Eq. (4.34), consider a slow-fast version of the Hopf normal form, with attraction to the limit cycle moving at a faster time scale than motion around the limit cycle. The parameter dynamics remain trivial.

$$\begin{aligned} \dot{x} &= \frac{1}{\epsilon} \left(2\mu - \left(x^2 + y^2 \right) \right) x - y, \\ \dot{y} &= \frac{1}{\epsilon} \left(2\mu - \left(x^2 + y^2 \right) \right) y + x, \\ \dot{\mu} &= 0. \end{aligned} \tag{4.39}$$

For a supercritical Hopf bifurcation, $\mu < 0$ corresponds with a single stable fixed point at the origin and $\mu > 0$ corresponds to an unstable fixed point at the origin with an attracting limit cycle of radius $\sqrt{2\mu}$.

Fig. 4.15 shows the phase space for this example for both $\mu = -1$, below the bifurcation, and $\mu = 1$, beyond the bifurcation point, showing the appearance of the limit cycle. Calculating the largest magnitude eigenvalue of the 3-dimensional repulsion rate $\dot{\mathbf{R}}$ shows the dominant attraction or repulsion at each point in extended parameter space. The panel shows the values along the (x, μ) and (y, mu) planes, to represent the 3-dimensional data. Particularly

of note is the narrow dark blue region in the top half of this panel, indicating the attracting limit cycle of the system. This method is unable to identify the attracting line which exists for $\mu < 0$, but is able to calculate the attracting paraboloid, and shows instability in the center of the paraboloid, with a peak closest to the center. This example shows promise for the future application of the trajectory divergence rate in higher dimensions.

4.6 Summary and conclusions

The trajectory divergence rate is an inherent property of continuously differentiable vector fields that naturally follows from either the instantaneous stretching of vectors or the trajectory-normal repulsion rate. It measures the rate at which the normal distance between nearby trajectories grows at every position in the domain of the vector field. It is a straightforward quantity to compute, requiring only the instantaneous vector field and its derivatives, and therefore may provide a useful diagnostic when investigating the geometric properties of a flow.

In application, the trajectory divergence rate and divergence ratio may be applied to approximate slow manifolds, weak stable or unstable manifolds, or hyperbolic Lagrangian coherent structures, or to measure the local stability of trajectories such as limit cycles.

The trajectory divergence rate and ratio are computationally efficient and physically intuitive. These scalar fields may become useful tools for the investigation of many applications in various fields. The python package ManifoldID for manifold identification, developed for this paper, may be found on GitHub at
https://github.com/gknave/manifoldid.

Bibliography

[1] David G. Schmale III and Shane D. Ross. Highways in the sky: Scales of atmospheric transport of plant pathogens. *Annual Review of Phytopathology*, 53:591–611, 2015.

[2] Jifeng Peng and John O Dabiri. The 'upstream wake' of swimming and flying animals and its correlation with propulsive efficiency. *Journal of Experimental Biology*, 211(16): 2669–2677, 2008.

[3] Gary K Nave Jr and Shane D Ross. Global phase space structures in a model of passive descent. *Under review, arXiv Preprint arXiv:1804.05099*, 2018.

[4] Emilie Tew Kai, Vincent Rossi, Joel Sudre, Henri Weimerskirch, Cristobal Lopez, Emilio Hernandez-Garcia, Francis Marsac, and Veronique Garçon. Top marine predators track lagrangian coherent structures. *Proceedings of the National Academy of Sciences*, 106 (20):8245–8250, 2009.

[5] Francois Lekien, Chad Coulliette, Arthur J Mariano, Edward H Ryan, Lynn K Shay, George Haller, and Jerry Marsden. Pollution release tied to invariant manifolds: A case study for the coast of Florida. *Physica D: Nonlinear Phenomena*, 210(1-2):1–20, 2005.

[6] Stephen Wiggins. The dynamical systems approach to lagrangian transport in oceanic flows. *Annual Review of Fluid Mechanics*, 37:295–328, 2005.

[7] Jun Zhong, Lawrence N Virgin, and Shane D Ross. A tube dynamics perspective governing stability transitions: An example based on snap-through buckling. *International Journal of Mechanical Sciences*, 2017.

[8] Wang Sang Koon, Martin W Lo, Jerrold E Marsden, and Shane D. Ross. *Dynamical systems, the three-body problem and space mission design*. Citeseer, 2008.

[9] Christian Kuehn. *Multiple time scale dynamics*, volume 1. Springer, 2016.

[10] Stephen Wiggins. *Normally hyperbolic invariant manifolds in dynamical systems*, volume 105. Springer Science & Business Media, 2013.

[11] JA Jiménez Madrid and Ana M Mancho. Distinguished trajectories in time dependent vector fields. *Chaos: An Interdisciplinary Journal of Nonlinear Science*, 19(1):013111, 2009.

[12] Shawn C. Shadden, Francois Lekien, and Jerrold E. Marsden. Definition and properties of lagrangian coherent structures from finite-time lyapunov exponents in two-dimensional aperiodic flows. *Physica D: Nonlinear Phenomena*, 212(3):271–304, 2005.

[13] Shawn C Shadden. Lagrangian coherent structures. *Transport and Mixing in Laminar Flows: From Microfluidics to Oceanic Currents*, pages 59–89, 2011.

[14] Bree B Aldridge, George Haller, Peter K Sorger, and Douglas A Lauffenburger. Direct lyapunov exponent analysis enables parametric study of transient signalling governing cell behaviour. *IEE Proceedings-Systems Biology*, 153(6):425–432, 2006.

[15] Evan S Gawlik, Jerrold E Marsden, Philip C Du Toit, and Stefano Campagnola. Lagrangian coherent structures in the planar elliptic restricted three-body problem. *Celestial Mechanics and Dynamical Astronomy*, 103(3):227–249, 2009.

[16] Martin L Tanaka, Shane D Ross, and Maury A Nussbaum. Mathematical modeling and simulation of seated stability. *Journal of Biomechanics*, 43(5):906–912, 2010.

[17] Sanjeeva Balasuriya, Nicholas T Ouellette, and Irina I Rypina. Generalized lagrangian coherent structures. *Physica D: Nonlinear Phenomena*, 2018.

[18] Michael Dellnitz, Gary Froyland, and Oliver Junge. The algorithms behind gaioset oriented numerical methods for dynamical systems. In *Ergodic Theory, Analysis, and Efficient Simulation of Dynamical Systems*, pages 145–174. Springer, 2001.

[19] Gary Froyland and Kathrin Padberg-Gehle. A rough-and-ready cluster-based approach for extracting finite-time coherent sets from sparse and incomplete trajectory data. *Chaos: An Interdisciplinary Journal of Nonlinear Science*, 25(8):087406, 2015.

[20] Michael R Allshouse and Jean-Luc Thiffeault. Detecting coherent structures using braids. *Physica D: Nonlinear Phenomena*, 241(2):95–105, 2012.

[21] Marko Budišić and Jean-Luc Thiffeault. Finite-time braiding exponents. *Chaos: An Interdisciplinary Journal of Nonlinear Science*, 25(8):087407, 2015.

[22] Alireza Hadjighasem, Mohammad Farazmand, Daniel Blazevski, Gary Froyland, and George Haller. A critical comparison of lagrangian methods for coherent structure detection. *Chaos: An Interdisciplinary Journal of Nonlinear Science*, 27(5):053104, 2017.

[23] Siavash Ameli, Yogin Desai, and Shawn C Shadden. Development of an efficient and flexible pipeline for lagrangian coherent structure computation. In *Topological Methods in Data Analysis and Visualization III*, pages 201–215. Springer, 2014.

[24] Steven L Brunton and Clarence W Rowley. Fast computation of finite-time lyapunov exponent fields for unsteady flows. *Chaos: An Interdisciplinary Journal of Nonlinear Science*, 20(1):017503, 2010.

[25] George Haller and Themistoklis Sapsis. Localized instability and attraction along invariant manifolds. *SIAM Journal on Applied Dynamical Systems*, 9(2):611–633, 2010.

[26] Pinaki Chakraborty, S Balachandar, and Ronald J Adrian. On the relationships between local vortex identification schemes. *Journal of Fluid Mechanics*, 535:189–214, 2005.

[27] Mattia Serra and George Haller. Objective Eulerian coherent structures. *Chaos: An Interdisciplinary Journal of Nonlinear Science*, 26(5):053110, 2016.

[28] George Haller. A variational theory of hyperbolic Lagrangian coherent structures. *Physica D: Nonlinear Phenomena*, 240(7):574–598, 2011.

[29] Carlos Lopesino, Francisco Balibrea-Iniesta, Víctor J García-Garrido, Stephen Wiggins, and Ana M Mancho. A theoretical framework for lagrangian descriptors. *International Journal of Bifurcation and Chaos*, 27(01):1730001, 2017.

[30] George Haller. Lagrangian structures and the rate of strain in a partition of two-dimensional turbulence. *Physics of Fluids*, 13(11):3365–3385, 2001.

[31] Mathieu Desroches and Mike R Jeffrey. Canards and curvature: the 'smallness of ε' in slow–fast dynamics. In *Proceedings of the Royal Society of London A: Mathematical, Physical and Engineering Sciences*, page rspa20110053. The Royal Society, 2011.

[32] Phanindra Tallapragada and Senbagaraman Sudarsanam. A globally stable attractor that is locally unstable everywhere. *AIP Advances*, 7(12):125012, 2017.

[33] Clifford Truesdell and Walter Noll. *The non-linear field theories of mechanics*. Springer, 2004.

[34] Melissa A Green, Clarence W Rowley, and Alexander J Smits. Using hyperbolic lagrangian coherent structures to investigate vortices in bioinspired fluid flows. *Chaos: An Interdisciplinary Journal of Nonlinear Science*, 20(1):017510, 2010.

[35] Steven H. Strogatz. *Nonlinear dynamics and chaos: with applications to physics, biology, chemistry, and engineering*. Westview Press, 2014.

[36] Isaac J. Yeaton, John J. Socha, and Shane D. Ross. Global dynamics of non-equilibrium gliding in animals. *Bioinspiration & Biomimetics*, 12(2):026013, 2017.

[37] Christoph Garth, Florian Gerhardt, Xavier Tricoche, and Hagen Hans. Efficient computation and visualization of coherent structures in fluid flow applications. *IEEE Transactions on Visualization and Computer Graphics*, 13(6):1464–1471, 2007.

[38] Michela De Dominicis, Silvia Falchetti, Francesco Trotta, Nadia Pinardi, Luca Giacomelli, Ernesto Napolitano, Leopoldo Fazioli, Roberto Sorgente, Patrick J Haley Jr, Pierre FJ Lermusiaux, et al. A relocatable ocean model in support of environmental emergencies. *Ocean Dynamics*, 64(5):667–688, 2014.

[39] Benjamin Schindler, Ronald Peikert, Raphael Fuchs, and Holger Theisel. Ridge concepts for the visualization of lagrangian coherent structures. In *Topological Methods in Data Analysis and Visualization II*, pages 221–235. Springer, 2012.

[40] Patrick J Haley and Pierre FJ Lermusiaux. Multiscale two-way embedding schemes for free-surface primitive equations in the "multidisciplinary simulation, estimation and assimilation system". *Ocean Dynamics*, 60(6):1497–1537, 2010.

[41] Francois Lekien and Shane D Ross. The computation of finite-time lyapunov exponents on unstructured meshes and for non-euclidean manifolds. *Chaos: An Interdisciplinary Journal of Nonlinear Science*, 20(1):017505, 2010.

[42] X Xie, PJ Nolan, SD Ross, and T Iliescu. Lagrangian data-driven reduced order modeling of finite time lyapunov exponents. *Under Review*, 2018.

[43] Fathei Ali and Michael Menzinger. On the local stability of limit cycles. *Chaos: An Interdisciplinary Journal of Nonlinear Science*, 9(2):348–356, 1999.

[44] James A Norris, Anthony P Marsh, Kevin P Granata, and Shane D Ross. Revisiting the stability of 2d passive biped walking: local behavior. *Physica D: Nonlinear Phenomena*, 237(23):3038–3045, 2008.

[45] Martin Krupa and Peter Szmolyan. Relaxation oscillation and canard explosion. *Journal of Differential Equations*, 174(2):312–368, 2001.

[46] Stephen Wiggins. *Introduction to applied nonlinear dynamical systems and chaos*, volume 2. Springer Science & Business Media, 2003.

4.7 Derivation of Equation (4.17)

Starting with (4.15), the trajectory-normal repulsion rate, ρ_T can be written, to leading order in T, as,

$$
\begin{aligned}
\rho_T &= 1 + \left(\text{tr}(\mathbf{S}) - \frac{\mathbf{v}^\dagger \mathbf{S} \mathbf{v}}{|\mathbf{v}|^2} \right) T \\
&= 1 + \frac{1}{|\mathbf{v}|^2} (\text{tr}(\mathbf{S}) |\mathbf{v}|^2 - \mathbf{v}^\dagger \mathbf{S} \mathbf{v}) T \\
&= 1 + \frac{\mathbf{v}^\dagger (\text{tr}(\mathbf{S})\mathbf{I} - \mathbf{S}) \mathbf{v}}{|\mathbf{v}|^2} T
\end{aligned}
\tag{4.40}
$$

For a 2-tensor, $\mathbf{A}$, the relation $\text{tr}(\mathbf{A})\mathbf{I} - \mathbf{A}$ in index notation may be written as $A_{ii}\delta_{jk} - A_{jk}$.

$$
\begin{aligned}
\text{tr}(\mathbf{A})\mathbf{I} - \mathbf{A} &= A_{ii}\delta_{jk} - A_{jk} \\
&= A_{il}\delta_{li}\delta_{jk} - A_{il}\delta_{lk}\delta_{ji} \\
&= A_{il}(\delta_{li}\delta_{jk} - \delta_{lk}\delta_{ji}) \\
&= A_{il}\varepsilon_{lj}\varepsilon_{ik} \\
&= \mathbf{R}^\dagger \mathbf{A} \mathbf{R}
\end{aligned}
\tag{4.41}
$$

Where ε_{ij} is the 2-dimensional Levi-Cevita symbol which, for a 2x2 matrix, is the index representation of the negative of the 90° counter-clockwise rotation matrix, $\varepsilon_{ij} = -\mathbf{R}$. Therefore,

for small time T, ρ_T may be written as,

$$
\begin{aligned}
\rho_T &= 1 + \frac{\mathbf{v}^\dagger (\mathbf{R}^\dagger \mathbf{S} \mathbf{R}) \mathbf{v}}{|\mathbf{v}|^2} T \\
&= 1 + \frac{(\mathbf{R} \mathbf{v})^\dagger \mathbf{S} (\mathbf{R} \mathbf{v})}{|\mathbf{v}|^2} T
\end{aligned}
\tag{4.42}
$$

Which can alternatively be written in terms of the unit normal field, $\mathbf{n} = \mathbf{R} \mathbf{v} / |\mathbf{v}|$, as in (4.3), yielding

$$
\rho_T = 1 + \langle \mathbf{n}, \mathbf{S} \mathbf{n} \rangle T
\tag{4.43}
$$

which gives us that the leading order behavior is defined by the instantaneous rate,

$$
\dot{\rho} = \langle \mathbf{n}, \mathbf{S} \mathbf{n} \rangle
\tag{4.44}
$$

Note that the rate of length change for an infinitesimal material element vector ℓ based at $\mathbf{x}_0$ and advected under the flow is

$$
\frac{d}{dt} |\ell| = \frac{1}{|\ell|} \langle \ell, \mathbf{S} \ell \rangle
\tag{4.45}
$$

Thus, the leading order behavior of the trajectory-normal repulsion rate for short time T can be thought of as the rate of stretching of unit normal vectors, normal to the invariant manifold passing through $\mathbf{x}_0$. This value is locally maximized along the most repulsive (or attractive) manifolds, which provide the most influential core of phase space deformation patterns.

Chapter 5

Summary and conclusions

The purpose of the research presented in this dissertation, through all three manuscripts, is to provide numerical tools and methods for future application. Using existing quasi-steady fluid force data, theoretical insights, and computational methods on vector fields, I have developed an updated fluid force model, frameworks with which to compare systems with fluid forcing, and introduced a new diagnostic to help understand the geometry of both fluid flows and mathematical models. The research presented in this dissertation may have applications to a wide variety of fields and research problems.

In Chapter 2, I extend the idea of wake stiffness [1] to incorporate nonlinear effects, provide a new model for quasi-steady forces induced by a bluff body wake that takes into account the critical spacing of a body in the wake, and conducted kinematic experiments on a novel cylinders configuration to apply the idea of nonlinear wake stiffness. This framework generalizes wake stiffness to consider configurations beyond solely transversely oscillating tandem cylinders. The extension of the quasi-analytical model of Blevins [2] to incorporate fluid forces below the critical spacing between cylinders reduces the mean squared error of the best previous model by 67%. In this model, we present both a piecewise model for the two branches of the hysteresis in critical spacing and a smoothed model for use when the critical spacing is unknown for the application. Experiments confirm that the combined use of lift and drag expansions provide a good approximation for new systems, and that gap flow switching can lead to larger amplitude, more consistent oscillations than wake-induced vibration. The models developed in this section can be applied to prevent clashing of offshore oil pipes and to predict energy harvesting capabilities of wake oscillator devices.

In Chapter 3, I built on the work of Yeaton et al. [3] to find rigorous calculation and analysis of the terminal velocity manifold in models of passive gliding flight. We were able to describe the manifold as the collection of weak unstable manifolds of the stable fixed points of the systems, and show that a fixed point is guaranteed in the system. We compared several methods to rigorously calculate the terminal velocity manifold, and, finally, expanded the terminal velocity manifold to a 2D manifold embedded in a 3-dimensional space, using the body's fixed angle with respect to the ground. This work provides a platform with which to compare the glide capabilities of different animals. Because this model relies solely on quasi-steady translational forces, experimental deviations from the expected higher dimensional terminal velocity manifold can show to what extent rotational forces and shape changes are used in an animal's glide. Thinking of gliding in terms of a terminal velocity manifold may also prove useful in the context of controlling engineered gliders. By changing an airfoil shape to control lift and drag as functions of angle-of-attack and, therefore, to control the properties and shape of the terminal velocity manifold, the glider performance can be optimized.

In Chapter 4, I develop a new diagnostic for identifying attracting and repelling manifolds such as the one discussed in Chapter 3 known as the trajectory divergence rate. This scalar field may be derived from the trajectory-normal repulsion rate [4], and gives a measurement for the instantaneous growth of the normal distance between nearby trajectories. This technique may prove very useful in experimental and field applications of coherent structure detection. This and other techniques have been included in a software package freely available on GitHub at https://github.com/gknave/manifoldid.

5.1 Future research directions

The work of this dissertation ends up raising as many questions as it answers. From this work, I would suggest several possible future research directions:

The framework of nonlinear wake stiffness and extended model for wake forcing developed in Chapter 2 leaves the door open to future research directions. This work focused primarily on the development of the model, but hasn't focused much on its application beyond the tethered cylinders. For example, the conditions for clashing between tandem cylinders may be calculated as in [2, 5], helping to prevent damage to offshore oil risers. In collaboration with Wenchao Yang, planned future work also includes investigating the very low Reynolds

number limit of nonlinear wake stiffness through quasi-2D, soap film experiments [6].

The work of Chapter 3 raises many questions about attracting manifolds and animal gliding. The most pressing future direction of this work is to compare experimental research results of animal glides with the predicted terminal velocity manifold for that animal. How closely does the animal's glide follow the 3D terminal velocity manifold? How closely does the animal's glide follow an optimal control strategy based on the perspective of the terminal velocity manifold? Such a study has been proposed in collaboration with Ty Hetrick and Pranav Khandelwal at UNC Chapel Hill, based on the glide performance of the flying lizard, *Draco dussumieri*. Another interesting question is that of controlling the lift and drag functions by changing shape in order to control the terminal velocity manifold. Such a question could be approached with the framework of manipulating flow barriers [7], and a project related to this idea has been discussed with Sanjeeva Balasuriya at the University of Adelaide.

Finally, the development of the trajectory divergence rate in Chapter 4 naturally lends itself to future application of the divergence rate to finding structure. Using the instantaneous metric to rapidly develop a mesh for the simulation of trajectories, for example, could provide a simple way to improve the accuracy of finite-time methods without adding much computational time. In addition, as demonstrated by Figure 4.7, a variational principle may be able to calculate precisely the trajectory which maximizes (or minimizes) the instantaneous repulsion of the system. Lastly, the refinement and application of the higher dimensional approach introduced in Sec. 4.5 could prove very fruitful, allowing for the rapid calculation of lower dimensional manifolds in large parameter spaces.

Bibliography

[1] G. R. S. Assi, P. W. Bearman, B. S. Carmo, J. R. Meneghini, S. J. Sherwin, and R. H. J. Willden. The role of wake stiffness on the wake-induced vibration of the downstream cylinder of a tandem pair. *Journal of Fluid Mechanics*, 718:210–245, 2013.

[2] Robert D. Blevins. Forces on and Stability of a Cylinder in a Wake. *Journal of Offshore Mechanics and Arctic Engineering*, 127(1):39–45, March 2005. ISSN 0892-7219. doi: 10.1115/1.1854697.

[3] Isaac J. Yeaton, John J. Socha, and Shane D. Ross. Global dynamics of non-equilibrium gliding in animals. *Bioinspiration & Biomimetics*, 12(2):026013, 2017.

[4] George Haller. A variational theory of hyperbolic Lagrangian coherent structures. *Physica D: Nonlinear Phenomena*, 240(7):574–598, 2011.

[5] Erling Huse et al. Interaction in deep-sea riser arrays. In *Offshore Technology Conference*. Offshore Technology Conference, 1993.

[6] Wenchao Yang and Mark A. Stremler. Critical spacing of stationary tandem circular cylinders at $Re \approx 100$. *In preperation*, 2018.

[7] Sanjeeva Balasuriya. Unsteadily manipulating internal flow barriers. *Journal of Fluid Mechanics*, 818:382–406, 2017.

Appendices

Appendix A

Wake stiffness and its application: oscillating cylinders and flying snakes

Abstract

Wake stiffness is the tendency of the wake of an upstream body to pull a downstream body toward the centerline. In this presentation, we will discuss the validity of applying the wake stiffness model to the dynamics of a tethered pair of cylinders in a uniform flow. We find that wake stiffness provides a good simplified model for cylinders, but does not explain the whole behavior, particularly with cylinder spacings above 3.5 diameters. We will also explore the extension of the wake stiffness concept to modeling the underlying mechanics of flying snakes.

Attribution

This appendix presents the extended abstract for a conference presentation

A.1 Wake stiffness in the motion of tandem, tethered cylinders

When considering cylinder oscillations in the wake of an upstream cylinder submerged in a uniform flow, several researchers have found that oscillations persist and even amplify beyond the lock-in region for single cylinders in a flow [1][2]. Assi et al. [3] have proposed an explanation for the effect of the upstream wake that they refer to as "wake stiffness". They demonstrate in their experimental system that the wake of the upstream cylinder acts as a linear spring, pulling the downstream cylinder toward the centerline of the wake.

To understand the behavior of tandem bluff bodies and investigate this concept of wake stiffness, we have focused our experimental efforts on investigating tandem circular cylinders. Using a free surface water channel at Virginia Tech, we have conducted experiments over a range of cylinder spacings, $x_0/D \in [3.0, 5.0]$, and a range of Reynolds numbers, $Re \in (4 \times 10^3, 1.1 \times 10^4)$. In our experiments, the upstream cylinder is fixed and the trailing cylinder is tethered to this fixed cylinder; that is, the downstream cylinder is constrained to move along a circular path around the upstream cylinder, as shown in Figure 1(a). The trailing cylinder is displaced to angular amplitudes, θ_{max}, between 10° and 25°, giving a nearly transverse cylinder motion. Since the majority of the literature considers transverse oscillations [3][1][2], we will compare with such experiments.

In their investigations of wake induced vibration of tandem cylinders, Assi et al. [3] conducted experiments on a fixed upstream cylinder with a transversely constrained downstream cylinder on air bearings. They found that steady oscillations of the trailing cylinder persisted when they removed the structural restoring force from their experiments, and they introduce wake stiffness to explain the frequency of oscillations that they measure. As the cylinder is displaced from the wake centerline, the average magnitude of the coefficient of lift increases, giving the overall wake a stiffness-like behavior for quasi-steady dynamics. The wake stiffness is generated by the mean pressure difference between the surrounding flow and passing vortices shed from the upstream cylinder, providing an approximately linear dependence on displacement.

Since our experiments have no structural restoring force, any forces on the cylinders are due solely to fluid forces. For cylinder separations of 3.5 to 5 diameters, the power spectrum of cylinder motion is dominated by two frequencies: a lower power, higher frequency component

consistent with the corresponding Strouhal frequency for a stationary cylinder at that flow velocity; and a higher power, lower frequency component that we associate with the wake stiffness, as shown in Figure 1(c). When $x_0/D = 3$, the power spectrum shows one frequency peak. Based on results from the literature [4], this behavior lies within the little-studied gap-flow switching regime for tandem cylinders, which occurs over $x_0/D < 3.5$ according to [4]. As the trailing cylinder is displaced, flow around the cylinders is redirected through the gap, causing the cylinder to be forced back toward the centerline. Assi et al. [3] did not conduct experiments in the gap-flow switching regime.

In the present study, we non-dimensionalize the measured frequency of oscillation by flow velocity and diameter in order to calculate an apparent wake stiffness, which we define as the stiffness necessary to give the measured frequency. Our experimental results support the use of the wake stiffness model in our tethered cylinder system. Figure 1(d) shows that apparent wake stiffness decreases slightly as Reynolds number increases for all cases within the wake induced vibration regime for which Assi et al. [3] initially postulated wake stiffness; this decreasing relative frequency is also shown in the original paper. In contrast, in the gap-flow switching regime the apparent wake stiffness remains essentially constant throughout the tested range, suggesting that the wake stiffness model is even more applicable to this regime than to the parameter range proposed in [3].

A.2 Applying wake stiffness to a model of flying snakes

There are five species of arboreal snakes native to Southeast Asia, most notably *Chrysopelea ornata*, which are able to flatten their bodies into a symmetric airfoil-like shape and glide through the air. They continue to undulate their bodies throughout the flight much as snakes do on the ground, leading to complex mechanics. The flow structure around their bodies is unknown, but Holden et al. [5] have investigated the forces on a representative cross-sectional body shape and have found that the cross-section is a bluff body with a vortex wake at every angle of attack.

In the investigation of flying snakes, work has been done to represent the essential components of the mechanics of gliding in simplified models. One such model, developed by Jafari et al. [6], uses the mean lift and drag forces on the snake airfoil shape from experiments by Holden et al. [5] to influence a tandem wing model. A schematic of the tandem wing model

is shown in Figure 1(b) to highlight the similarities with the tandem cylinder configuration. Each wing represents an approximately straight segment of the snake that is transverse to the incoming flow. These wings are considered as rigidly connected, aerodynamically decoupled bodies. Each wing is a bluff body at any angle of attack. Therefore, we assume that we can apply the concept of wake stiffness to the model, and thereby achieve a first order improvement over the initial model. We will discuss the effect of wake stiffness on glide stability and distance for the tandem wing model of the snake.

A.3   Conclusions

This talk will focus on the concept of wake stiffness, first introduced by Assi et al.[3]. We will discuss our findings regarding the validity of this concept through our own experiments on tandem cylinders in a different configuration. We will also explore the implications of extending the wake stiffness model to a non-circular pair of bluff bodies, such as the cross-sectional body shape of flying snakes.
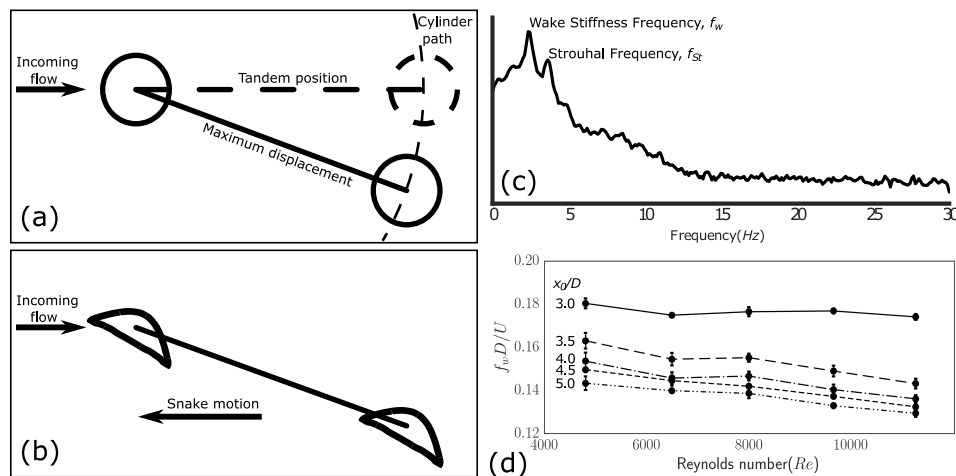
Figure A.1: (a) Configuration of the tandem, tethered cylinder system. The trailing cylinder is constrained to move around the upstream cylinder along the "cylinder path." (b) Schematic of tandem wing model of flying snakes. The wings move together and are constrained to a constant distance, giving the similarity to tethered cylinders. (c) PSD of dynamic response for cylinder spacing $x_0/D = 4$, showing frequency peaks corresponding to Strouhal frequency and wake stiffness frequency. (d) Apparent Wake Stiffness, $f_w D/U$, for tandem, tethered cylinders at various spacings. The figure shows that wake stiffness effects decrease for $x_0/D \geq 3.5$, but remain constant for $x_0/D = 3.0$.

Bibliography

[1] G. R. S. Assi, P. W. Bearman, and J. R. Meneghini. On the wake-induced vibration of tandem circular cylinders: the vortex interaction excitation mechanism. *Journal of Fluid Mechanics*, 661:365–401, 2010. doi: 10.1017/S0022112010003095.

[2] F. S. Hover and M. S. Triantafyllou. Galloping response of a cylinder with upstream wake interference. *Journal of Fluids and Structures*, 15(3):503–512, 2001.

[3] G. R. S. Assi, P. W. Bearman, B. S. Carmo, J. R. Meneghini, S. J. Sherwin, and R. H. J. Willden. The role of wake stiffness on the wake-induced vibration of the downstream cylinder of a tandem pair. *Journal of Fluid Mechanics*, 718:210–245, 2013.

[4] M. M. Zdravkovich. Review of interference-induced oscillations in flow past two parallel circular cylinders in various arrangements. *Journal of Wind Engineering and Industrial Aerodynamics*, 28(13):183–199, August 1988. ISSN 0167-6105. doi: 10.1016/0167-6105(88)90115-8.

[5] Daniel Holden, John J. Socha, Nicholas D. Cardwell, and Pavlos P. Vlachos. Aerodynamics of the flying snake *chrysopelea paradisi*: how a bluff body cross-sectional shape contributes to gliding performance. *The Journal of Experimental Biology*, 217(3):382–394, 2014.

[6] Farid Jafari, Shane D. Ross, Pavlos P. Vlachos, and John J. Socha. A theoretical analysis of pitch stability during gliding in flying snakes. *Bioinspiration & Biomimetics*, 9(2):025014, 2014.